Cavitation implosion loads from energy balance considerations in numerical flow simulations

Schenke, S.

DOI
10.4233/uuid:9b8243b3-cc41-4c70-a95d-158c7ad96bb8

Publication date
2020

Document Version
Final published version

Citation (APA)
Schenke, S. (2020). *Cavitation implosion loads from energy balance considerations in numerical flow simulations*. [Dissertation (TU Delft), Delft University of Technology]. https://doi.org/10.4233/uuid:9b8243b3-cc41-4c70-a95d-158c7ad96bb8

CAVITATION IMPLOSION LOADS FROM ENERGY BALANCE CONSIDERATIONS IN NUMERICAL FLOW SIMULATIONS

Proefschrift

ter verkrijging van de graad van doctor
aan de Technische Universiteit Delft,
op gezag van de Rector Magnificus prof. ir. T.H.J.J. van der Hagen,
voorzitter van het College voor Promoties,
in het openbaar te verdedigen op donderdag 17 september 2020 om 10:00 uur

door

Sören SCHENKE

Master of Naval Architecture and Ocean Engineering,
Technische Universität Hamburg, Hamburg, Duitsland,
geboren te Sömmerda, Duitsland.

Dit proefschrift is goedgekeurd door de

promotor: prof. dr. ir. T.J.C. van Terwisga
copromotor: prof. dr. ir. J. Westerweel

Samenstelling promotiecommissie:

Rector Magnificus,	voorzitter
Prof. dr. ir. T.J.C. van Terwisga,	Technische Universiteit Delft
Prof. dr. ir. J. Westerweel,	Technische Universiteit Delft
Onafhankelijke leden:	
Prof. dr. ir. R. Bensow,	Chalmers tekniska högskola
Dr.-Ing. S.J. Schmidt,	Technische Universität München
Prof. dr. M. Versluis,	Universiteit Twente
Prof. dr. S. Hickel,	Technische Universiteit Delft
Prof. dr. ir. C. Poelma,	Technische Universiteit Delft

This research was funded by the European Union Horizon 2020 Research and Innovation programme, Grant Agreement No. 642536, and by the MARIN (Maritime Research Institute Netherlands) Academy.

Keywords: cavitation erosion, implosion, energy balance

Printed by: Ipskamp Printing

Cover: Accumulated surface energy distribution on a horizontal disk caused by repetitive cavity implosions. The result is obtained from the numerical simulation of the experiment done by Franc *et al.* ["Impact Load Measurements in an Erosive Cavitating Flow", J. Fluids Eng. Dec 2011, **133**(12): 121301].

ISBN 978-94-6366-305-2

An electronic version of this dissertation is available at
`http://repository.tudelft.nl/`.

CONTENTS

SUMMARY

Cavitation erosion is a problem in the design of a wide range of fluid machinery involving liquid flows. Ship propellers, rudders, hydro pumps and turbines or diesel injectors are some of the most prominent examples. Cavitation occurs at locations of high local flow velocity, where the pressure may drop so low that the liquid phase vaporizes. The violent collapse of cavitating structures in regions of pressure recovery can result in high pressure loads and severe damage of such devices. Erosive cavitation is typically encountered when the hydrodynamic efficiency of fluid machinery is optimized. In order to find an appropriate balance in the design trade-off between hydrodynamic efficiency and the risk of cavitation erosion damage, there is a need for computational tools that can predict the risk of cavitation erosion in the early design and optimization process. The prediction of cavitation erosion risk using Computational Fluid Dynamics (CFD), however, is a major challenge because the local erosion damage is the result of extreme pressure loads forming at the final stage of cavity collapses at extremely small scales in both space and time. Due to limited computational resources, such small scales can usually not be resolved for flow problems relevant to engineering applications.

The main contribution of the present research effort is an acoustic model to compute cavitation implosion loads with numerical simulation tools that are typically used in engineering practice. To approach the aforementioned problems, the present research has essentially two goals. The first goal is to better understand which quantities of the cavitating flow can be reliably predicted with engineering flow simulation tools. It is found that kinematic flow parameters such as the collapse time of larger scale cavities or the frequency of periodic cavitating flows are reliably predicted, whereas the extreme pressure loads eventually leading to cavitation erosion are not reliably predicted. Against this finding, the second and most relevant goal is to develop a cavitation implosion load model that relies on the evolution of the macroscopic vaporous structures in the cavitating flow. The impact load resulting from the collapse of these structures is linked to their potential energy content. While this idea is actually not new, there are only very few attempts to rigorously incorporate the energy balance involved in the energy cascade from the initial potential energy content of a collapsing structure to the final impact load somewhere on the solid surface. However, satisfying the collapse energy balance is crucial when quantitative impact load predictions are the principal aim.

The suggested modeling approach can be subdivided into two sub-problems, both coming at their own difficulties. The first problem is to identify the collapse locations in a cavitating flow and the energy content that is radiated from these sources in form of shock wave energy. In an approximation that is good enough for most engineering purposes, the cascade of energy leading to the radiated energy content essentially involves the decrease of potential energy of the collapsing structure, which feeds into kinetic energy of the surrounding liquid. In order to exploit the advantage that the macroscopic evolution of collapsing cavitating structures is well predicted, the energy content radi-

ated from the collapse center must be determined from the history of the collapse. For this reason, the radiated energy content cannot simply be extracted from the instantaneous local flow quantities computed by the numerical flow solver. Instead, a novel transport equation of collapse induced kinetic energy is proposed to track the amount of kinetic energy induced by collapsing vaporous structures and to transport this energy into the collapse center. By this means, a physical focusing of the accumulated kinetic energy into the collapse center is achieved. In this modeling frame work, the decrease of potential cavity energy and the radiation of shock wave energy act as source terms in the transport equation of collapse induced kinetic energy. The transport terms and the criterion to identify the final collapse stage, at which energy radiation is assumed to take place, are formulated in such a way that the transport equation can reflect the energy cascade of interacting cavities. This, in return, enables to capture the energy focusing mechanism of a collective bubble cloud collapse.

The second problem concerns the energy conservative propagation of the radiated shock wave energy to the solid surfaces. Formally, this is achieved in a rather straightforward fashion via a projection approach based on spherical wave propagation. The problem here is that the surface projection of multiple sources can get computationally expensive. A computationally efficient approach to achieve this projection is presented in this work. Finally, a statistical analysis method is developed to identify extreme event contributions to the surface energy distribution accumulated from repetitive cavitation implosion loads.

The acoustic cavitation implosion load model developed in this work is applied to three test cases. The purpose of these test cases is to show in how far the model can compete with high fidelity simulations and what the limitations are. Best practice guidelines for the use of the model are developed and it is indicated that quantitative predictions of cavitation implosion loads are possible. In future work, the implosion load model can be linked to material models to predict the material damage caused by violent cavitation.

SAMENVATTING

Cavitatie-erosie is een verschijnsel dat bij het ontwerp van verschillende soorten turbomachines zoals bijvoorbeeld scheepsschroeven, roeren, vloeistofpompen, turbines en dieselinjectoren een belangrijke rol speelt. Cavitatie vindt plaats op locaties met een hoge lokale stroomsnelheid, waar de druk zo laag kan dalen dat de vloeibare fase verdampt. De gewelddadige implosie van cavitatiebellen in gebieden waar de druk vervolgens herstelt, kan tot hoge drukbelastingen en ernstige schade aan dergelijke apparaten leiden. Erosieve cavitatie vindt doorgaans plaats wanneer de hydrodynamische efficiëntie van turbomachines wordt geoptimaliseerd. Om een passend evenwicht te vinden tussen de efficiëntie en de erosiviteit van de caviterende stroming, is er behoefte aan computertools die het risico van cavitatie-erosie in het vroege ontwerp- en optimalisatieproces kunnen voorspellen. De voorspelling van het risico op cavitatie-erosie met behulp van Computational Fluid Dynamics (CFD) is echter een grote uitdaging, omdat de lokale erosieschade het gevolg van extreme drukpulsen is, die zich in het laatste stadium van een implosie op extreem kleine schaal in zowel ruimte als tijd vormen. Dergelijk kleine schalen kunnen echter niet worden opgelost met de CFD tools die voor technische toepassingen relevant zijn, vanwege de beperkte rekenkracht en tijd die doorgaans beschikbaar is.

De belangrijkste bijdrage van de huidige onderzoeksinspanning is een een akoestisch model om cavitatie-implosiebelastingen te kunnen berekenen, met numerieke simulatietools die voor de technische praktijk toepasbaar zijn. Om de bovengenoemde problemen aan te pakken, heeft het huidige onderzoek in wezen twee doelen. Het eerste doel is om beter te begrijpen welke delen van de caviterende stroming betrouwbaar voorspeld kunnen worden met de simulatietools uit de technische praktijk. Het huidige onderzoek toont aan dat kinematische stromingsparameters zoals de implosietijd van de grotere caviterende structuren of hun afschuddingsfrequentie in periodiek caviterende stromingen betrouwbaar berekend kunnen worden, terwijl de voorspelling van de extreme drukbelastingen die uiteindelijk tot cavitatie-erosie leiden niet betrouwbaar is. Tegen deze achtergrond is het tweede en meest relevante doel het ontwikkelen van een cavitatie-implosiemodel, dat op de evolutie van de macroscopische dampvormige structuren in de stroming berust. De huidige studie koppelt de impactbelasting als gevolg van de implosie aan de potentiële energie-inhoud van de dampstructuren. Deze koppeling is op zich niet nieuw, er zijn echter maar heel weinig toepassingen bekend waarbij rekening is gehouden met de volledige energiebalans. Het voldoen aan de implosie-energiebalans is echter cruciaal wanneer er naar een kwantitatieve voorspelling van de impactbelasting wordt gestreefd. Deze energiebalans moet zowel de aanvankelijke potentiele energie-inhoud van een imploderende structuur als ook de energiecascade tot aan de uiteindelijke impactbelasting ergens op een vast oppervlak bevatten.

De voorgestelde modelaanpak kan in twee deelproblemen onderverdeeld worden, die elk hun eigen moeilijkheden met zich mee brengen. Het eerste probleem is het iden-

tificeren van de implosielocaties in de stroming en de berekening van de energie-inhoud die vanuit deze bronnen in de vorm van schokgolfenergie wordt uitgestraald. In een benadering die voldoende nauwkeurig is voor de meeste technische doeleinden, omvat de energiecascade, die tot de uitgestraalde energie leidt, in wezen de afname van de potentiële energie van de imploderende structuur, die omgezet wordt in kinetische energie van de omgevende vloeistof. Om gebruik te kunnen maken van de bevinding dat de macroscopische evolutie van de ineenstortende cavitatiestructuren voldoende nauwkeurig voorspeld wordt, zou de vanuit het implosiecentrum uitgestraalde schokgolfenergie uit de geschiedenis van de implosie bepaald moeten worden. Deze informatie is echter niet beschikbaar in het instantane stroomveld, en om deze reden kan de uitgestraalde energie niet via deze weg worden bepaald. In plaats daarvan wordt een nieuwe transportvergelijking voorgesteld, die de formatie van kinetische energie in aanmerking neemt die door de implosieprocessen opgewekt wordt. De tijdelijke en ruimtelijke verdeling van de geïnduceerde kinetische energie wordt achterhaald om de energiehoeveelheid in het implosiecentrum te bepalen. Op deze manier wordt de focussering van de geaccumuleerde kinetische energie naar het implosiecentrum bereikt. De afname van de potentiële energie en de uitstraling van schokgolfenergie zullen dan als brontermen in de transportvergelijking van de implosie-geïnduceerde kinetische energie optreden. De transporttermen maar ook het criterium om het eindpunt van de primaire implosie en dus de locatie van energie-uitstraling vast te stellen, zijn zo geformuleerd dat de transportvergelijking de energie-uitwisseling tussen meerdere cavitatiebellen kan weerspiegelen wanneer deze tijdens de implosie in interactie met elkaar treden. Daardoor wordt het mogelijk gemaakt, om het energiefocusseringsmechanisme van de implosie van een collectieve bellenwolk weer te spiegelen.

Het tweede probleem betreft de verspreiding van de uitgestraalde schokgolfenergie naar de vaste oppervlakken op een zodanige manier, dat aan het wet van behoud van energie wordt voldaan. Formeel wordt dit op een vrij eenvoudige manier via een sferische projectie bereikt, die op de behoudswet van sferische golfvoortplanting gebaseerd is. Het probleem hier is dat de projectie van een groot aantal bronnen rekenkundig duur kan worden. In verband met dit werk wordt een rekenkundig efficiënte methode gepresenteerd om deze projectie uit te voeren. Ten slotte is een statistische analysemethode ontwikkeld, om in het geval van periodieke cavitatie en de daaruit voortvloeiende herhaaldelijke cavitatie-implosielastingen de extreme bijdragen aan de verdeling van de geaccumuleerde oppervlakte-energie te identificeren.

Het akoestische cavitatie-implosiemodel wordt op drie testcases toegepast. Het doel van deze testcases is om te laten zien in hoeverre het model met meer geavanceerde simulaties kan concurreren en wat de beperkingen ervan zijn. Er worden richtlijnen voor beste praktijken voor het gebruik van het model ontwikkeld, en er wordt aangetoond dat kwantitatieve voorspellingen van cavitatie-implosiebelastingen mogelijk zijn. In de toekomst zou het implosiemodel aan materiaalmodellen gekoppeld kunnen worden, om op deze manier de erosieschade als gevolg van schadelijke cavitatie te voorspellen.

1

INTRODUCTION

Parts of this chapter were published in Physics of Fluids **31**, 052102 (2019) [1] and in the International Journal of Multiphase Flow **111**, 200 (2019) [2].

1

1.1. A BRIEF OVERVIEW OVER RESEARCH ON THE NUMERICAL PREDICTION OF CAVITATION EROSION

The development of cavition erosion models for numerical flow simulations is strongly driven by the question what the most essential mechanism of cavitation erosion would be. An ongoing debate concerns the question whether cavitation erosion is predominantly caused by impinging liquid micro-jets or by collapse induced shock waves impacting the solid surface. Fig. 1.1 depicts high-speed shadowgraphic images of an isolated vapor bubble collapse [3], resulting in a spherical shock wave. When a vapor bubble collapses in close distance to a solid wall, the surrounding pressure distribution becomes non-symmetric in such a way that the collapse is predominantly driven from the wall-opposite side. As exemplary shown in Fig. 1.2 [4], this leads to the formation of a high velocity liquid jet, which penetrates the bubble and eventually impinges the solid wall. The moment of jet incidence on the wall goes along with a high amplitude water hammer pressure of very short impact duration [5], after which the impinging jet causes a stagnation pressure of smaller amplitude but longer impact duration [5].

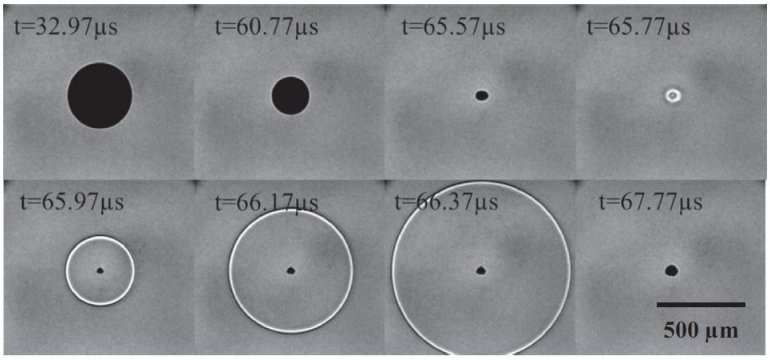

Figure 1.1: High-speed shadowgraphic images of the isolated collapse of a laser induced vapor bubble taken from the work by Johansen *et al.* [3]; a shock wave forms at the final collapse stage and propagates in spherical direction.

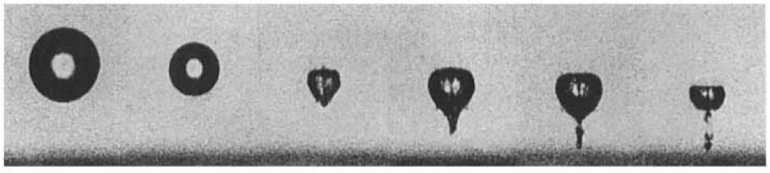

Figure 1.2: High-speed photography of the close wall collapse of a laser induced vapor bubble taken from the work by Vogel *et al.* [4]; the maximum bubble radius after generation is $R_0 = 2$ mm and the wall distance is $2.3R_0$.

The liquid jet hypothesis on the one hand is often motivated by the assumption that near wall bubbles collapse under the influence of shock waves caused by the collapse of larger scale structures [6]. A liquid micro-jet forms due to bubble-wall interaction [5]

and impinges the solid surface. The jet is supposed to cause erosion pit formation if the liquid mass velocity exceeds a critical threshold velocity [7]. Relations between the liquid jet velocity, ambient conditions and geometrical parameters of a near-wall bubble collapse were in numerous studies, suggesting that the jet velocity is proportional to the square root of the driving pressure [8, 9]. This relation was adopted by Dular and Coutier-Delgosha [10] to model the formation of cavitation erosion pits caused by impinging liquid jets, where the occurrence of the individual jet impacts is linked to the local flow conditions predicted from a numerical flow simulation.

An important foundation of the shock wave hypothesis on the other hand is the potential energy hypothesis initiated by Hammitt [11]. According to the later formulation by Vogel and Lauterborn [12], it states that the potential energy of the spherical bubble is proportional to its initial volume and the difference between the static ambient pressure p_∞ and the vapor pressure p_v. This relation can be interpreted as the work that the surrounding liquid can do on the vapor volume throughout the collapse. With R_0 being the initial bubble radius and r the distance from the center, this work and hence the initial potential bubble energy is given by [12–14]

$$E_{\mathrm{pot},0} = \int_0^{R_0} 4\pi r^2 \left(p_\infty - p_v\right) dr = \frac{4}{3}\pi R_0^3 \left(p_\infty - p_v\right). \tag{1.1}$$

Vogel and Lauterborn [12] further support the potential energy hypothesis by showing experimentally that the energy of a spherical acoustic transient as derived by Cole [15] is indeed proportional with the initial potential energy of a spherical bubble collapsing close to a solid wall. Wang and Brennen [16] as well as Schmidt *et al.* [17] and Ogloblina *et al.* [18] have shown by a numerical simulation of vapor bubble cloud collapses, that such clouds exhibit a collective behavior if they are densely populated. Practically the entire energy content of the cloud can then feed into a single primary shock wave. Early applications of the potential energy concept to cavitating flow problems are found in the work by Pereira *et al.* [19], Patella and Reboud [20], and Patella *et al.* [21]. They explain how energy is transferred from the collapse of macro-scale cavities to the solid surface in an energy cascade. As shown by Vogel and Lauterborn [12] and Kato *et al.* [22], the distance of imploding cavities from the impacted surface plays a major role in this energy cascade. Two different integral approaches evolved from this understanding. One approach attempts to identify isolated collapse events to assess their surface impact strength from the wall distance and kinematic parameters. Mihatsch *et al.* [23] partially assess the impact aggressiveness from the maximum local velocity divergence at the final stage of the collapse. Based on the work by Bark *et al.* [24], Arabnejad and Bensow [25] assess the collapse aggressiveness from the maximum volume change of the entire isolated cavity, which occurs prior to the final stage of the collapse. Another family of approaches rather attempts to assess the collapse strength in a direct integral fashion without isolating individual collapse events. Different from the approaches by Mihatsch *et al.* [23] and Arabnejad and Bensow [25], it is assumed that the collapsing cavities release their potential energy instantaneously during the collapse. Patella *et al.* [26] integrate the locally released power over an aggressiveness height derived from the work by Kato *et al.* [22]. Leclercq *et al.* [27] derived a discrete surface impact power model from the solid angle projection of released power on a discrete surface element. Apart

from the integral approaches described above, there are also attempts to utilize the potential energy concept for the prediction of cavitation erosion exclusively based on local flow quantities. Those approaches are essentially based on local changes of vapor volume and/or pressure [28, 29] and can be used as qualitative aggressiveness indicators. However, a quantitative model of impact loads based on the potential energy hypothesis [11, 12] should somehow involve the cascade of potential cavity energy into radiated shock wave energy and eventually into local impact power, as formally described by Pereira *et al.* [19], Patella *et al.* [21], and Bark *et al.* [24].

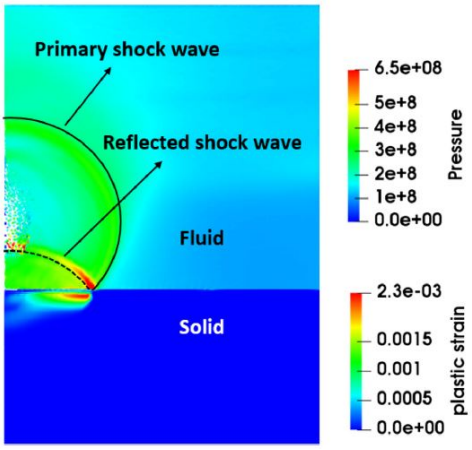

Figure 1.3: Axisymmetric Smoothed Particle Hydrodynamics (SPH) simulation by Joshi *et al.* [30] to compute the plastic material deformation caused by the collapse of a vapor bubble initially attached to the solid surface.

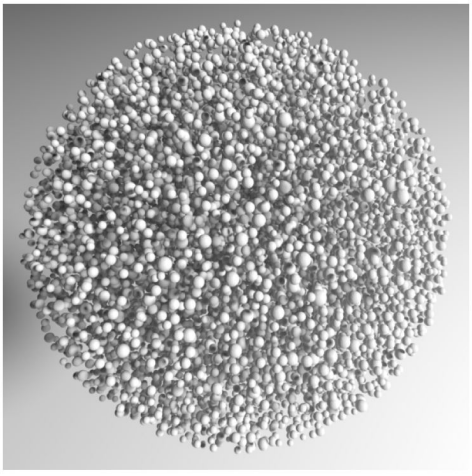

Figure 1.4: Resolved cloud of 12500 gas bubbles taken from the work by Rasthofer *et al.* [31]; the numerical simulation of the cloud collapse involved nearly $232 \cdot 10^9$ grid cells.

More detailed insights into the mechanisms leading to cavitation erosion are obtained from highly resolved numerical simulations that are restricted to very local phenomena. What makes the problem intriguingly difficult is that cavitation erosion is a complex non-linear interaction of fluid and material dynamics. An attempt to capture both was made by Joshi *et al.* [30], who employed Smoothed Particle Hydrodynamics (SPH) to simulate the collapse of a vapor bubble attached to a solid surface and the resulting plastic material deformation. They found that the intersection of the primary collapse shock wave front with the shock wave front reflected from the material surface leads to the highest observed surface pressures (see Fig. Fig. 1.3). The intersecting shock wave front propagates from the center of initial impact in radial direction, where both the pressure and the propagation speed gradually decrease. Joshi *et al.* [30] suggest that while the local pressure is largest at the center of initial impact, the impact duration might be too short for the material to reach its yield point. Taking both the impact pressure and the material response time into account, Joshi *et al.* [30] suggest an effective pressure to explain why most of the plastic strain depicted in Fig. 1.3 occurs at some distance away from the impact center. Based on their results, Joshi *et al.* [30] further argue

that even though the local incubation time of surface erosion may be smaller for the liquid micro-jet impact, the material volume plastified by a shock wave can be expected to be significantly larger. Obviously, the availability of computational resources sets a limit to the applicability of such highly resolving flow simulations. An example of the resolution that can be achieved when supercomputer resources are employed is shown in Fig. 1.4. In order to simulate the high ambient pressure collapse of a non-cavitating gas bubble cloud including 12500 bubbles, nearly $232 \cdot 10^9$ computational grid cells were used in the work by Rasthofer *et al.* [31]. To give an order of magnitude, this is approximately $\mathcal{O}\left(10^4\right)$ times more than what is typically affordable in engineering practice. At the same time, the time and length scales that are resolved in the work by Rasthofer *et al.* [31] with the given computational effort are still orders of magnitudes smaller than the scales of typical engineering flow problems.

1.2. APPROACH IN THE PRESENT RESEARCH

1.2.1. PROBLEM DEFINITION

In the present research, the potential energy concept is chosen as the basis of the cavitation implosion load model to be developed. It is considered as a decisive advantage that the computed impact loads are based on the evolution of the larger scale vapor structures in this modeling frame work. As it is discussed in more detail in Chap. 2, the evolution of vaporous cavitating structures can be accurately predicted by engineering flow simulation tools until the final collapse stage. From this moment on, both the insufficient resolution and the model simplifications affect the reliability of the impact load prediction. A global energy balance describing the collapse of an isolated vapor bubble in an infinite liquid was proposed by Tinguely *et al.* [14]. In slightly modified form, the energy balance by Tinguely *et al.* [14] is written as

$$E_{\text{pot},0} = E_{SW} + \Delta E_{\text{internal}} + E_{\text{reb}} + E_{\text{kin, res}}. \tag{1.2}$$

Eqn. (1.2) states that the initial potential energy $E_{\text{pot},0}$ is converted into different energy forms at and right after the final stage of the cavity collapse. The first three terms on the right-hand side were adopted from Tinguely *et al.* [14]. The energy radiated with the primary shock wave is denoted by E_{SW}. The term $\Delta E_{\text{internal}}$ represents the change of internal energy of non-condensable gas that is compressed in the collapse center, and E_{reb} is the energy amount that feeds into the potential of a rebound bubble. In addition to the energy partition by Tinguely *et al.* [14], the term $E_{\text{kin, res}}$ is included to account for residual kinetic energy that may still be present in the flow after the final collapse stage when the collapse is not symmetric as in the experiment by Tinguely *et al.* [14]. In particular, the energy absorbed by the liquid micro jet in a near-wall collapse situation can be thought to absorb a significant amount of $E_{\text{kin, res}}$. From the above considerations, the erosive potential of the liquid micro jet stems from its ability to focus some fraction of the residual kinetic energy $E_{\text{kin, res}}$ in space due to the small area in which this kinetic energy is concentrated. Having in mind that it is not affordable to resolve the length scale of individual vapor bubbles in larger scale flow simulations, and that the liquid micro jet is even much smaller in cross-section, one may conclude that the length scale of energy concentration associated with the micro jet impact is far beyond the currently affordable

resolution of the numerical flow simulation.

While Eqn. (1.2) represents the energy balance at the beginning and after the bubble collapse, the instantaneous energy balance during the collapse involves the conversion of potential bubble energy into kinetic energy $\dot{E}_{\text{kin}}$ of the surrounding liquid, such that

$$\frac{dE_{\text{pot}}}{dt} + \frac{dE_{\text{kin}}}{dt} = 0. \tag{1.3}$$

The acceleration of the liquid directly follows from mass conservation. It was shown by Obreschkow *et al.* [13], and earlier by Mikic *et al.* [32] in the context of bubble growth, how this conversion of potential into kinetic energy is directly related to the equation of motion of the bubble interface, as described by the well known Rayleigh equation [33].

In the present research, it is formally assumed that the potential energy content completely feeds into a shock wave radiated from the primary collapse, being aware that this is a strongly simplified representation of the events at and after the final collapse stage. However, it is argued that irrespective of how the work acting on the impacted surface is eventually partitioned into the different terms on the right-hand side of Eqn. (1.2), all contributions eventually feed from the original potential energy content. Satisfying this global energy balance, and knowing the involved numerical error sources when adopting it for a cavitation implosion load model, is considered crucial when the aim is to achieve quantitative impact load predictions. This means that by strictly following the modeling assumption that the potential energy content predominantly feeds into a primary shock wave, we do not imply that the impinging liquid jet does not potentially contribute to local erosion damage. The idea is rather to absorb all contributions to impact into one single quantity that satisfies the collapse energy balance at the length and time scales that are resolved by the flow simulation.

The conversion of the different energy forms involved in the cavity collapse and the surface impact is also vividly described in the work by Patella *et al.* [34], who have, together with Pereira *et al.* [19] and Bark *et al.* [24], shaped the concept of the energy cascade leading to cavitation erosion. Starting from the initial content of the potential energy, Patella *et al.* [34] define ratios in order to describe the conversion of potential energy into radiated shock wave energy E_{SW} and the conversion of radiated shock wave energy into plastic deformation energy of the material. The practical problems coming along with the attempt to build an impact load model based on the collapse energy cascade are illustrated in Fig. 1.5, which sketches four time instants A), B), C) and D) of a cavity collapse sequence on a hydrofoil. Following the collapse sequence, the challenges in describing the collapse energy cascade are identified as follows:

(A) Two cavitating structures are just about to collapse, where one structure is a large collective cloud composed of multiple cavities, and the other one is an isolated cavity. The collective structure is densely populated so that it behaves like one homogeneous structure with an equivalent vapor fraction [16, 17]. The entire cloud energy $E_{\text{pot, collective}}$ then gets focused into the cloud center, instead of being distributed over the centers of the individual cavities. The energy cascade model must be able to distinguish between a collective collapse behavior and an isolated collapse of associated energy $E_{\text{pot, isolated}}$.

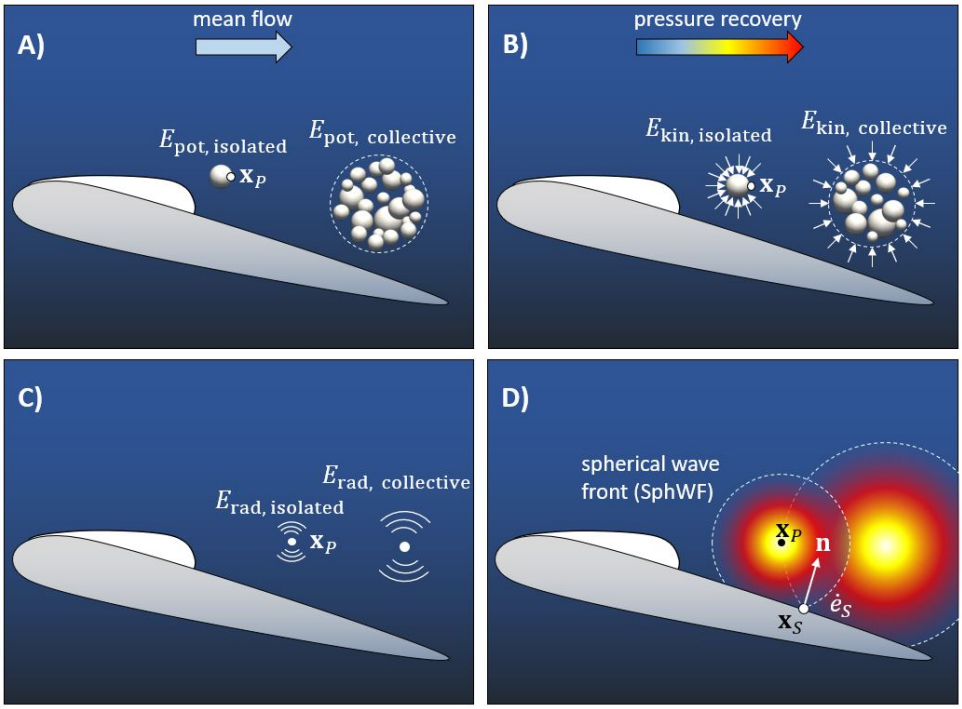

Figure 1.5: Sketch of a cavity collapse sequence on a hydrofoil; cavities have separated from a sheet cavity (A), implode in the region of pressure recovery (B), radiate shock waves at the final collapse stage (C), which propagate spherically and impact on the foil surface (D).

(B) As the cavities collapse, their potential energy content is reduced and distributed over the surrounding liquid in the form of kinetic energy. The distribution of this collapse-induced kinetic energy is known for an isolated bubble collapse, but not for more complex flow situations. Furthermore, the collapse-induced kinetic energy in the liquid phase also cannot be extracted from the numerical flow simulation, because it is an unknown part of the total flow velocity. The total flow velocity further includes an evaporization induced component due to the local expansion of the fluid. Also, different from an isolated bubble collapse in an infinite liquid, the collapse driving pressure is not a constant reference pressure p_∞, but actually varies both in space and time. In this particular case, the pressure recovery, as it occurs towards the trailing edge of a lifting foil, has a major influence on the collapse driving pressure distribution.

(C) At the final stage of the collapse, a shock wave is emitted. The radiated energy content E_{rad} feeds from the evolution of the collapse-induced kinetic energy. The final collapse stage must be identified in such a way that the energy cascade in a collective cloud collapse is supported.

(D) The energy radiated from each of the cavity collapses is assumed to propagate

spherically, where energy conservation requires the energy content across the spherical wave front (SphWF) to be constant. Hence, the local energy density decays with increasing distance from the collapse center. While the decay law of spherical waves is straightforwardly adopted in the modeling approach, the main problem to be solved is to make the model computationally efficient. As each point of the surface impact energy distribution is the result of a volume integral over all emission sources and the corresponding distances and surface orientations, the model can become expensive relative to the computational cost of the cavitation flow solver.

1.2.2. SKETCH OF THE PROPOSED SOLUTION

The main contribution of the present work is a computationally efficient model transport equation representing the collapse energy cascade described by Eqn. (1.3) and the acoustic surface impact following from spherical wave propagation. In the following, the transport equation is briefly sketched, as the present work essentially evolves around the modeling assumptions for its individual terms. Details on the derivation of the individual terms are then presented in Chap. 3. The transport equation of the energy cascade is formulated in the Eulerian reference frame and can be applied as a run-time post-processing tool in the numerical simulation of cavitating flows.

As discussed in Sec. 1.2.1, the local kinetic energy of the flow is given by

$$e_{\mathrm{kin}}(t,\mathbf{x}) = e_{\mathrm{kin},c}(t,\mathbf{x}) + e_{\mathrm{kin},v}(t,\mathbf{x}) + e_{\mathrm{kin},a}(t,\mathbf{x}), \tag{1.4}$$

where $e_{\mathrm{kin},c}$ and $e_{\mathrm{kin},v}$ represent the collapse/condensation-induced and the evaporation-induced kinetic energy, respectively, and $e_{\mathrm{kin},a}$ is the remaining component, which is thought to stand lose from the liquid kinetic energy induced by the cavity volume changes. Both $e_{\mathrm{kin},c}$ and $e_{\mathrm{kin},v}$ can only exist because of the presence of divergence sources somewhere in the flow vicinity, whereas $e_{\mathrm{kin},a}$ is of purely advective nature. However, the velocity fields of all three components are divergence free and cannot be distinguished from each other. Consequently, the spatial distribution of the collapse-induced kinetic energy $e_{\mathrm{kin},c}$ feeding into radiated shock wave energy is unknown. It is known from Eqn. (1.3), however, that the total amount of kinetic energy induced by a collapsing cavity is equal to the change of potential energy that the cavity has experienced. This motivates the idea to artificially absorb the collapse-induced kinetic energy present at locations $\mathbf{x}$ into the interface of the collapsing cavity, denoted by coordinates $\mathbf{x}_P$. The artificially absorbed kinetic energy is denoted by $\mathscr{E}$, and the absorption process is illustrated by Fig. 1.6. As is later discussed in more detail in Sec. 3.1.1, the kinetic energy distribution induced by a collapsing cavity focuses into the collapse center. This means that $\mathscr{E}$ evolves into a physically correct representation of the induced kinetic energy when the final collapse stage is approached.

The energy cascade from potential energy into collapse-induced kinetic energy into radiated shock wave energy can then be described by

$$\frac{\partial \mathscr{E}}{\partial t} - \underbrace{(1-\beta)\,\phi(\mathscr{E})}_{\text{conservative transport}} = \underbrace{-(1-\beta)\left(\frac{De_{\text{pot}}}{Dt}\right)_c}_{\substack{\text{potential energy reduction} \\ \downarrow \\ \text{kinetic energy generation}}} - \underbrace{\beta\frac{\partial \mathscr{E}_{\text{rad}}}{\partial t}}_{\substack{\text{energy radiation} \\ \downarrow \\ \text{kinetic energy reduction}}} , \qquad (1.5)$$

$$\text{where} \quad \int_{\text{vol}} \phi(\mathscr{E})\, dV = 0 \quad \text{and}$$

$$\beta(t,\mathbf{x}_P) = \begin{cases} 1 & \text{at the final collapse stage} \\ 0 & \text{else.} \end{cases}$$

Eqn. (1.5) is the transport equation of the absorbed collapse-induced kinetic energy $\mathscr{E}$. The first term on the right-hand side represents the generation of kinetic energy due to the reduction of potential energy as a result of condensation. The second term on the right-hand side represents the conversion of kinetic energy into radiated shock wave energy. Both terms act as source terms in the kinetic energy balance. The term $\phi(\mathscr{E})$ on the left-hand side denotes the conservative transport of $\mathscr{E}$ along the cavity interface. It requires a modeling assumption, because it must allow for a redistribution of energy between coherently cavitating structures in collective collapse situations. The parameter $\beta(t,\mathbf{x})$ is equal to 1 when a final collapse stage is identified and thereby activates the radiation source term in Eqn. (1.5). At any location, where no final collapse stage is identified, β is equal to 0 to keep the potential energy reduction term and the conservative transport term $\phi(\mathscr{E})$ active.

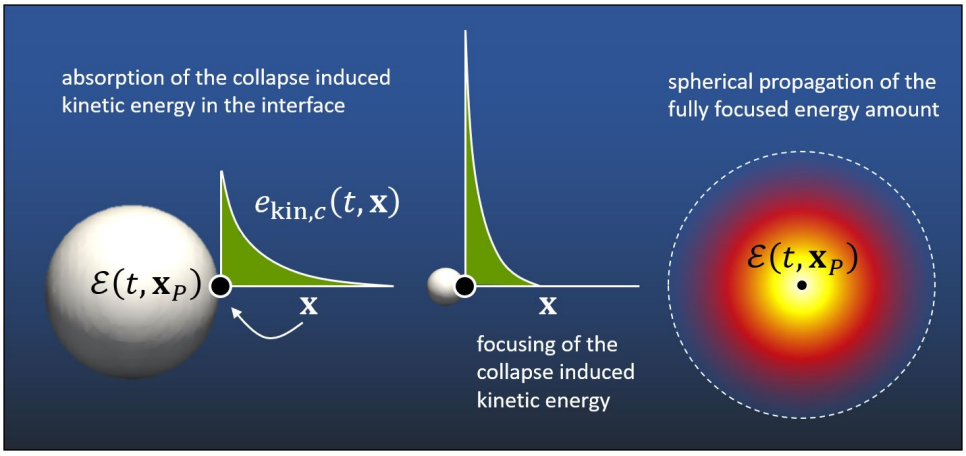

Figure 1.6: Illustration of how the collapse-induced kinetic energy distribution $e_{\text{kin},c}(t,\mathbf{x})$ is absorbed into $\mathscr{E}(t,\mathbf{x}_P)$ at the cavity interface; this artificial representation becomes physically correct at the final stage of the collapse, where the distribution of $e_{\text{kin},c}(t,\mathbf{x})$ is entirely focused into the collapse center

The impact power on the solid surface is given by

$$\left.\frac{\partial e_S}{\partial t}\right|_{t,\mathbf{x}_S} = \int_{\mathrm{vol}} \underbrace{\left(\beta \frac{\partial \mathscr{E}_{\mathrm{rad}}}{\partial t}\right)_{t,\mathbf{x}_P}}_{(\partial e_{\mathrm{rad}}/\partial t)_{t,\mathbf{x}_P}} \underbrace{G_{\mathbf{x}_P \to \mathbf{x}_S,\mathbf{n}}}_{\text{spherical wave projection}} \, dV, \tag{1.6}$$

$$\text{where} \quad G_{\mathbf{x}_P \to \mathbf{x}_S,\mathbf{n}} = \frac{1}{4\pi} \frac{(\mathbf{x}_P - \mathbf{x}_S) \cdot \mathbf{n}}{\| \mathbf{x}_P - \mathbf{x}_S \|^3}$$

$$\text{and} \quad \int_{t^*}^{t^* + T_{SW}} \oint_{\mathrm{SphWF}} \left(\frac{\partial e_{\mathrm{rad}}}{\partial t}\right)_{t,\mathbf{x}_P} G_{\mathbf{x}_P \to \mathbf{x}_S,\mathbf{n}} \, dS \, dt = \mathscr{E}(t, \mathbf{x}_P) .$$

The term $G_{\mathbf{x}_P \to \mathbf{x}_S,\mathbf{n}}$ in Eqn. (1.6) is the operator that represents the spherical wave propagation and projection from an emission source at location $\mathbf{x}_P$ onto a point $\mathbf{x}_S$ of the impacted surface, where $\mathbf{n}$ is the local surface normal vector. The radiated energy content $\mathscr{E}$ is conserved as the spherical wave front (SphWF) passes a fixed observation point in a wave passage time T_{SW} and the orientation of the impacted surface location relative to the encountered wave is taken into account. It is noted that Eqn. (1.6) is based on the assumption of infinite wave propagation speed and that the shock wave front is thought to be infinitely thin, such that $T_{SW} \to 0$. This means that in the present form, only the energy content of the radiated shock wave is well defined, but not its exact shape across the spherical wave front.

1.3. OUTLINE OF THE PRESENT RESEARCH

In Chap. 2 of this work, the physical and the numerical model for the simulation of the cavitating flow is presented. It is discussed why and under which operating conditions the cavitation model is able to accurately reflect the kinematic features of a cavitating flow, despite its simplifications. This finding justifies the applicability of the implosion load model presented in Chap. 3, which essentially relies on an accurate representation of the evolution of cavitating structures at larger scales.

In Chap. 3 detailed derivations and considerations are presented for the individual terms in Eqns. (1.5) and (1.6) that describe the collapse energy cascade. These terms are the conservative kinetic energy transport term $\phi(\mathscr{E})$, the driving pressure involved in the balance of e_{pot}, the criterion to identify the final collapse stage at which $\beta = 1$, and the spherical wave propagation and surface projection operator $G_{\mathbf{x}_P \to \mathbf{x}_S,\mathbf{n}}$. Most importantly, it is discussed how $\phi(\mathscr{E})$ and β can be modeled in such a way that Eqn. (1.5) supports the energy cascade mechanism in a collective collapse situation, as illustrated in Fig. 1.5. The numerical efficiency of the approach is further elaborated, and a statistical analysis method to identify extreme impact events in periodically cavitating flows is derived.

Chap. 4 is on the application of the implosion load model to three test cases. A collapsing bubble cloud is investigated to show that the energy focusing mechanism of a collective cloud collapse is captured by the model. Subsequently, the cavitating flow around a hydrofoil is studied to derive best practice guidelines for the statistical analysis method and the computation of the collapse driving pressure distribution. Finally, a test case involving the cavitating flow in an axisymmetric nozzle is employed to compare the model performance against experimental and numerical results from the literature. It is demonstrated that the present model can give physically converged results for the

energy impact distribution resulting from cavitation implosions. Here, physically converged, means that the obtained energy distribution is independent of the resolution of the numerical flow simulation and the involved cavitation model parameters. This can be seen as a first step towards quantitative predictions of cavitation erosion in engineering flow scenarios.

Conclusions and recommendations are finally presented in Chap. 5.

2

NUMERICAL REPRESENTATION OF THE CAVITATING FLOW DYNAMICS

In this chapter, the physical model and the governing equations of the cavitating flow are introduced. The technique is presented in relation to alternative approaches to elaborate on its expected accuracy and limitations on the one hand, and on its computational efficiency on the other hand. In Sec. 2.1, it is discussed analytically, in how far rather simplifying engineering cavitation flow models can mimic the behavior of more elaborate thermodynamic models as long as the cavitating flow can be classified as inertia driven.

The implications from the analytical considerations in Sec. 2.1 are further discussed in the light of the cavitating flow model presented in Sec. 2.2. Predictions about the cavitation model behavior are derived. The numerical implementation of the flow model is presented in Appx. A.

In order to demonstrate some of the predicted model features, the controlled situation of an isolated vapor bubble collapse is employed in Sec. 2.3. It is shown that the bubble collapse time is accurately predicted in the limit of large mass transfer coefficients, which is explained against the theoretical considerations in Sec. 2.1. The dynamics leading to the formation of violent cavitation implosion loads, however, are not accurately captured by the flow model. This behavior is typical for computationally efficient cavitation flow models used for large scale engineering applications and motivates the design of a cavitation implosion load model that strongly relies on kinematic flow features.

2.1. INERTIA DRIVEN DYNAMICS OF CAVITATING FLOWS

2.1.1. CLASSIFICATION OF CAVITATION MODELING APPROACHES

Fig. 2.1 is an attempt to classify existing cavitation models into physical categories, having in mind that this classification cannot be entirely sharp and complete due to the vast amount of modeling approaches. In the context of the present work, however, cavitation models can be classified into equilibrium and non-equilibrium models.

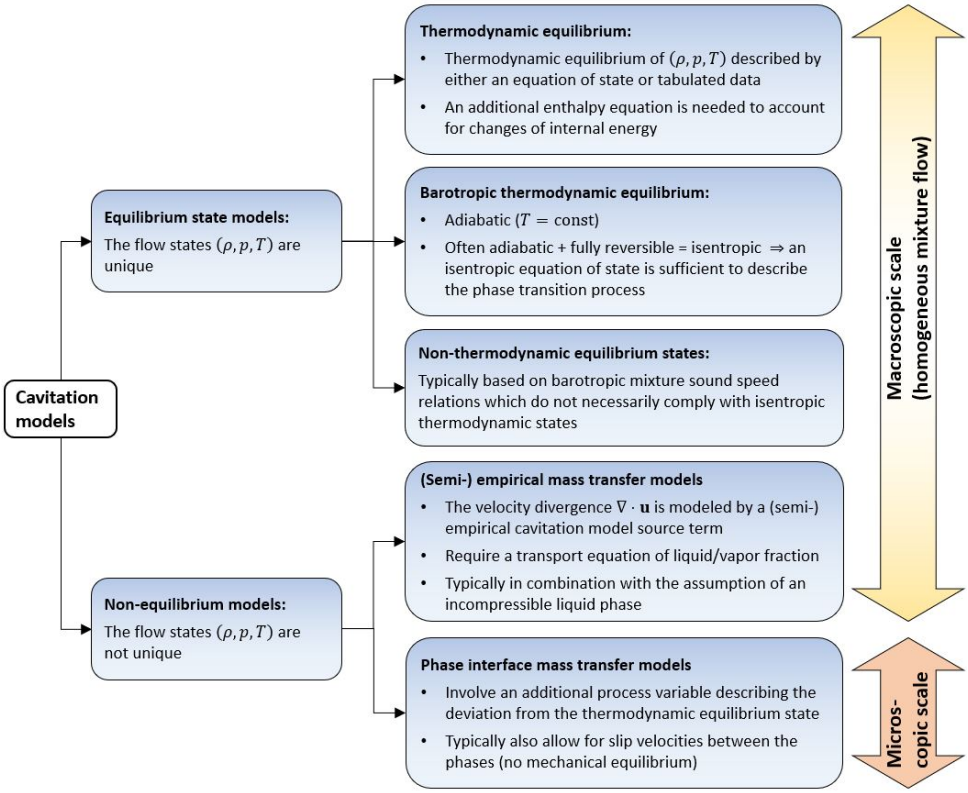

Figure 2.1: Classification of cavitation models existing in literature

On the macroscopic scale, cavitating flows are typically treated as homogeneous mixtures of liquid, vapor and possibly non-condensable gas. The mixture flow states are often assumed to satisfy the equilibrium flow assumption of macroscopic gas dynamics [35], which states that the phase equilibrium of all involved variables is established at any time instant. This means that the macroscopic states of density, pressure and temperature are unique. In order to achieve a most accurate representation of the macroscopic fluid states, thermodynamic relations can be employed to describe their dependency on each other. In the homogeneous equilibrium approach, the fluid flow is typically treated as fully compressible. The equation of state of the cavitating mixture is then often complemented by the ideal gas law of the gaseous phase and the Tait

equation of state [36, 37] for the pure liquid. To increase the numerical efficiency of these approaches, thermodynamic tables can be utilized alternatively [38, 39]. An enthalpy equation is needed to achieve closure in this modeling frame work [40] due to the changes of internal energy involved in the phase transition process and the compressibility of the mixed vapor/liquid and gas phases. When the involved thermodynamic processes are assumed to be adiabatic and fully reversible, an isentropic equation of state can be employed [41, 42]. Equations of state in which the pressure is directly linked to the density, such that $\rho = \rho\left(p\right)$, are referred to as barotropic equations of state [43–45]. Barotropic equations of state force the pressure and density gradients to be aligned with each other because $\nabla\rho\left(p\right) = \partial\rho/\partial p \nabla p$, which implies that no baroclinic vorticity can exist in such a flow [46]. Often, barotropic equations of state primarily aim to provide a realistic sound speed distribution of the cavitating mixture, but do not necessarily obey strict thermodynamic relations [43, 45]. The large compressibility of the cavitating mixture in combination with the nearly incompressible behavior of the pure liquid phase imposes considerable challenges from a numerical point of view, because a large range of Mach numbers needs to be handled [44, 47–49].

When it comes to the simulation of flow situations encountered in large scale engineering applications, the violation of the phase equilibrium constraint is therefore often accepted for the sake of computational efficiency and numerical robustness. The cavitating flow is then typically modeled by numerically less demanding mass transfer models, and the pure liquid phase is treated as incompressible, which allows for significantly larger time steps as no fast propagating pressure waves in the liquid phase need to be resolved. The modeling approaches belonging to this model family are often considered as (semi-) empirical [50–52], even though for instance the model by Sauer and Schnerr [53] is conceptually derived from sub-grid bubble dynamics considerations. In order to describe the phase transition of the mixture fluid flow in terms of a mass transfer process, an additional transport equation of the vapor-liquid fraction that includes the mass transfer source term needs to be solved [47, 53, 54].

Another family of non-equilibrium mass transfer models aims to directly simulate the phase change at the phase interface, [55] rather than the phase change of a homogeneous mixture fluid. The involved phases then need to be treated by separate sets of governing equations that involve cross coupling terms to model the exchange of mass and momentum and the heat transfer at the interfaces of the individual phases [56, 57]. Compared to aforementioned family of (semi-) empirical mass transfer models, these models involve a significantly more accurate description of the phase transition physics, as they essentially start from thermodynamic equilibrium and then introduce additional process variables to describe the deviation from the equilibrium state [40, 58]. Examples of situations where non-equilibrium effects become physically relevant are micro-scale cavitation bubble dynamics [55] or flashing liquid flows [59]. Cristofaro *et al.* [60] present a multifluid approach in which cavitation is still modeled as a mass transfer process in a mixture fluid flow, but where slip velocities between the phases are allowed. They have found that slip velocities between the liquid and the vapor phases are negligible on a macroscopic scale, but that they play an important role between the liquid and the gaseous phases of a combustion spray [60].

In the present work, a semi-empirical mass transfer modeling approach is employed

to model the macroscopic cavitating flow dynamics. In order to better understand and control the behavior of such models, it is useful to discuss how barotropic equilibrium states can be achieved by a finite rate mass transfer processes and in how far common engineering cavitation models deviate from the equilibrium mass transfer process.

2.1.2. EQUILIBRIUM VS NON-EQUILIBRIUM MASS TRANSFER

In this section, the apparent fluid compressibility, observed in the Eulerian and the Lagrangian reference frames, is derived for arbitrary mass transfer processes under the neglect of temperature effects. It is shown how the existence of barotropic density-pressure equilibrium states [43–45] is supported by an invariant of the compressiblity observed in both reference frames and how this invariant is satisfied by a finite-rate mass transfer process. The apparent flow compressibility allows to make analytical predictions on the behavior of mass transfer models that violate the equilibrium flow assumption.

The mass transfer process is interpreted as a source of velocity divergence, denoted by

$$\nabla \cdot \mathbf{u} = \Gamma, \tag{2.1}$$

such that the continuity equation

$$\frac{\partial \rho}{\partial t} + \nabla \cdot \left(\rho \mathbf{u}\right) = 0 \tag{2.2}$$

can be rewritten as

$$\frac{D\rho}{Dt} = -\rho\Gamma, \quad \text{where } \frac{D}{Dt} := \frac{\partial}{\partial t} + \mathbf{u} \cdot \nabla. \tag{2.3}$$

In the absence of temperature effects, the apparent compressibility at some location $\mathbf{x}$ and some time instant t is given by

$$\left.\frac{\partial \rho}{\partial p}\right|_{t,\mathbf{x}} = \lim_{\delta t \to 0} \frac{\rho\left(t+\delta t, \mathbf{x}\right) - \rho\left(t, \mathbf{x}\right)}{p\left(t+\delta t, \mathbf{x}\right) - p\left(t, \mathbf{x}\right)} \tag{2.4}$$

in the Eulerian reference frame and by

$$\left.\frac{D\rho}{Dp}\right|_{t,\mathbf{x}} = \lim_{\substack{\delta t \to 0 \\ \delta \mathbf{x} \to 0}} \frac{\rho\left(t+\delta t, \mathbf{x}+\delta \mathbf{x}\right) - \rho\left(t, \mathbf{x}\right)}{p\left(t+\delta t, \mathbf{x}+\delta \mathbf{x}\right) - p\left(t, \mathbf{x}\right)} \tag{2.5}$$

in the Lagrangian reference frame, where the position $\mathbf{x}$ and the displacement $\delta\mathbf{x}$ of the Lagrangian fluid particle is given with respect to the fixed Eulerian reference frame. Furthermore, the local densities and pressures in Eqns. (2.4) and (2.5) can be expanded in time by some infinitesimal δt, such that

$$\begin{aligned} \rho\left(t+\delta t, \mathbf{x}\right) &= \rho\left(t, \mathbf{x}\right) + \left.\frac{\partial \rho}{\partial t}\right|_{t,\mathbf{x}} \delta t, \\ p\left(t+\delta t, \mathbf{x}\right) &= p\left(t, \mathbf{x}\right) + \left.\frac{\partial p}{\partial t}\right|_{t,\mathbf{x}} \delta t \end{aligned} \tag{2.6}$$

and

$$\rho(t+\delta t,\mathbf{x}+\delta\mathbf{x}) = \rho(t,\mathbf{x}) + \left.\frac{D\rho}{Dt}\right|_{t,\mathbf{x}} \delta t,$$
$$p(t+\delta t,\mathbf{x}+\delta\mathbf{x}) = p(t,\mathbf{x}) + \left.\frac{Dp}{Dt}\right|_{t,\mathbf{x}} \delta t, \tag{2.7}$$

where the displacement contribution in Eqn. (2.7) follows from the advective term of the material derivative multiplied by δt, such that $\nabla\rho\cdot\mathbf{u}\delta t = \nabla\rho\cdot\delta\mathbf{x}$ and $\nabla p\cdot\mathbf{u}\delta t = \nabla p\cdot\delta\mathbf{x}$, which also implies that $\delta\mathbf{x}\to 0$ as $\delta t\to 0$. Substituting Eqns. (2.6) and (2.7) into Eqns. (2.4) and (2.5), respectively, these can be rewritten as

$$\frac{\partial\rho}{\partial p} = \frac{\partial\rho}{\partial t}\Big/\frac{\partial p}{\partial t} \tag{2.8}$$

and

$$\frac{D\rho}{Dp} = \frac{D\rho}{Dt}\Big/\frac{Dp}{Dt}, \tag{2.9}$$

respectively. Hence, the mass continuity equation as given by Eqn. (2.3) becomes

$$\frac{\partial\rho}{\partial p} = -\frac{\rho\Gamma + \nabla\rho\cdot\mathbf{u}}{\partial p/\partial t} \tag{2.10}$$

in the Eulerian reference frame, and

$$\frac{D\rho}{Dp} = -\frac{\rho\Gamma}{Dp/Dt} = -\frac{\rho\Gamma}{\partial p/\partial t + \nabla p\cdot\mathbf{u}} \tag{2.11}$$

in the Lagrangian reference frame. Unique equilibrium states of density and pressure are obtained if they can be described by a unique invertible function $\rho(p)$, which implies that also the slope of the ρ-p trajectory must be a unique function of ρ or p, regardless of the reference frame in which this trajectory is observed. This means that unique equilibrium states of ρ and p are only supported when the apparent compressiblity becomes invariant with respect to the frame of reference, such that

$$\frac{\partial\rho}{\partial p} = \frac{D\rho}{Dp} = \frac{d\rho}{dp} := \psi, \tag{2.12}$$

where ψ is the mechanical compressibility and where the derivative operator d indicates the invariant. From Eqns. (2.10), (2.11) and (2.12) it follows that this invariant is satisfied if and only if, when

$$\Gamma = -\frac{\psi}{\rho}\frac{Dp}{Dt} = -\frac{1}{\rho}\left(\psi\frac{\partial p}{\partial t} + \nabla\rho\cdot\mathbf{u}\right), \tag{2.13}$$

where the relation $\nabla p(\rho)\cdot\mathbf{u} = (dp/d\rho)\nabla\rho\cdot\mathbf{u} = (1/\psi)\nabla\rho\cdot\mathbf{u}$ is employed. As soon as the equilibrium constraint for Γ given by Eqn. (2.13) is violated, the flow compressibilty

cannot be uniquely described as a function of either ρ or p anymore. Mass transfer models, as typically employed for engineering applications, are usually given by a function of p and/or ρ. Eqns (2.10) and (2.11) suggest that the apparent compressibilty obtained from these models is then inversely proportional to $\partial p/\partial t$. Eqns (2.10) and (2.11) further suggest a dependency of the apparent compressibility on advected density $\nabla\rho\cdot\mathbf{u}$ in the Eulerian reference frame, and on advected pressure $\nabla p\cdot\mathbf{u}$ in the Lagrangian reference frame.

2.1.3. SCALE SEPARATION OF FLOW STATES

In this section, it is argued that the pressure scale at which phase transition occurs, typically separates from the characteristic pressure difference driving the inertial dynamics of the cavitating flow in most engineering applications. Such flows are typically subject to very confined regions of evaporation, where high local flow accelerations cause a local pressure drop necessary for cavitation inception to occur, even at relatively high operating pressures. The mixture fluid then exists within a pressure range that is small relative to the operating pressure, regardless of the exact vapor fraction of the mixture. The primary problem is then to correctly represent the collapse behavior of the generated vapor structures, which again is strongly governed by the pressure difference between the operating ambient pressure p_∞ and the vapor pressure p_v. More specifically, the above mentioned scale separation can be explained by the inverse Mach number $\mathrm{Ma}^{-1} = c_m/v_{\mathrm{inert}}$, where in this context, c_m is the associated mixture sound speed, and v_{inert} an inertial flow velocity that is characteristic of a cavity collapse. With the Rayleigh collapse time being $\tau = 0.915R_0\sqrt{\rho_l/\left(p_\infty - p_v\right)}$ [33], a measure of the inertial flow velocity is given by the time averaged collapse speed [61] $v_{\mathrm{inert}} = R_0/\tau = 1.09\sqrt{\left(p_\infty - p_v\right)/\rho_l}$ for an isolated bubble collapse. It is further noted that the mixture sound speed is related to the mechanical compressibility via the relation $d\rho/dp = 1/c_m^2$. Assuming the sound speed c_m to be approximately constant over the entire phase transition regime, as illustrated in Fig. 2.2, the relation between the phase transition pressure range Δp_m and the phase transition density range $\rho_l - \rho_v$ can be approximated by $c_m^2 = \Delta p_m/\left(\rho_l - \rho_v\right)$. From the mixture sound speed distribution derived by Pelanti and Shyue [62] based on the homogeneous equilibrium model by Stewart and Wendroff [63], the water-vapor mixture is assumed to be represented by an equivalent constant value of $c_m = 2.0$ m/s. Neglecting the constant 1.09 (since it is close to unity), it follows from the above considerations that

$$\mathrm{Ma}^{-1} = \frac{c_m}{v_{\mathrm{inert}}} = c_m\sqrt{\frac{\rho_l}{p_\infty - p_v}}. \tag{2.14}$$

When $\rho_l >> \rho_v$, the mixture sound speed is approximately $c_m = \sqrt{\Delta p_m/\rho_l}$ and Eqn. (2.14) can be expressed as the ratio between the pressure ranges Δp_m and $p_\infty - p_v$, such that

$$\mathrm{Ma}^{-1} \approx \sqrt{\frac{\Delta p_m}{p_\infty - p_v}}. \tag{2.15}$$

The inverse Mach number as given by Eqn. (2.14) and, for $\rho_l >> \rho_v$, by Eqn. (2.15), measures to what extent a cavitating flow is inertia driven. If the flow is assumed to

exist in unique barotropic equilibrium states, the range Δp_m at which phase transition occurs, is a well defined constant value that depends on the thermodynamic properties of the fluid. The range $p_\infty - p_v$ characterizes the ambient condition and can be seen as the driving force behind the cavity collapse. In typical practical flow situations, where $p_\infty \approx 1$ bar or larger, we have $\mathrm{Ma}^{-1} << 1$, and the flow can be seen as predominantly inertia driven. As long as this condition holds, the macroscopic inertial flow dynamics can be expected to be insensitive to the exact flow states in the phase transition regime.

The important implication of these considerations is that even semi-empirical non-equilibrium mass transfer models can give realistic representations of the inertial dynamics of cavitating flows as long as the density-pressure trajectories obtained from the model are steep such that $\mathrm{Ma}^{-1} << 1$, and as long as the obtained scale separation is physically justified. In physical situations where Ma^{-1} approaches 1, inertial forces become a less and less dominant driver of the cavity collapse dynamics, whereas the phase transition process becomes increasingly important. It can be expected that a correct representation of the mixture fluid states becomes increasingly important in that case.

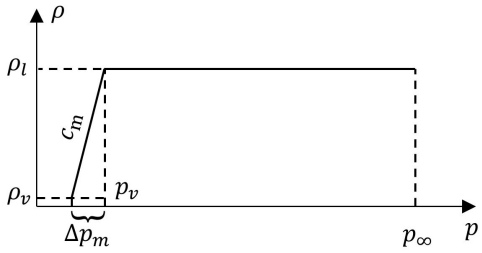

Figure 2.2: Illustration of the transition from vapor density ρ_v to liquid density ρ_l at constant mixture sound speed c_m

2.2. GOVERNING EQUATIONS AND CAVITATION MODEL

The flow model is a modified version of the flow solver interPhaseChangeFOAM that is available in the open source CFD package OpenFOAM [64]. The flow is assumed to be inviscid, and the Euler equations for momentum and mass continuity are solved:

$$\frac{\partial}{\partial t}\left(\rho \mathbf{u}\right) + \nabla \cdot \left(\rho \mathbf{u} \otimes \mathbf{u}\right) = -\nabla p \tag{2.16}$$

$$\frac{\partial \rho}{\partial t} + \nabla \cdot \left(\rho \mathbf{u}\right) = 0 \tag{2.17}$$

Furthermore, the flow is assumed to be incompressible in the pure liquid and vapor phases, where ρ_l and ρ_v are the liquid and vapor densities, respectively. The mixture density ρ is expressed in terms of the liquid fraction γ by the linear mixture relation

$$\rho = \gamma \rho_l + \left(1-\gamma\right)\rho_v, \qquad \text{where} \qquad 0 \leq \gamma \leq 1. \tag{2.18}$$

The mass transfer model by Merkle *et al.* [54] is employed in a slightly modified form [65] to model cavitation:

$$\nabla\cdot\mathbf{u}=\Gamma=-\frac{1}{\rho}\left(\frac{1}{\rho_v}-\frac{1}{\rho_l}\right)(p-p_v)\begin{cases} C_v\gamma & \text{for} \quad p\le p_v \\ C_c(1-\gamma) & \text{for} \quad p>p_v \end{cases} \tag{2.19}$$

The constants C_v and C_c are model coefficients to adjust the source term magnitude for the evaporation and condensation processes, respectively. Substituting the mixture density given by Eqn. (2.18) into Eqn. (2.17) gives the mass continuity equation expressed in terms of the liquid fraction:

$$\frac{\partial\gamma}{\partial t}+\nabla\gamma\cdot\mathbf{u}+\gamma\nabla\cdot\mathbf{u}=-\nabla\cdot\mathbf{u}\frac{\rho_v}{\rho_l-\rho_v} \tag{2.20}$$

Substituting the divergence term $\nabla\cdot\mathbf{u}$ on the right-hand side of Eqn. (2.20) by Eqn. (2.19) yields the transport equation of γ, which must be solved to achieve phase transition:

$$\frac{\partial\gamma}{\partial t}+\nabla\cdot(\gamma\mathbf{u})=-\frac{p-p_v}{\rho\rho_l}\begin{cases} C_v\gamma & \text{for} \quad p\le p_v \\ C_c(1-\gamma) & \text{for} \quad p>p_v \end{cases} \tag{2.21}$$

In order to examine the phase transition behavior of the model, the source term Γ as given by Eqn. (2.19) is substituted into Eqn. (2.10), which gives the apparent compressibility

$$\frac{\partial\rho}{\partial p}=-\frac{\nabla\rho\cdot\mathbf{u}}{\partial p/\partial t}+\left(\frac{1}{\rho_v}-\frac{1}{\rho_l}\right)\frac{p-p_v}{\partial p/\partial t}\begin{cases} C_v\gamma & \text{for} \quad p\le p_v \\ C_c(1-\gamma) & \text{for} \quad p>p_v \end{cases} \tag{2.22}$$

in the Eulerian frame of reference. Next to the dependency on the partial pressure derivative $\partial p/\partial t$ and the advected density $\nabla\rho\cdot\mathbf{u}$, as discussed in Sec. 2.1.2, Eqn. (2.22) shows that the apparent compressibility $\partial\rho/\partial p$ is proportional to the pressure difference $p-p_v$, the mass transfer constants C_v and C_c, as well as the liquid and the vapor fractions, given by γ and $1-\gamma$, respectively. By choosing large enough values for the model coefficients C_v and C_c, the apparent compressiblity of the mixture eventually becomes sufficiently large such that a scale separation of the phase transition/mixture pressure range Δp_m from the driving pressure difference $p_\infty-p_v$, as described in Sec. 2.1.3, is achieved. This means that the inertial dynamics of the flow become independent from the magnitude of the mass transfer coefficients in the limit of large coefficient values. By these means, the conditions of more physically correct thermodynamic equilibrium models can be mimicked [66], given that the physics of the flow situation are indeed such that the inverse Mach number given by Eqn. (2.15), is significantly smaller than 1.

2.3. ISOLATED BUBBLE VAPOR COLLAPSE

2.3.1. NUMERICAL SET-UP

A section of a spherical bubble is initialized in the computational domain shown in Fig. 2.3. An axisymmetric wedge and a symmetry boundary condition are applied on the patches specified in Table 2.1 to represent the spherical bubble. The wedge angle $\sphericalangle COD$ includes one cell layer. A structured spherical computational grid is used. This computationally efficient set-up has kindly been shared by M. H. Arabnejad (Marine Technology/Mechanics and Maritime Sciences at Chalmers University of Technology). The

computational grid is identical with the one that is used in the work by Ghahramani *et al.* [67]. Table 2.1 specifies the wedge angle as well as the sizes of the inner domain, where the cells are uniformly distributed in radial direction, and the outer domain, where the cell to cell expansion ration is such that a smooth cell size transition to the inner domain is achieved. A grid sensitivity study is not carried out for this test case, but it has been shown in previous work [2, 68] on similar cavity collapse test cases that a resolution of only two cells per initial cavity radius is already sufficient to achieve grid convergence. Therefore, the resolution of 20 cells per R_0 in the present set-up is high enough with margin.

Table 2.1: Mesh properties and boundary conditions for the isolated bubble collapse, where the reference points *O*, *A*, *B*, *C*, *D* and *E* are indicated in Fig. 2.3

Surface	*AOD*	*AOB*	*COD*	*ACD*
Boundary type	wedge	-	symmetry	far field
$\sphericalangle$ [deg]	-	90	5	-
Line	*OE*		*EA*	
Length [mm]	1 ($2.5R_0$)		499	
Number of cells	50		50	
Arc	*AB*		*CD*	
Number of cells	50		1	

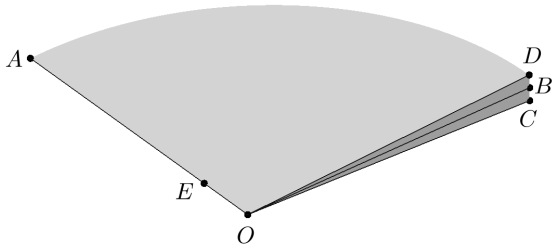

Figure 2.3: Outline of the computational domain (distance $\overline{OA}$ relative to $\overline{OE}$ is not true to scale); the boundary types of the individual patches are specified in Table 2.1

The initial bubble radius is R_b=0.4 mm and the liquid fraction γ is initially equal to 1 outside the bubble and equal to 10^{-5} inside the bubble (see Fig. 2.4, left). The liquid and vapor densities are assumed to be ρ_l = 1000 kg/m^3 and ρ_v = 0.02 kg/m^3, respectively. The bubble interface is initially at rest and then collapses under an ambient pressure of

$p_\infty = 1$ bar, which is imposed as a fixed value boundary condition at the far field patch. The vapor pressure is assumed to be $p_v = 2340$ Pa. The pressure field is initialized such that it satisfies the Laplace equation $\nabla \cdot \nabla p = 0$ (see Fig. 2.4, right). The liquid fraction γ is constrained by a zero gradient boundary condition at the far field. The bubble collapse behavior is investigated for a systematic variation of the mass transfer condensation constant C_c as given in Eqn. (2.19) and the time step size Δt. In particular, it is investigated how these two parameters affect the local phase transition behavior and eventually the collapse time of the isolated bubble. Furthermore, the maximum pressures are inspected. Iterative schemes, discretization schemes and residual controls are described in Appx. A. Different from the settings in Appx. A.3, the residual tolerance is chosen to be $\epsilon_\mathfrak{r} = 10^{-14}$ for all equations in this case. Ghahramani *et al.* [67] did a similar study on the effect of the mass transfer coefficient magnitude on the bubble collapse time and the evolution of the pressure field. In the present study, it is investigated in more detail how the states of pressure and density compare against the analytical predictions in Secs. 2.1.2 and 2.2 and how they affect the flow dynamics.

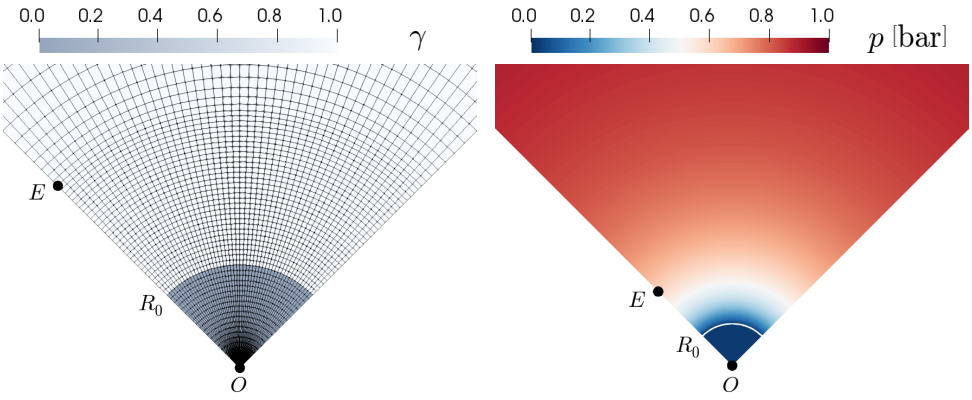

Figure 2.4: Initial γ distribution (left) with a sharp interface at $R_0 = 0.4$ mm and initial pressure distribution (right) with p satisfying the Laplace equation $\nabla \cdot \nabla p = 0$

2.3.2. THE EFFECT OF TIME STEP SIZE AND MASS TRANSFER COEFFICIENTS ON THE COLLAPSE DYNAMICS

Figure 2.5 depicts the evolution of the bubble radius over time for three different condensation rates and three different time step sizes. The (quasi) analytical solution is obtained from numerical integration of dR/dt, for which the analytical solution $dR/dt = \sqrt{2\left(p_\infty - p_v\right)\left(R_0^3/R^3 - 1\right)/\left(3\rho_l\right)}$ [33] is given. The overall observation is that the collapse time obtained from the numerical simulation converges to the Rayleigh [33] collapse time $\tau = 0.915 R_0 \sqrt{\rho_l/\left(p_\infty - p_v\right)}$ with increasing magnitude of the mass transfer coefficient C_c and with decreasing time step size Δt. However, a closer look reveals that the bubble collapse time does not unconditionally converge with increasing C_c. For the medium time step $\Delta t = 5 \cdot 10^{-8}$ s and even more for the largest time step $\Delta t = 5 \cdot 10^{-7}$

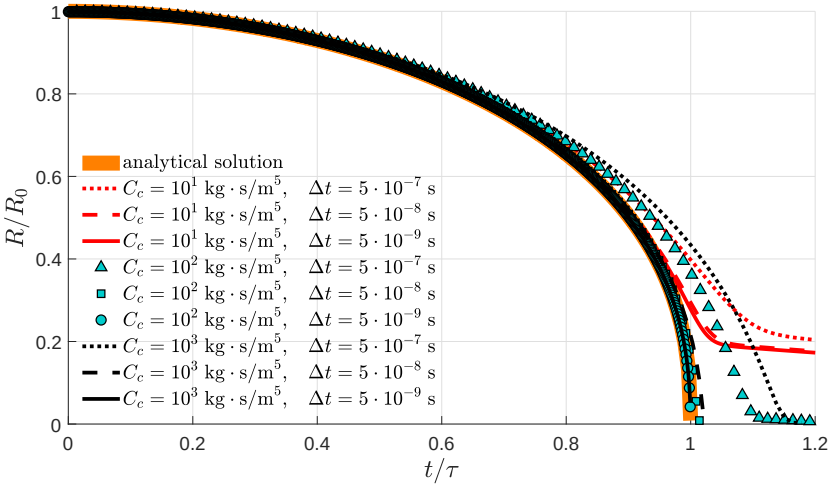

Figure 2.5: Evolution of the bubble radius $R(t)$ for different condensation rates C_c and time step sizes Δt

s, the collapse time tends to slightly increase again for the largest mass transfer coefficient value $C_c = 10^3$ kg·s/m^3. For the smallest time step $\Delta t = 5 \cdot 10^{-9}$ s, however, the collapse times obtained for $C_c = 10^3$ kg·s/m^3 and $C_c = 10^3$ kg·s/m^2 both coincide with the Rayleigh [33] collapse time τ. The convergence of the bubble collapse time to the Rayleigh [33] collapse time τ with increasing mass transfer coefficient value is in line with the findings by Bhatt *et al.* [69] and Ghahramani *et al.* [67].

The convergence with increasing C_c is explained by the circumstance that the increasingly steep ρ-p trajectories establish an inertia driven flow as discussed in Sec. 2.1.3. This is shown by the ρ-p trajectories in Fig. 2.6. The individual sub-figures represent different time steps, and each of them shows the trajectories for three different values of C_c and at three different distances from the bubble center. The trajectories appear to be practically independent from the time step size, but are strongly dependent on the location of the observation point and the condensation mass transfer coefficient. Both dependencies are predicted by Eqn. (2.22). At a fixed observation point, the trajectory slope increases with increasing C_c, because $\partial\rho/\partial p$ is proportional to C_c. For a fixed value of C_c, the slope decreases as the bubble center is approached, because $\partial\rho/\partial p$ is inversely proportional to the pressure change $\partial p/\partial t$, which again increases towards the collapse center.

An additional effect of large mass transfer coefficients is that the inertia driven liquid mass flow upstream from the collapsing bubble interface diverges into the bubble interface such that the flow velocity inside the bubble remains zero. In that sense, the mass transfer coefficients $C_{c,v}$ can be interpreted as a mass transfer capacity, which is only exploited to an extent governed by the speed of the inertial flow. If the mass transfer coefficient is chosen too low, however, there is a time instant from which on the mass transfer model does not have enough capacity anymore to achieve the local phase transition within the time scale dictated by the incoming inertia driven flow. From that mo-

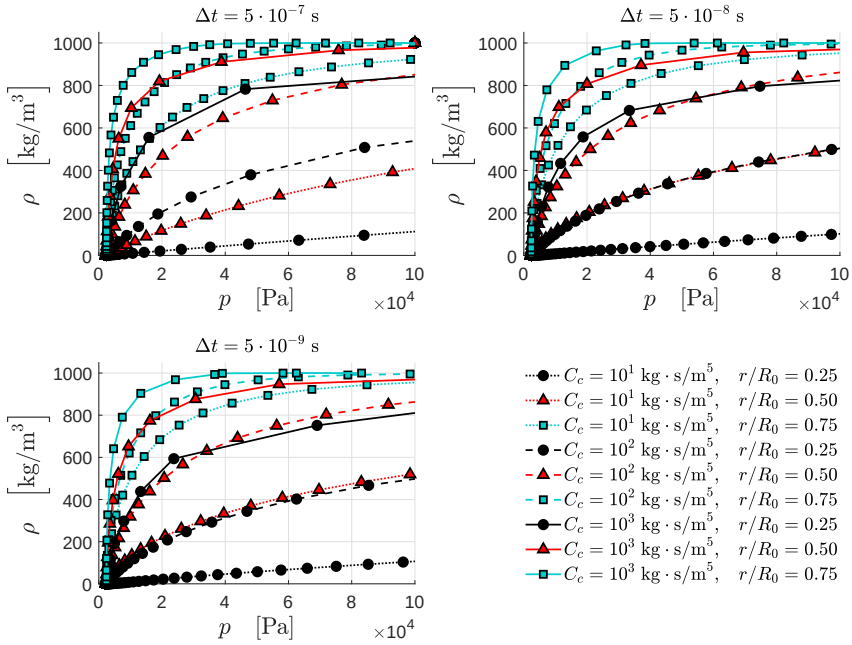

Figure 2.6: ρ-p trajectories at three different observation points and for different condensation rates and time step sizes

ment on, an increasing amount of mass flow is allowed to diffuse through the interface before the local condensation process is complete. This mass diffusion goes along with a non-physical pressure rise in the vapor phase. In order to demonstrate this effect, the evolution of the radial flow velocity u_r and the evolution of the pressure field are depicted in u_r-t (Fig. 2.7) and p-t (Fig. 2.8) diagrams, respectively, both for different values of $C_{c,v}$. In both figures, the green dashed line indicates the evolution of the bubble interface $R(t)$. As the bubble interface never appears to be perfectly sharp, the instantaneous interface position is reconstructed from $R = \left[3V_{\text{vap}}/(4\pi)\right]^{1/3}$, where V_{vap} is the instantaneous vapor volume in the computational domain.

Fig. 2.7 shows that the moment at which the bubble interface becomes diffuse, is delayed towards the final collapse stage with increasing C_c. For the smallest mass transfer coefficient $C_c = 10$ kg·s/m^5, a pronounced mass flow starts to diffuses through the interface at $t \approx 0.5\tau$ and reaches the bubble center at $t \approx 0.9\tau$. For large values of C_c, the interface sharpness is maintained reasonably well until close to the final collapse stage. The evolution of the reconstructed bubble interface, represented by the green dashed line, also indicates the formation of a rebound bubble for the larger mass transfer coefficients.

Fig. 2.8 shows that for the smallest mass transfer coefficient $C_c = 10$ kg·s/m^5, the vapor pressure inside the bubble cannot be maintained anymore from $t \approx 0.8\tau$ onward. An artificial stagnation pressure forms at the bubble center when the diffusing mass flow

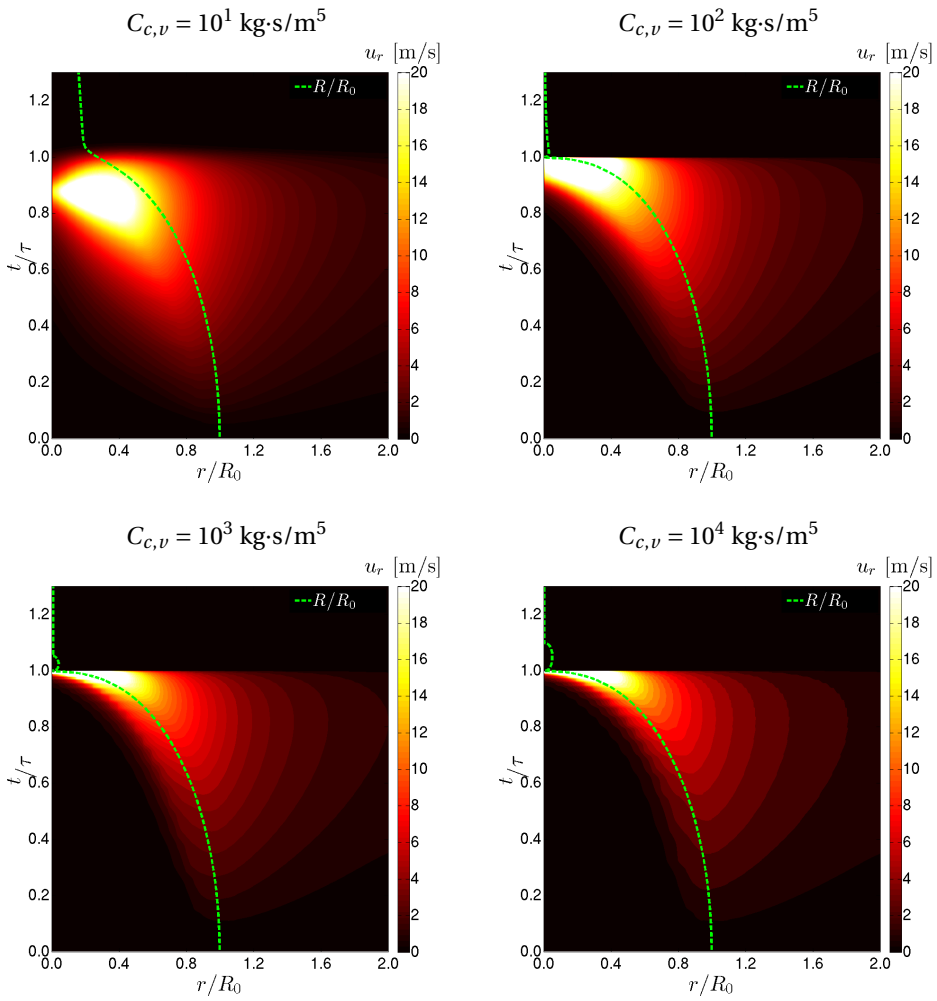

Figure 2.7: Radial velocity u_r over the non-dimensional distance r/R_0 from the bubble center and over the non-dimensional time t/τ for a variation of the mass transfer coefficients C_c, where R_0 is the initial bubble radius and τ the Rayleigh collapse time [33]; the green dashed line indicates the evolution of the bubble interface, where the instantaneous interface position is reconstructed from $R = \left[3V_{\text{vap}}/(4\pi)\right]^{1/3}$, with V_{vap} being the instantaneous vapor volume in the domain.

collides at the center. This artificial stagnation pressure is maintained as long as some mass flow is directed towards the center. The moment at which the pressure drops back to the ambient pressure p_∞ ($t/\tau \approx 1.05$) coincides with a pronounced decrease of mass transfer rate, because the local mass transfer rate is proportional to $p - p_v$ (see Eqn. (2.19)). This sudden decrease of mass transfer rate marks the point in Fig. 2.5 at which the bubble interface velocity $\dot{R}$ suddenly drops for $C_c = 10$ kg·s/m^5. For the larger C_c values, the vapor pressure inside the bubble is maintained, and the bubble fully collapses as t approaches τ. It is also noted that the pressure field around the bubble is subject to numerical perturbations which appear as short pulses increasing in amplitude with increasing C_c. Such pressure perturbations were also found by Ghahramani *et al.* [67] for large model coefficient values in the mass transfer model by Sauer and Schnerr [53]. Due to their short duration, however, they do not affect the evolution of the bubble interface. Furthermore, the numerical pressure perturbations, as well as the pressure pulse forming at the final stage of the collapse, appear as horizontal lines in the p-t diagram. This shows, as expected, that the pressure perturbations propagate infinitely fast through the incompressible liquid phase. For reference, the black dashed line indicates a propagation speed of 1500 m/s, which is approximately equal to the sound speed c_l in pure water.

The delayed bubble collapse at large time steps is explained by truncation errors that occur when the solution is forwarded in time by means of a linear discretization scheme, which affects the time that it takes for the ρ-p trajectory to evolve from vapor to liquid density. This effect is shown by Fig. 2.9, which depicts the evolution of the mixture density ρ over time for different mass transfer coefficients $C_{c,v}$, at different observation points and for different time step sizes. It can be seen that the local phase transition time converges with increasing values of $C_{c,v}$ and decreasing time step Δt. For the smallest time step $\Delta t = 5{\cdot}10^{-7}$ s, however, the largest condensation coefficient $C_c = 10^3 = $ kg·s/m^5 causes an additional delay of the local phase transition, especially for the inner observation point $r/R_0 = 0.25$, where the most rapid density change occurs. This is in line with the previous observation that sufficient temporal resolution is needed to converge the bubble collapse time in the limit of large mass transfer coefficient values. Presumably, this behavior is related to the numerical convergence of the discretized γ transport equation and the pressure equation. The local residual as given by Eqn. (A.24) is inversely proportional to the maximum value $\max\left(\| a_C \phi_C \|\right)$ of the matrix diagonal. As a result of the semi-implicit source term treatment, the mass transfer coefficients are included in the a_C coefficient in both the γ transport and the pressure equation. Due to the normalization by $\max\left(\| a_C \phi_C \|\right)$, the L_1 norm can be artificially reduced, while the solution quality itself has actually not improved.

Furthermore, Fig. 2.10 shows that the peak pressures caused by the bubble collapse at different observation points converge with increasing condensation coefficient C_c for a fixed time step size Δt. However, no convergent behavior is achieved with respect to Δt, where the peak pressure $p_{\max}$ tends to increase linearly with decreasing Δt and at approximately the factor at which Δt decreases.

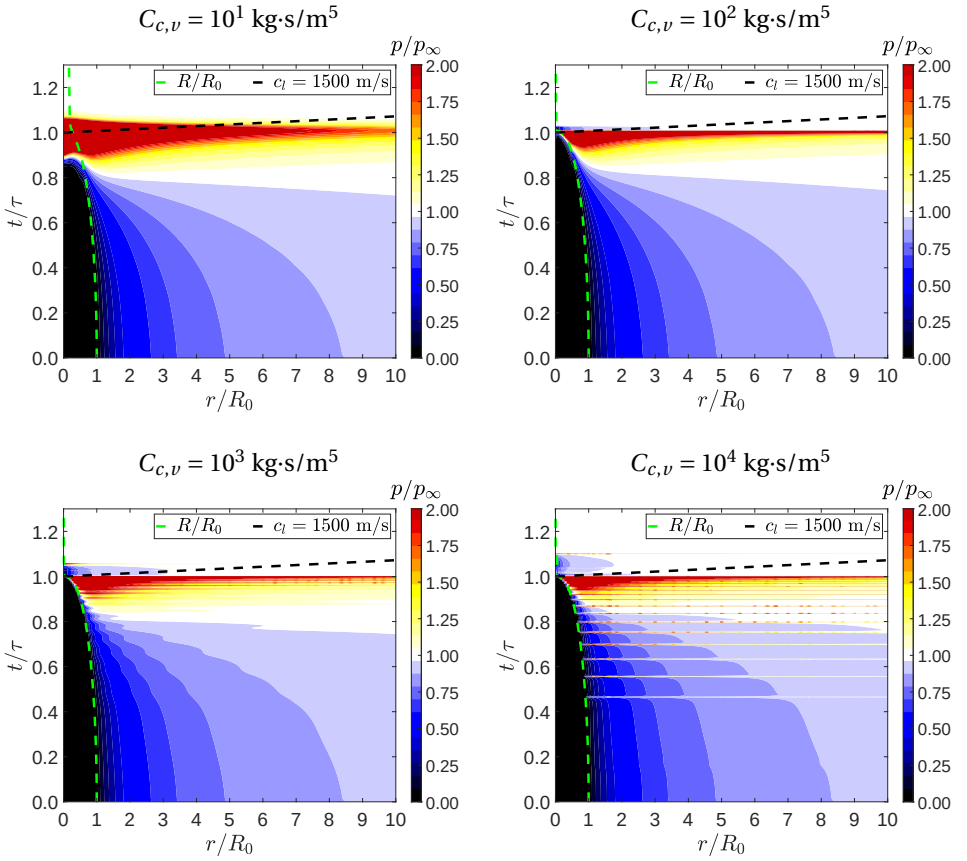

Figure 2.8: Non-dimensional pressure p/p_∞ over the non-dimensional distance r/R_0 from the bubble center and over the non-dimensional time t/τ for a variation of the mass transfer coefficients $C_{c,v}$, where R_0 is the initial bubble radius and τ the Rayleigh collapse time [33]; the slope of the black dashed line indicates the liquid sound speed $c_l = 1500$ m/s and the green dashed line indicates the evolution of the bubble interface, where the instantaneous interface position is reconstructed from $R = \left[3V_{\text{vap}}/(4\pi)\right]^{1/3}$, with V_{vap} being the instantaneous vapor volume in the domain.

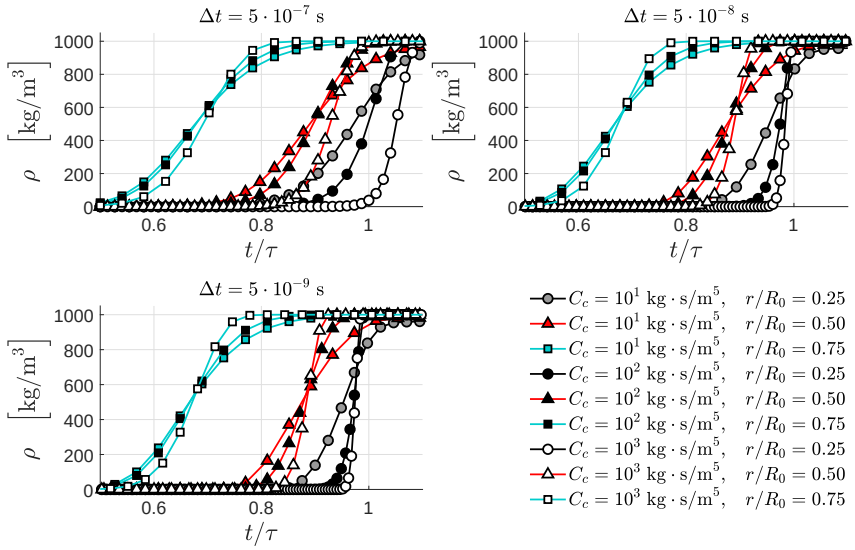

Figure 2.9: Evolution of the mixture density ρ versus time during the condensation process for the same three observation points, condensation rates and time step sizes as in Fig. 2.6.

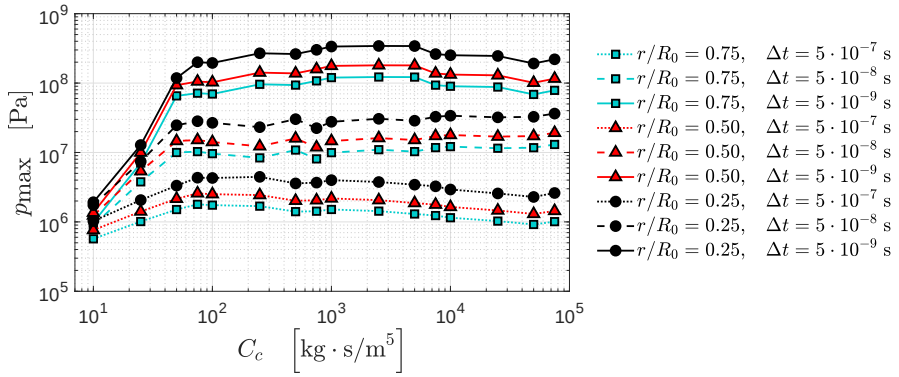

Figure 2.10: Collapse peak pressure over the condensation mass transfer coefficient value C_c at different observation points r/R_0 and for different time step sizes Δt.

2.3.3. IMPLICATIONS WITH RESPECT TO CAVITATION EROSION MODELING

Together with the instantaneous occurrence of the collapse peak pressure in the entire flow domain due to the incompressibility of the pure liquid phase, the non-convergent behavior of the pressure peaks strongly indicates that cavitation erosion indicators based on the local pressure are not able to reliably predict the erosive aggressiveness of a cavitating flows within the presented numerical frame work. A similar conclusion was drawn by Eskilsson and Bensow [70]. Based on their comparative study on the capability of several erosion indicators available in literature, they also highlight the need for further development in this field [70]. As far as the kinematic features of the cavity collapse are concerned, e.g. the cavity collapse time, semi-empirical mass transfer models give accurate predictions in the limit of large mass transfer coefficients and sufficient temporal resolution. In Sec. 4.3, it is further demonstrated that also the characteristic shedding frequency of periodic cavitating flows and the time averaged vapor content exhibit convergent behavior in the limit of large coefficient values. This suggests that the prediction of cavitation implosion loads should preferably be determined from the kinematic evolution of the imploding vaporous structures.

3

DEVELOPMENT OF A CAVITATION IMPLOSION LOAD MODEL

Against the findings from the previous chapter, a model is developed which couples the kinematics of the cavity collapse to the implosion load via the potential energy content [12] $E_{\text{pot}} = V\left(p_d - p_v\right)$ of the collapsing cavity, where V is the cavity volume and p_d the collapse driving pressure. Analytical considerations on an isolated vapor bubble collapse, mostly based on existing literature, are presented in Sec. 3.1.

The analytical considerations on the simplifying situation of the isolated spherical collapse build the foundation of the modeling approach by linking the potential energy content to the equations of motion of the collapsing bubble and the surrounding liquid as well as the energy content of the pressure wave radiated at the final stage of the collapse, which is interpreted as an acoustic wave in this modeling framework. Under some modeling assumptions, the energy balance of the collapsing bubble is rewritten in a local form for arbitrary flow situations. In particular, the non-trivial role of the driving pressure p_d is discussed in more detail.

In Sec. 3.2.1, a novel transport equation of collapse induced kinetic energy is derived to account for the kinetic energy that a cavity collapse induces in the liquid flow. As a result, a focusing of collapse energy into the collapse center is obtained. The transport equation is formulated in such a way that it can also account for the energy focusing mechanism in a collective vapor bubble cloud collapse as described by Wang and Brennen [16]. Similar to the work by Leclercq et al. *[27], a projection approach is employed to convert the energy radiated from the source location into local acoustic impact power and acoustic pressure.*

The numerical implementation of the acoustic implosion load model is subject of Sec. 3.3. Most importantly, a computationally efficient approach is presented to obtain accumulated surface energy distributions from the model. Sec. 3.4 presents a statistical analysis method to isolate extreme events from accumulated surface energy distributions.

Parts of this chapter were published in Physics of Fluids **31**, 052102 (2019) [1] and in the International Journal of Multiphase Flow **111**, 200 (2019) [2].

3.1. CONSIDERATIONS ON THE POTENTIAL CAVITY ENERGY

3.1.1. INSTANTANEOUS ENERGY BALANCE OF THE ISOLATED BUBBLE COLLAPSE

The potential energy hypothesis [11, 12] implies that the potential energy of a cavity is equal to the work that the driving pressure difference $p_d - p_v$ can do on its vapor volume throughout the collapse, where p_d is the driving pressure and p_v the vapor pressure. During the collapse, the initial potential cavity energy $E_{\text{pot},0}$ can be partitioned into different forms of energy, such that the total energy amount $E_{\text{pot},0}$ is conserved at any time instant [13, 14]. In order to discuss the relevance of the instantaneous energy balance with respect to cavitation implosion loads, we first consider the simplified case of an isolated vapor bubble collapse. In this case, the driving pressure p_d is equal to the ambient pressure p_∞ and the potential cavity energy reduces to the potential bubble energy [12]

$$E^b_{\text{pot},0} = \frac{4}{3}\pi R_0^3 \left(p_\infty - p_v\right), \tag{3.1}$$

where R_0 is the initial bubble radius, and where the superscript b indicates that the relation is valid for a spherical undisturbed bubble. In order to formulate the instantaneous energy balance during the collapse process, the entire liquid body around the collapsing bubble needs to be taken into account [13]. As the bubble collapses, its potential energy decreases. The reduction of potential energy feeds into kinetic energy of the liquid body. The local kinetic energy per unit volume at some distance r from the center is $1/2\rho_l \|\mathbf{u}\|^2(r,t)$. Given the spherical symmetry of the problem, it is convenient to integrate the kinetic energy per unit volume over the surface of a sphere around the bubble center, which gives the radial kinetic energy density. With the continuity relation $r^2\|\mathbf{u}\| = R^2\dot{R}$ for constant liquid density and $r > R$, the instantaneous radial kinetic energy density at some distance r from the bubble center becomes

$$\frac{dE_{\text{kin}}}{dr} = 2\pi\rho_l R^4 \frac{\dot{R}^2}{r^2} \quad \text{for} \quad r \geq R, \tag{3.2}$$

where $R = R(t)$ is the instantaneous bubble radius. The instantaneous kinetic energy of the entire liquid body follows from the radial integration of Eqn. (3.2), which gives [13]

$$E^b_{\text{kin}} = \int_R^\infty \left(\frac{dE_{\text{kin}}}{dr}\right) dr = 2\pi\rho_l \dot{R}^2 R^3 \tag{3.3}$$

and hence the instantaneous change of kinetic energy around the collapsing bubble becomes [71]:

$$\frac{dE^b_{\text{kin}}}{dt} = 2\pi\rho_l R^2 \dot{R}\left[2R\ddot{R} + 3\dot{R}^2\right] \tag{3.4}$$

From Eqn. (3.1) follows the change of potential energy :

$$\frac{dE^b_{\text{pot}}}{dt} = 4\pi R^2 \dot{R}\left(p_\infty - p_v\right) \tag{3.5}$$

As pointed out by Obreschkow *et al.* [13], the change of kinetic energy in the liquid body and the change of potential bubble energy must cancel out each other, such that

$$\frac{dE^b_{\text{pot}}}{dt} + \frac{dE^b_{\text{kin}}}{dt} = 0, \tag{3.6}$$

which gives the Rayleigh equation [13, 33]

$$R\ddot{R} + \frac{3}{2}\dot{R}^2 = -\frac{p_\infty - p_v}{\rho_l}. \tag{3.7}$$

Substituting the analytical solution [33]

$$\dot{R} = -\sqrt{\frac{2}{3}\frac{p_\infty - p_v}{\rho_l}\left(\frac{R_0^3}{R^3} - 1\right)} \tag{3.8}$$

into Eqn. (3.3), one finds that

$$E^b_{\text{kin}}(R = 0) = E^b_{\text{pot},0}. \tag{3.9}$$

This means that the initial potential bubble energy is fully converted into kinetic energy as the final collapse stage is approached. Also, the kinetic energy around a spherical collapsing bubble focuses towards the bubble interface over time. This is shown by combining Eqn. (3.2) with the analytical solution for $\dot{R}$ given by Eqn. (3.8), which gives the dimensionless radial kinetic energy density at some distance r from the collapse center:

$$\left(\frac{dE^b_{\text{kin}}}{dr}\right)^* = \frac{R_0}{E_{\text{pot},0}}\frac{dE^b_{\text{kin}}}{dr} = \left(\frac{R_0}{r}\right)^2 \frac{R}{R_0}\left[1 - \left(\frac{R}{R_0}\right)^3\right] \tag{3.10}$$

Evaluating Eqn. (3.10) at the interface shows that $\lim_{R\to 0}\left(dE^b_{\text{kin}}/dr\right)^*_{r=R} = \infty$, which means that the radial kinetic energy density at the bubble interface tends towards infinity as the final collapse stage is approached. As we further know from Eqn. (3.9) that the kinetic energy of the entire liquid body around the bubble approaches the finite value $E^b_{\text{pot},0}$, we can conclude that all the kinetic energy of the liquid body focuses into the collapse center at the final collapse stage. The focusing of kinetic energy is illustrated by Fig. 3.1, which depicts the radial distribution of the dimensionless kinetic energy density given by Eqn. (3.10) for different bubble radii, i.e. for different time instants of the bubble collapse. According to these simplified considerations, the shock wave emitted at the final collapse stage propagates from an idealized point source. The relation between the power radiation $\partial e_{\text{rad}}/\partial t$ associated with the shock and the acoustic pressure p_a at some distance r from the source is given by [15]

$$p_a^2(t, r) = \frac{\rho_l c_l}{4\pi r^2}\frac{\partial e_{\text{rad}}}{\partial t}. \tag{3.11}$$

With T_{SW} being the pulse duration at some distance r from the source, the radiated shock wave energy is then given by [15]

$$E_{SW} = \frac{4\pi r^2}{\rho_l c_l}\int_{T_{SW}} p_a^2(t, r)\, dt. \tag{3.12}$$

As discussed by Tinguely *et al.* [14], the initial potential bubble energy is eventually partitioned into shock wave energy, dissipative thermal energy, and rebound energy, where they show the latter to be relevant for low ambient pressures significantly below 1 bar only. Thermal dissipation was shown to be negligible [14]. Under these circumstances, the shock wave energy E_{SW} is approximately equal to the initial potential bubble energy $E^b_{\text{pot},0}$. In addition to the energy balance by Tinguely *et al.* [14], which addresses the collapse of spherical bubbles in particular, we also mention that some residual kinetic energy may remain in the flow due to asymmetries in the collapse. This residual kinetic energy may again transform into potentially erosive energy forms, e.g. the waterhammer and stagnation pressure imposed by the impinging liquid jet forming during the collapse of a near wall vapor bubble [5]. The energy partition is further affected by the presence of non-condensable gas, where the size of the rebound bubble tends to increase with increasing gas content [72].

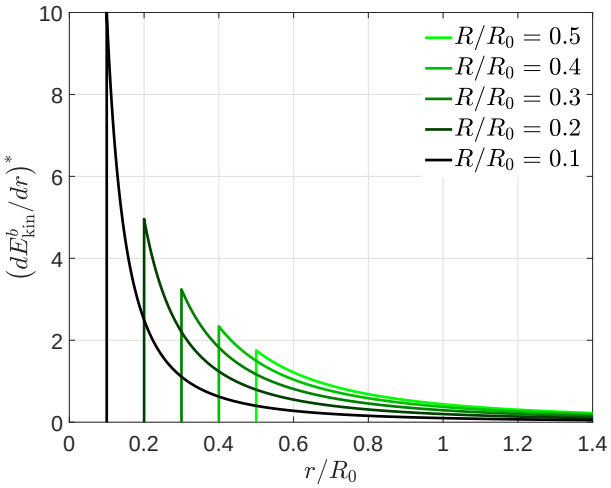

Figure 3.1: Distribution of the dimensionless radial kinetic energy density around a collapsing vapor bubble (see Eqn. (3.10)) for different time instants associated with the corresponding bubble radii R/R_0; the integral of each curve represents the kinetic energy of the entire liquid body as given by Eqn. (3.3).

3.1.2. COLLAPSE POTENTIAL IN ARBITRARY FLOW SITUATIONS

A local formulation of the cavity potential suitable for arbitrarily shaped cavities is obtained from the vapor fraction $1-\gamma$ [73], such that

$$e_{\text{pot}} = (1-\gamma)(p_d - p_v). \tag{3.13}$$

For arbitrary flow situations, the ambient pressure p_∞ is replaced by the collapse driving pressure $p_d(t,\mathbf{x})$. The driving pressure is still interpreted as an ambient condition, which, however, is not necessarily constant in space and time. Integration of Eqn. (3.13) over the vapor mixture volume gives the total amount of potential cavity energy

$$E_{\text{pot}} = \int_{\text{v.vol}} (1-\gamma)(p_d - p_v)\, dV. \tag{3.14}$$

The time derivative of the total potential is

$$\frac{dE_{\text{pot}}}{dt} = -\int_{\text{v.vol}} \frac{D\gamma}{Dt}(p_d - p_v)\, dV + \int_{\text{v.vol}} (1-\gamma)\frac{Dp_d}{Dt} dV. \tag{3.15}$$

The change of vapor volume induces a flow in the surrounding liquid. This condensation/evaporation induced liquid flow, denoted by $\mathbf{u}_{c,v}$, is a component of the total liquid flow velocity $\mathbf{u}$. The liquid volume integral of the induced kinetic energy is then given by

$$E_{\text{kin},c,v} = \frac{1}{2}\int_{\text{l.vol}} \rho_l \mathbf{u}_{c,v} \cdot \mathbf{u}_{c,v} dV, \tag{3.16}$$

and the time derivative of Eqn. (3.16) is

$$\frac{dE_{\text{kin},c,v}}{dt} = \int_{\text{l.vol}} \rho_l \mathbf{u}_{c,v} \cdot \frac{\partial \mathbf{u}_{c,v}}{\partial t} dV + \frac{1}{2}\int_{\text{l.vol}} \frac{D\rho_l}{Dt} \mathbf{u}_{c,v} \cdot \mathbf{u}_{c,v} dV. \tag{3.17}$$

As stated by Eqn. (3.6), the change of potential cavity energy must balance the change of induced liquid kinetic energy in case of an isolated cavity collapse at constant ambient pressure [13]. In that case, the system consisting of the vapor cavity and the surrounding liquid can approximately be considered as conservative, meaning that no external energy source or energy dissipation [14] is involved in the energy conversion. For non-conservative systems, Eqn. (3.6) is rewritten as

$$\frac{dE_{\text{pot}}}{dt} + \frac{dE_{\text{kin},c,v}}{dt} = \frac{dW}{dt}, \tag{3.18}$$

where W represents an external or dissipative source that can feed energy into the system or extract energy from the system. Substituting Eqns. (3.15) and (3.17) into Eqn. (3.18) and assuming the liquid phase to be incompressible ($D\rho_l/Dt = 0$) gives the following instantaneous energy balance:

$$-\int_{\text{v.vol}} \frac{D\gamma}{Dt}(p_d - p_v)\, dV + \rho_l \int_{\text{l.vol}} \mathbf{u}_{c,v} \cdot \frac{\partial \mathbf{u}_{c,v}}{\partial t} dV + \int_{\text{v.vol}} (1-\gamma)\frac{Dp_d}{Dt} dV + = \frac{dW}{dt} \tag{3.19}$$

The first two terms on the left-hand side of Eqn. (3.19) describe the instantaneous conversion of potential cavity energy into kinetic liquid energy due to cavity volume changes. They are directly coupled to each other via continuity of the incompressible liquid, because the induced liquid flow must follow the collapsing or growing cavity interfaces in such a way that $\nabla \cdot \mathbf{u}_{c,v} = 0$. This means that only the first term on the left-hand side of Eqn. (3.19) can directly feed into the induced flow velocity $\mathbf{u}_{c,v}$. The third term on the left-hand side of Eqn. (3.19) represents the change of collapse driving pressure at constant cavity volume ($D\gamma/Dt = 0$) and is balanced by the source term dW/dt.

Further defining the $\{\}^+$ and $\{\}^-$ operators applied to some scalar quantity $\bullet$ as

$$\{\bullet\}^+ := \max[\bullet, 0], \quad \{\bullet\}^- := \min[\bullet, 0], \tag{3.20}$$

the local change of potential energy per unit volume can be written as follows:

$$\frac{De_{\text{pot}}}{Dt} = \underbrace{-\left(p_d - p_v\right)\left\{\frac{D\gamma}{Dt}\right\}^{+}}_{\left(De_{\text{pot}}/Dt\right)_c} \underbrace{-\left(p_d - p_v\right)\left\{\frac{D\gamma}{Dt}\right\}^{-}}_{\left(De_{\text{pot}}/Dt\right)_v} + \underbrace{\left(1-\gamma\right)\frac{Dp_d}{Dt}}_{\text{change of the ambient condition}} \tag{3.21}$$

The terms $\left(De_{\text{pot}}/Dt\right)_c$ and $\left(De_{\text{pot}}/Dt\right)_v$ in Eqn. (3.21) represent the material derivative of the potential energy e_{pot} due to condensation and evaporization, respectively. The third term on the right-hand side of Eqn. (3.21) is interpreted as the change of the ambient condition experienced at a certain location in the mixture phase. From the interpretation of Eqn. (3.19) follows that only $\left(De_{\text{pot}}/Dt\right)_c$ can directly feed into collapse induced kinetic energy, which is again converted into radiated shock wave energy at the final collapse stage. Nevertheless, an increase of the driving pressure p_d during a cavity collapse enhances the collapse aggressiveness, because it increases the driving pressure difference in the term $\left(De_{\text{pot}}/Dt\right)_c$ over time. This is further discussed by following an associated Lagrangian particle and by expanding p_d in time using a first-order Taylor series expansion, which gives

$$p_d^{\mathfrak{L}}\left(t+\Delta t\right) = p_d\left(t\right) + \underbrace{\left(\frac{\partial p_d}{\partial t}\right)_t \Delta t + \left(\mathbf{u}\cdot\nabla p_d\right)_t \Delta t}_{\left(Dp_d/Dt\right)_t \Delta t} + \mathcal{O}\left(\Delta t^2\right). \tag{3.22}$$

The superscript $\mathfrak{L}$ on the left-hand side of Eqn. (3.22) indicates that the Taylor series expansion is carried out in the Lagrangian reference frame. The second term on the right-hand side of Eqn. (3.22) represents the change of the driving pressure due to the unsteadiness of the driving pressure field, and the third term represents the change of driving pressure experienced by an associated Lagrangian particle as it moves along the driving pressure gradient. This interpretation of the driving pressure reflects that it is thought of as an ambient condition to which the associated Lagrangian particle is subjected, rather than a material property transported by the particle itself. In other words, the derivative $\mathbf{u}\cdot\nabla p_d$ is only visible in the Lagrangian reference frame, whereas the advective derivative of a transported quantity is only visible in the Eulerian reference frame.

An illustrative example to further motivate this interpretation is given by a vapor bubble collapsing along a driving pressure gradient, such that $\mathbf{u}\cdot\nabla p_d > 0$ and $p_d\left(\mathbf{x}\right) = \text{const}$. As far as the change of potential energy according to Eqn. (3.21) is concerned, the increase of driving pressure and the reduction of bubble volume counteract each other in this situation, because $\left(De_{\text{pot}}/Dt\right)_c < 0$ and $Dp_d/Dt > 0$. However, employing the Lagrangian time expansion of p_d given by Eqn. (3.22), one finds that the reduction of vapor volume and the increase of driving pressure both work in the same direction in the sense that they both feed into collapse induced kinetic energy, which can eventually be converted into shock wave energy at the final stage of the collapse. Such a flow situation is likely to occur in cavitating flows along lifting bodies, where vapor cavities can implode into a region of pressure recovery. If p_d is uniform in space but not in time, the bubble experiences a variation of the driving pressure over time due to the unsteady term

$\partial p_d/\partial t$ in Eqn. (3.22). As the first two terms on the left-hand side of the instantaneous energy balance given by Eqn. (3.19) must balance each other, an increase of p_d implies that $dW/dt > 0$. This means that energy feeds into the system, which is responsible for the increase of p_d. On the other hand, a decrease of p_d means that energy dissipates from the system ($dW/dt < 0$), which might be the result of a viscous pressure drop for example.

It is concluded from the above considerations that the collapse induced kinetic energy of the liquid phase, fed by the volume reduction of the imploding cavities, plays a key role in the energy cascade from potential cavity energy into radiated shock wave energy. The local kinetic energy of the condensation induced flow is denoted by $e_{\mathrm{kin},c}$, and the total kinetic energy e_{kin} per unit volume is formally decomposed into the condensation induced component, an evaporization induced component $e_{\mathrm{kin},v}$, and a purely advective component $e_{\mathrm{kin},a}$, such that

$$e_{\mathrm{kin}}(t,\mathbf{x}) = e_{\mathrm{kin},c}(t,\mathbf{x}) + e_{\mathrm{kin},v}(t,\mathbf{x}) + e_{\mathrm{kin},a}(t,\mathbf{x}). \tag{3.23}$$

The condensation as well as the evaporization induced liquid flow can only exist because of the presence of divergence sources in which the mixture flow is compressed or expanded, respectively. The condensation/evaporization induced liquid flow itself, however, is (approximately) divergence free. Therefore, the distribution of the collapse induced kinetic energy $e_{\mathrm{kin},c}$, which feeds into the radiated shock wave energy, cannot directly be extracted from the flow velocity field.

3.1.3. COLLAPSE DRIVING PRESSURE

The driving pressure p_d, which is effectively driving the cavity collapse, involves the largest uncertainty in defining the potential energy content of a cavitating flow. This quantity is typically unknown in complex flow situations. An example would be the cavitating flow around a hydrofoil or any other obstacle, where pressure recovery gradients along the obstacle are important for the dynamics of the cavitating flow. For a bubble collapsing close to a solid wall, the driving pressure across its interface varies due to the effect of wall interaction, leading to deformation of the bubble and, finally, to the formation of a liquid jet impacting the wall [5]. Even for an isolated bubble, the presence of the hydrostatic pressure gradient leads to deformation at a certain stage of the collapse [74]. Thus, the driving pressure is practically never exactly constant in space. An approach to determine the driving pressure in complex flow situations is suggested and implemented by Arabnejad and Bensow [25]. In their work, coherent cavition structures are identified and simplified to an isolated spherical bubble of equivalent volume. Thus, the driving pressure can be determined from the Rayleigh-Plesset equation [33, 75] and a set of kinematic parameters uniquely defining the state of the collapse [24]. However, this is at the cost of not reflecting the exact shape of the collapsing structure and its orientation relative to the impacted surface.

In order to provide an approximation of the conditions to which arbitrarily shaped cavities are subjected, the time averaged pressure [68]

$$p_d(t^*) = \langle p \rangle_{t^*} = \frac{1}{T_{\mathrm{mov}}} \int_{t^*-T_{\mathrm{mov}}}^{t^*} p(t)\,dt, \quad \text{where } t^* \geq T_{\mathrm{mov}}, \tag{3.24}$$

is proposed as a measure of the collapse driving pressure. The average given by Eqn. (3.24) is a moving average over a time window of size T_{mov} that can be adjusted to the periodicity of the flow.

3.2. CONVERSION OF POTENTIAL ENERGY INTO SURFACE IMPACT POWER

3.2.1. TRANSPORT EQUATION OF COLLAPSE INDUCED KINETIC ENERGY

It was shown in Sec. 3.1.1 that the potential energy is gradually converted into kinetic energy [13] and focused into the collapse center, where it is eventually released in a shock wave. With this in mind, the reduction of potential cavity energy due to condensation is absorbed into the accumulated collapse induced kinetic energy field $e_{\mathrm{kin},c}(t,\mathbf{x})$ until a criterion for the conversion of this kinetic energy into radiated acoustic energy is met. This process can formally be expressed by a transport equation of collapse induced kinetic energy, given by

$$\frac{\partial e_{\mathrm{kin},c}}{\partial t} - (1-\beta)\,\phi\left(e_{\mathrm{kin},c}\right) = -(1-\beta)\left(\frac{De_{\mathrm{pot}}}{Dt}\right)_c - \beta\frac{\partial e_{\mathrm{kin}\to\mathrm{rad}}}{\partial t}. \tag{3.25}$$

The terms $\left(De_{\mathrm{pot}}/Dt\right)_c$ and $\partial e_{\mathrm{kin}\to\mathrm{rad}}/\partial t$ in Eqn. (3.25) represent the conversion of potential cavity energy into kinetic energy and the conversion of collapse induced kinetic energy into radiated acoustic energy, respectively. Therefore, they are both interpreted as source terms in the kinetic energy balance. Physical models are needed to describe both processes.

The term $\phi\left(e_{\mathrm{kin},c}\right)$ represents the conservative advective transport of $e_{\mathrm{kin},c}$, which is responsible for the spatial focusing of the accumulated kinetic energy. The fraction β is either 1 or 0 based on a local flow condition to identify the final collapse stage. By this means, β activates either the radiation source term or the kinetic energy flux term in such a way that the overall amount of energy is conserved. From Eqn. (3.6), it is known that the amount of collapse induced kinetic energy in the entire liquid body is equal to the change of potential energy that the collapsing cavities have undergone, such that

$$\underbrace{\int_{\mathrm{vol}} \frac{\partial e_{\mathrm{kin},c}}{\partial t}\,dV}_{dE_{\mathrm{kin},c}/dt} + \underbrace{\int_{\mathrm{vol}} \left(\frac{De_{\mathrm{pot}}}{Dt}\right)_c dV}_{\left(dE_{\mathrm{pot}}/dt\right)_c} = 0. \tag{3.26}$$

However, the exact spatial distribution of $e_{\mathrm{kin},c}$ is unknown. For this reason, the conservative transport of the accumulated kinetic energy requires a modeling assumption as well. We essentially assume that locations of potential energy reduction act as attractors of the collapse induced kinetic energy that is already present in the flow field. Based on this consideration, we further assume that this kinetic energy can be absorbed by the interface of the collapsing cavities until a criterion for the conversion of this energy into radiated acoustic energy is met. To this end, the actual collapse induced kinetic energy distribution $e_{\mathrm{kin},c}(t,\mathbf{x})$ is absorbed into the cavity interface region $\mathbf{x}_P$, where the collapse induced kinetic energy distribution is then represented by the artificial quantity

$$\mathscr{E}(t,\mathbf{x}_P) = e_{\mathrm{kin},c}(t,\mathbf{x}\rightarrow\mathbf{x}_P), \quad \text{such that} \quad \delta s \oint_{\text{cav. surf.}} \mathscr{E}(t,\mathbf{x}_P)\, dS = \int_{\text{vol}} e_{\mathrm{kin},c}(t,\mathbf{x})\, dV. \tag{3.27}$$

Eqn. (3.27) states that the volume integral over the actual collapse induced kinetic energy $e_{\mathrm{kin},c}$ must be equal to the cavity surface integral of the absorbed kinetic energy $\mathscr{E}$ times an associated cavity interface thickness δs, which can be considered as arbitrarily small. As a result of the artificial kinetic energy absorption, the model cannot correctly reflect the spatial kinetic energy distribution around the cavity before the final collapse stage. At the final collapse stage, however, where the kinetic energy is shown to entirely focus into the collapse center (see Sec. 3.1.1), the model approaches the correct representation of the kinetic energy distribution. With the above definitions, Eqn. (3.25) is rewritten as

$$\frac{\partial \mathscr{E}}{\partial t} = \underbrace{(1-\beta)\left[\phi(\mathscr{E}) - \left(\frac{De_{\mathrm{pot}}}{Dt}\right)_c\right]}_{\text{kinetic energy flux}} - \underbrace{\beta\frac{\partial \mathscr{E}_{\mathrm{rad}}}{\partial t}}_{\text{radiated energy flux}}. \tag{3.28}$$

As indicated by Eqn. (3.28), the generation of kinetic energy, given by the negative change of potential energy $\left(De_{\mathrm{pot}}/Dt\right)_c$, as well as the conservative kinetic energy transport $\phi(\mathscr{E})$ contribute to the kinetic energy flux. The negative change of potential energy is given by [73]

$$\left(\frac{De_{\mathrm{pot}}}{Dt}\right)_c = -\left\{\frac{D\gamma}{Dt}\right\}^+ (p_d - p_v). \tag{3.29}$$

The positive material derivative of γ directly follows from the continuity equation expressed in terms of the liquid fraction γ:

$$\left\{\frac{D\gamma}{Dt}\right\}^+ = -\{\nabla\cdot\mathbf{u}\}^- \frac{\rho}{\rho_l - \rho_v} \tag{3.30}$$

In order to derive an appropriate model for the conservative transport term $\phi(\mathscr{E})$ in Eqn. (3.28), $\phi(\mathscr{E})$ is formally decomposed into a production term and a reduction term, such that

$$\phi(\mathscr{E}) = \{\phi(\mathscr{E})\}^+ + \{\phi(\mathscr{E})\}^-. \tag{3.31}$$

For the amount of transported energy to be conserved, the transport term must satisfy

$$\int_{\text{vol}} \left[\{\phi(\mathscr{E})\}^+ + \{\phi(\mathscr{E})\}^-\right] dV = 0. \tag{3.32}$$

It is first assumed that the reduction rate given by $\{\phi(\mathscr{E})\}^-$ is proportional to $\mathscr{E}$ to ensure that $\mathscr{E} \geq 0$ everywhere. Secondly, the fraction of $\mathscr{E}$ reduced by $\{\phi(\mathscr{E})\}^-$ per time δt is assumed to be given by the normalized projection of $\nabla\mathscr{E}(\mathbf{x}_P)$ on the local flow velocity vector $\mathbf{u}(\mathbf{x}_P)$. With the projection operator

$$\mathfrak{P}_{\mathbf{u}}(\nabla\mathscr{E}) := \frac{\{\mathbf{u}\cdot\nabla\mathscr{E}\}^+}{\|\mathbf{u}\|\,\|\nabla\mathscr{E}\|} \quad \in [0,1], \tag{3.33}$$

this gives

$$\{\phi(\mathscr{E})\}^- = \begin{cases} -\dfrac{\mathscr{E}}{\delta t}\mathfrak{P}_{\mathbf{u}}(\nabla\mathscr{E}), & \text{for: } \|\mathbf{u}\| > 0 \wedge \|\nabla\mathscr{E}\| > 0 \\ 0, & \text{elsewhere.} \end{cases} \tag{3.34}$$

This formulation is motivated by the assumption that the flow at the interface of a collapsing cavity is directed into the collapse center and therefore aligned with $\nabla\mathscr{E}$, since $\mathscr{E}$ is stored in the cavity interface. The underlying assumption for the formulation of the production term $\{\phi(\mathscr{E})\}^+$ is that the kinetic energy accumulated throughout the cavity collapse is attracted by locations where kinetic energy is induced by the collapse. To this end, it is assumed that $\{\phi(\mathscr{E})\}^+$ is proportional to $-\left(De_{\text{pot}}/Dt\right)_c$, such that $\{\phi(\mathscr{E})\}^+ = -k\left(De_{\text{pot}}/Dt\right)_c$, where k is assumed to be constant in space and must be determined such that

$$-k\int_{\text{vol}}\left(\frac{De_{\text{pot}}}{Dt}\right)_c dV = -\int_{\text{vol}}\{\phi(\mathscr{E})\}^- dV \tag{3.35}$$

at any time instant to comply with the conservation requirement given by Eqn. (3.32). Thus, we get

$$\{\phi(\mathscr{E})\}^+ = -k\left(\frac{De_{\text{pot}}}{Dt}\right)_c, \quad \text{where} \quad k = \begin{cases} -\dfrac{\int_{\text{vol}}\frac{\mathscr{E}}{\delta t}\mathfrak{P}_{\mathbf{u}}(\nabla\mathscr{E})\,dV}{\int_{\text{vol}}\left(\frac{De_{\text{pot}}}{Dt}\right)_c dV}, & \text{for: } \left(\frac{De_{\text{pot}}}{Dt}\right)_c < 0 \\ 0, & \text{elsewhere.} \end{cases} \tag{3.36}$$

A conceptually similar mechanism to describe the interaction between cavitation bubbles based on the volume distribution of the velocity divergence field was proposed by Maiga *et al.* [76]. Combining the above equations, Eqn. (3.28) becomes

$$\frac{\partial\mathscr{E}}{\partial t} = \underbrace{(1-\beta)\left[-(1+k)\left(\frac{De_{\text{pot}}}{Dt}\right)_c - \frac{\mathscr{E}}{\delta t}\mathfrak{P}_{\mathbf{u}}(\nabla\mathscr{E})\right]}_{\text{kin. energy flux}} - \beta\frac{\partial\mathscr{E}_{\text{rad}}}{\partial t}, \tag{3.37}$$

where $\left(De_{\text{pot}}/Dt\right)_c$, $\mathfrak{P}_{\mathbf{u}}(\nabla\mathscr{E})$ and k are specified by Eqns. (3.29), (3.33) and (3.36), respectively. With the model terms for $\{\phi(\mathscr{E})\}^-$ and $\{\phi(\mathscr{E})\}^+$ given by Eqns. (3.34) and (3.36), respectively, the conservative transport term $\phi(\mathscr{E})$ is not continuous in the sense of an advection term, because the conservation of $\mathscr{E}$ is enforced by an integral balance for k in Eqn. (3.36). However, this approach allows to redistribute the collapse induced kinetic energy between coherent vapor structures in situations where they are interacting with each other. This interaction plays an essential role in the collapse of densely populated vapor bubble clouds [16] and is further discussed in Sec. 3.2.2.

3.2.2. ENERGY RADIATION - ENERGY FOCUSING VS NO ENERGY FOCUSING

The fraction $0 \leq \beta \leq 1$ in Eqn. (3.28), which is splitting the local energy flux into a kinetic energy flux and a radiated energy flux, essentially is an identifier of the final collapse stage. If the energy radiation is considered as a discrete event, β becomes a Heaviside

function, such that $\beta = 1$ at the final collapse stage and otherwise $\beta = 0$. The task is then to find an adequate criterion to identify the final collapse stage. Most obviously, all the vapor must be condensed at the final collapse stage ($\gamma = 1$). In case of an isolated cavity collapse, this criterion would already be sufficient. In case of a collective vapor bubble cloud collapse, however, a second criterion is needed. The reason for this is illustrated by Fig. 3.2. In a cloud, where the bubbles are so densely packed that the pressure can hardly recover in the liquid phase between the bubbles, the bubble cloud tends to be behave like a homogeneous mixture of equivalent vapor fraction [16, 17], whose collapse is driven by the difference between the distant ambient pressure and the low pressure inside the cloud. As a result, the kinetic energy of the liquid phase accumulates upstream from a discontinuity, which can be seen as the cloud interface and which is propagating towards the cloud center as the cloud collapses. Wang and Brennen [16] have identified this discontinuity as an inward directed condensation shock, which implies a sharp pressure jump from the low cloud pressure to the upstream side of the condensation shock front. This has the effect that prior to shock wave radiation, the energy of the individual bubbles is not only transported into the individual bubble centers, but also further towards the center of the collective cloud. In order to allow for this transport mechanism, the kinetic energy flux is assumed to remain active as long as the local pressure has not exceeded the ambient pressure. This suggests the following Heaviside function for β:

$$\beta = H(\gamma, p) = \begin{cases} 1 & \text{for} \quad p > p_\infty \text{ and } \gamma = 1 \\ 0 & \text{otherwise} \end{cases} \tag{3.38}$$

With this formulation, the transport term in Eqn. (3.28) can fully focus the collapse induced kinetic energy $\mathscr{E}$ into the collapse center before the conversion into radiated shock wave energy takes place. Releasing the energy $\mathscr{E}$ in a discrete event within a time δt, the radiated energy flux is modeled by,

$$\frac{\partial e_{\text{rad}}}{\partial t} = \beta \frac{\partial \mathscr{E}_{\text{rad}}}{\partial t} = \frac{\mathscr{E}}{\delta t} \tag{3.39}$$

and the transport equation of $\mathscr{E}$ given by Eqn. (3.37) becomes

$$\frac{\partial \mathscr{E}}{\partial t} = (1-\beta)\left[-(1+k)\left(\frac{De_{\text{pot}}}{Dt}\right)_c + \frac{\mathscr{E}}{\delta t}\left(1 - \mathfrak{P}_{\mathbf{u}}(\nabla \mathscr{E})\right)\right] - \frac{\mathscr{E}}{\delta t}. \tag{3.40}$$

From Eqn. (3.39) then follows that $\partial e_{\text{rad}}/\partial t \to \infty$ as $\delta t \to 0$. This is the equivalent situation to the events at the final collapse stage of an isolated vapor bubble, as found from the simplified considerations in Sec. 3.1.1, where the energy density in the collapse center tends to infinity at the final collapse stage, although the absolute amount of energy remains finite. This behavior is the result of not resolving the events at the finite collapse stage, which eventually determine the exact energy density distribution within the radiated pressure wave. This energy density distribution is formally reflected by Eqn. (3.12), where the total amount of shock wave energy E_{SW} is proportional to the time integral of p_a over the impact duration T_{SW} as the wave passes some arbitrary location at a distance r from the center. Practically, this means that the radiation time δt is equal to the simulation time step size Δt. By this means, the energy content of the radiated shock

wave is consistently predicted, but an entirely time accurate solution for the shape of the impact power signal cannot be expected from this approach.

In order to investigate the effect of energy focusing due to the kinetic energy involved in the collapse process, a second model formulation was considered in which the conversion of potential energy into kinetic energy is omitted. In that case, the change of potential energy at negative flow divergence (condensation) is assumed to instantaneously feed into radiated power, such that [73]

$$\frac{\partial e_{\text{rad}}}{\partial t} = -\left(\frac{De_{\text{pot}}}{Dt}\right)_c = -\{\nabla\cdot\mathbf{u}\}^- \frac{\rho}{\rho_l-\rho_v}\left(p_d-p_v\right). \tag{3.41}$$

Due to its collapse energy focusing ability, Eqn. (3.39) is also referred to as the energy focusing approach, whereas Eqn. (3.41) is referred to as the non-focusing approach.

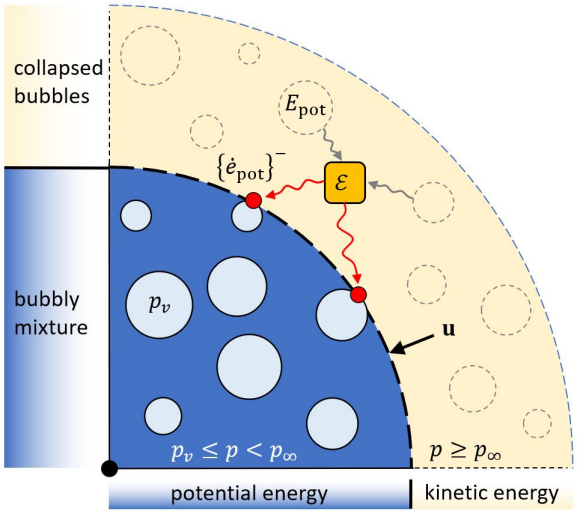

Figure 3.2: Illustration of the energy cascade governing the focusing of potential energy; the collapse induced change of potential energy is represented by $\{\dot{e}_{\text{pot}}\}^- = \left(De_{\text{pot}}/Dt\right)_c$.

3.2.3. SURFACE PROJECTION OF THE RADIATED ENERGY

The surface impact power caused by a cavity collapse is computed by projecting the energy flux radiated from the collapse source onto the impacted surface. The projection is instantaneous, which means that an infinite propagation speed of the radiated shock wave is assumed. This assumption is justified by the fact that the liquid sound speed is typically orders of magnitudes larger than the advective velocities of the cavitating flow. Let the power per unit volume radiated at some location $\mathbf{x}_P$ and some time instant t be $(\partial e_{\text{rad}}/\partial t)_{t,\mathbf{x}_P}$, then the impact power per unit surface caused by the isolated point source is given by

$$\left(\frac{de_S}{dt}\right)_{t,\mathbf{x}_P\rightarrow\mathbf{x}_S} = \left(\frac{\partial e_{\text{rad}}}{\partial t}\right)_{t,\mathbf{x}_P} G_{\mathbf{x}_P\rightarrow\mathbf{x}_S,\mathbf{n}}, \tag{3.42}$$

where the projection operator $G_{\mathbf{x}_P \to \mathbf{x}_S, \mathbf{n}}$ to achieve the projection of a monopole source at $\mathbf{x}_P$ on a surface location at $\mathbf{x}_S$ with corresponding surface normal vector $\mathbf{n}$ (see Fig. 3.3) is given by

$$G_{\mathbf{x}_P \to \mathbf{x}_S, \mathbf{n}} = \frac{1}{4\pi} \frac{(\mathbf{x}_P - \mathbf{x}_S) \cdot \mathbf{n}}{\| \mathbf{x}_P - \mathbf{x}_S \|^3}. \tag{3.43}$$

The instantaneous impact power per unit surface at some surface location $\mathbf{x}_S$ resulting from the distribution of all emission sources in the domain is then given by

$$\left(\frac{de_S}{dt} \right)_{t, \mathbf{x}_S} = \int_{\text{vol}} \left(\frac{\partial e_{\text{rad}}}{\partial t} \right)_{t, \mathbf{x}_P} G_{\mathbf{x}_P \to \mathbf{x}_S, \mathbf{n}} dV, \tag{3.44}$$

Eqns. (3.44) and (3.43) are a fully continuous form of the solid angle projection approach by Leclercq *et al.* [27]. Here, fully continuous, means that they represent the impact power per unit surface at a point location, whereas Leclercq *et al.* [27] employ the solid angle Ω (see Fig. 3.3) to project the radiated power on triangular surface elements of finite size. Nevertheless, both formulations represent an energy conserving conversion of radiated energy into local surface impact power. In spherical coordinates (r, θ, φ), we have $(\mathbf{x}_P - \mathbf{x}_S) \cdot \mathbf{n} = r \sin\theta$, where $r = \| \mathbf{x}_P - \mathbf{x}_S \|$. Surface integration of the projection operator, given by Eqn. (3.43), then gives

$$\int_{\text{surf}} G_{\mathbf{x}_P \to \mathbf{x}_S, \mathbf{n}} dS = \frac{1}{4\pi} \int_{\Delta\varphi} \int_{\Delta\theta} \sin\theta \, d\theta \, d\varphi = \frac{\Omega}{4\pi}, \tag{3.45}$$

where Ω is the solid angle as used in the work by Leclercq *et al.* [27]. With the surface integrated impact power caused by a single point radiation source given by

$$\left(\frac{dE_S}{dt} \right)_{t, \mathbf{x}_P \to S} = \int_{\text{surf}} \left(\frac{de_S}{dt} \right)_{t, \mathbf{x}_P \to \mathbf{x}_S} dS, \tag{3.46}$$

Eqn. (3.46) can be rewritten in terms of the solid angle as follows:

$$\left(\frac{dE_S}{dt} \right)_{t, \mathbf{x}_P \to S} = \frac{\Omega}{4\pi} \left(\frac{\partial e_{\text{rad}}}{\partial t} \right)_{t, \mathbf{x}_P} \tag{3.47}$$

The solid angle notation allows for straightforward analytical predictions of the surface integrated power caused by a single radiation source for any surface for which the corresponding solid angle is known. For a closed convex surface, for instance, we have $\Delta\theta = \pi$, $\Delta\varphi = 2\pi$, and hence $\Omega = 4\pi$. From Eqn. (3.47) then follows that all the power released from the point source is impacting the surface. For a point source impacting a flat surface stretched to infinity, the overall surface integrated impact rate can be expressed in polar coordinates (r_s, φ) as depicted in Fig. 3.4. Let the source be located at an arbitrary height h_s above the surface such that $(\mathbf{x}_P - \mathbf{x}_S) \cdot \mathbf{n} = h_s$ and $\| \mathbf{x}_P - \mathbf{x}_S \|^2 = r_s^2 + h_s^2$, then the solid angle becomes

$$\Omega = \int_0^{\infty}\int_0^{2\pi} \frac{h_s}{\left(r_s^2 + h_s^2\right)^{\frac{3}{2}}} r_s d\varphi dr_s$$
$$= 2\pi h_s \int_0^{\infty} \frac{r}{\left(r_s^2 + h_s^2\right)^{\frac{3}{2}}} dr_s = 2\pi. \tag{3.48}$$

Since Eqn. (3.48) holds for any arbitrary point source impacting the flat infinite surface, it follows from Eqns. (3.47) and (3.48) that the surface integrated impact power as the result of an arbitrary distribution of radiation sources becomes [77]

$$\left(\frac{dE_S}{dt}\right)_{\text{flat surf}} = \frac{1}{2}\frac{dE_{\text{rad}}}{dt}, \quad \text{where} \quad \left(\frac{dE_{\text{rad}}}{dt}\right)_t = \int_{\text{vol}} \left(\frac{\partial e_{\text{rad}}}{\partial t}\right)_{t,\mathbf{x}_P} dV. \tag{3.49}$$

The intuitive result of Eqn. (3.49) is that half of the emitted potential cavity energy is eventually distributed on the flat surface, irrespective of the cavity shape, its orientation, and initial distance from the impacted surface. However, the latter three aspects may have strong influence on how the same total amount of energy is distributed and focused on the surface, both in space and time.

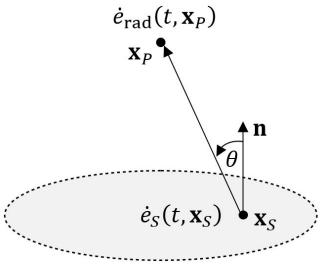

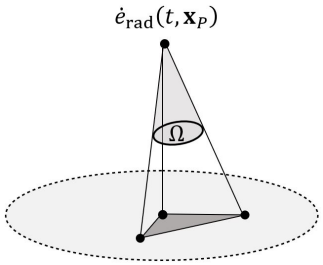

Figure 3.3: Coordinate definitions for the conversion of the power per unit volume radiated at location $\mathbf{x}_P$ into local impact power per unit surface at the surface location $\mathbf{x}_S$ (left) and illustration of the solid angle projection of radiated power on triangular surface elements as proposed by Leclercq *et al.* [27] (right).

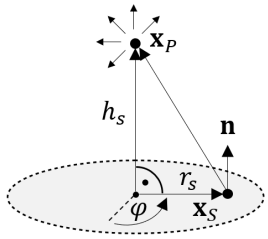

Figure 3.4: Point source impacting a flat surface stretching to infinity.

As Eqn. (3.44) represents the impact power per unit surface associated with a pressure wave, it can be rewritten in terms of the acoustic power density $d\mathscr{P}/dS$. The acoustic power $\mathscr{P}$ is equal to the radiated power $\partial e_{\text{rad}}/\partial t$ in Eqn. (3.11), and the acoustic power density is the acoustic power per unit surface area projected on the propagating wave front, such that

$$\frac{de_S}{dt} = \frac{d\mathscr{P}}{dS} = \frac{\partial e_{\text{rad}}/\partial t}{4\pi r^2}\cos\theta = \frac{p_a^2}{\rho_l c_l}\cos\theta. \tag{3.50}$$

In Eqn. (3.50), ρ_l and c_l are the liquid density and sound speed, respectively, and p_a is the acoustic pressure perturbation. The term $\cos\theta$ reflects the orientation of the reference surface dS relative to the propagation direction of the encountered sound

wave. Since $\mathscr{P}$ is the radiated power, it must be conserved across any spherical surface around the isolated source. The acoustic power density $d\mathscr{P}/dS$ can then be interpreted as the acoustic energy flux through an arbitrary point on that surface, and it can further be associated with the impact power per unit surface when the surface is thought to be the solid surface [78, 79]. In Eqn. (3.44), $\cos\theta$ is substituted with the relation $\cos\theta = (\mathbf{x}_P - \mathbf{x}_S)\cdot\mathbf{n}/\|\mathbf{x}_P - \mathbf{x}_S\|$. Thus, combining Eqns. (3.44) and (3.50) with the relation for $\cos\theta$ allows to reconstruct the acoustic pressure perturbation:

$$p_a(t,\mathbf{x}_S) = \frac{1}{2}\sqrt{\frac{\rho_l c_l}{\pi}\int_{\mathrm{vol}} \frac{(\partial e_{\mathrm{rad}}/\partial t)_{t,\mathbf{x}_P}}{\|\mathbf{x}_P - \mathbf{x}_S\|^2}\,dV} \tag{3.51}$$

Analogous to Eqn. (3.44) and in accordance with the solid angle projection approach by Leclercq *et al.* [27], the wave propagation time from the source location $\mathbf{x}_P$ to the impact location $\mathbf{x}_S$ is assumed to be zero. However, the liquid sound speed c_l in Eqn. (3.51) is considered to be finite.

3.3. NUMERICAL IMPLEMENTATION

3.3.1. DISCRETIZATION

The solution of the additional transport equation describing the spatial focusing of potential cavity energy, is explicitly forwarded in time. This means that all terms on the right-hand side of Eqn. (3.40) are assumed to be known from the previous time step t, such that $\mathscr{E}(t+\delta t)$ is obtained by forward substitution. The updated solution is then given by a first order Taylor series expansion: $\mathscr{E}(t+\delta t) = \mathscr{E}(t) + (\partial\mathscr{E}/\partial t)_t\,\delta t + \mathscr{O}\left(\delta t^2\right)$. The time increment δt, by which the solution is expanded, is equal to the time step size Δt. To achieve exact energy conservation for the splitting of the energy field into the kinetic energy flux ($\beta = 0$) and the radiation energy flux ($\beta = 1$), $\mathscr{E}$ and the radiated power $\partial e_{\mathrm{rad}}/\partial t$ are forwarded in such a way that the blending factors $\beta = 1$ and β are applied at the same time level $t+\Delta t$. With $\left(De_{\mathrm{pot}}/Dt\right)_c$, $\mathfrak{P}_{\mathbf{u}}(\nabla\mathscr{E})$, k, and β being specified by Eqns. (3.29), (3.33), (3.36), and (3.38), respectively, this gives

$$\mathscr{E}^*(t+\Delta t) = \left[-\Delta t\,(k+1)\left(\frac{De_{\mathrm{pot}}}{Dt}\right)_c + \mathscr{E}\left(1-\mathfrak{P}_{\mathbf{u}}(\nabla\mathscr{E})\right)\right]_t, \tag{3.52}$$

$$\left(\frac{\partial e_{\mathrm{rad}}}{\partial t}\right)_{t+\Delta t} = \beta(t)\,\frac{\mathscr{E}^*(t+\Delta t)}{\Delta t}, \tag{3.53}$$

$$\mathscr{E}(t+\Delta t) = \left(1-\beta(t)\right)\mathscr{E}^*(t+\Delta t). \tag{3.54}$$

Also, the updated solution for $\mathscr{E}$ is bound by 0, because $(k \geq 0) \wedge \left(\left(De_{\mathrm{pot}}/Dt\right)_c \leq 0\right) \wedge (0 \leq \mathfrak{P}_{\mathbf{u}}(\nabla\mathscr{E}) \leq 1)$, which means that no negative collapse induced kinetic energy can be produced by the numerical time integration. The evaluation of the terms $\{\phi(\mathscr{E})\}^-$ and $\{\phi(\mathscr{E})\}^+$ given by Eqns. (3.34) and (3.36), respectively, requires some special treatment, because they are only to be evaluated at locations where the corresponding denominator is different from zero. To avoid a point-wise check of the denominator value, a small number δ is added to the denominator of Eqn. (3.34) and subtracted from the denominator of Eqn. (3.36) to prevent a division by zero. The value of δ is chosen to be

10^{-15}, such that it does not affect the accuracy of the final result. All quantities that are needed to evaluate the transport equation of collapse induced kinetic energy and the radiated power are evaluated at the cell centers, except for the negative velocity divergence $\{\nabla\cdot\mathbf{u}\}^-$, which is needed to compute the material derivative $D\gamma/Dt$ and finally the acoustic power radiation given by Eqn. (3.29). The latter term is reconstructed from the face fluxes such that $(\nabla\cdot\mathbf{u})_C\,V_C=\sum_f \mathbf{u}_f\cdot\mathbf{S}_f$ for each cell. The subscripts C and f refer to the cell center and face center location, respectively; V_C is the cell volume, and $\mathbf{S}_f$ the face area times the outward directed face normal vector $\mathbf{n}$, given at the face center. The volume integration over all sources contributing to one surface impact location (see Eqn. (3.44)) is done by multiplying the locally radiated energy per unit volume by the corresponding cell volume V_c and by summation over all contributing cells. Similar to the reconstruction of the cell-centered velocity divergence, the cell centered gradient of $\mathscr{E}$ in Eqn. (3.33) is computed from the finite volume representation $(\nabla\mathscr{E})_C\,V_C=\sum_f \mathscr{E}_f\mathbf{S}_f$. It is further noted that the emitting grid cell of volume V_c can be thought of as a sphere of equivalent volume, which gives an equivalent radius $r_{\text{eq}}=[3V_c/(4\pi)]^{1/3}$. The radiated power is then given by a corresponding flux across the sphere surface. It is argued that r_{eq} is the smallest distance that is locally resolved by the computational grid. Therefore, near wall grid cells are treated such that the distance $\|\mathbf{x}_P-\mathbf{x}_S\|$ from the impact location in Eqns. (3.43) and (3.44) is substituted by the equivalent sphere radius when $\|\mathbf{x}_P-\mathbf{x}_S\|<r_{\text{eq}}$.

3.3.2. COMPUTATIONAL EFFICIENCY

The computational efficiency of the acoustic model is a key factor when it comes to its applicability in engineering practice. Fig. 3.5 illustrates that the computational efficiency of the model can be problematic indeed. It depicts a schematic of a computational domain with $N_{\text{cells}}=N_x\times N_y\times N_z$ cells. The solid bottom surface, where the acoustic model is evaluated as a run-time post-processing function, is discretized into $N_{\text{s.faces}}=N_x\times N_y$ surface faces.

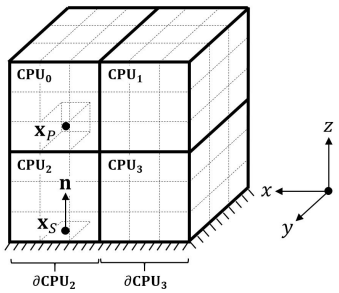

Figure 3.5: The sketch depicts 4 parallel CPUs, each including 27 grid cells, such that $N_{\text{cells}}=108$. The solid boundary is shared by CPUs 2 and 3. Hence, $N_{\text{s.faces}}=18$. In this context, $\mathbf{x}_P$ denotes the cell center location in the inner domain and $\mathbf{x}_S$ the face center location on the boundary with $\mathbf{n}$ being the corresponding surface normal vector. According to Eqn. (3.55), a volume integration (over $\mathbf{x}_P$) is needed to compute the impact at $\mathbf{x}_S$, which also involves parallel CPU communication. As this has to be done for each $\mathbf{x}_S$, the number of evaluations of Eqn. (3.55) is up to $N_{\text{cells}}\times N_{\text{s.faces}}=1944$.

One would expect that the model evaluation time relative to the flow simulation

time remains constant for different grid densities when the number of floating point operations needed for the model evaluation is proportional to the number of grid cells N_{cells}. In case that each grid cell acts as a radiation source, however, the number of floating point operations to evaluate Eqn. (3.44) is proportional to $\left(N_x \times N_y\right)^2 \times N_z = N_{\text{cells}} \times N_{\text{s.faces}}$. Hence, the model evaluation time relative to the flow simulation time is proportional to the number of surface faces, which makes the model increasingly expensive as the number of grid cells increases. The communication between parallel CPUs that is needed to project each acoustic source on each surface face, further increases the relative model evaluation time per time step. If, however, one is not primarily interested in the temporal evolution of $\dot{e}_S$, but rather in the distribution of the accumulated energy e_S, one finds from Eqn. (3.44) that

$$\begin{aligned} e_S\left(t^*, \mathbf{x}_S\right) &= \int_0^{t^*} \left(\frac{de_S}{dt}\right)_{t,\mathbf{x}_S} dt \\ &= \int_0^{t^*} \int_{\text{vol}} G_{\mathbf{x}_P \to \mathbf{x}_S, \mathbf{n}} \left(\frac{\partial e_{\text{rad}}}{\partial t}\right)_{t,\mathbf{x}_P} dV dt \\ &= \int_{\text{vol}} G_{\mathbf{x}_P \to \mathbf{x}_S, \mathbf{n}} \int_0^{t^*} \left(\frac{\partial e_{\text{rad}}}{\partial t}\right)_{t,\mathbf{x}_P} dt dV, \end{aligned} \tag{3.55}$$

because the surface projection operator $G_{\mathbf{x}_P \to \mathbf{x}_S, \mathbf{n}}$ is not time dependent. This means that the volume integration needs to be carried out only once at the end of the simulation and that it can be applied as a separate post-processing step. As a result, the model evaluation time becomes proportional with N_{cells}. Since the solution for $\partial e_{\text{rad}}/\partial t$ is obtained from explicit time integration, as given by Eqns. (3.52), (3.53), and (3.54), the relative evaluation time of the acoustic model becomes practically negligible.

Another practical problem is concerned with the computation of the moving average of p as defined by Eqn. (3.24), which assumed to be a measure of the collapse driving pressure p_d. The exact computation of the moving average requires to store the corresponding time window of the p-signal in a buffer $\left[p\left(t - n\Delta t, \mathbf{x}\right), ..., p\left(t, \mathbf{x}\right)\right]$, where $n\Delta t = T_{\text{mov}}$. This buffer must be updated at each time step. As this needs to be done for every cell of the computational grid, the amount of data to be stored in the buffer can easily exceed the random-access memory (RAM) limit when the number of time steps n in the buffer is large. For this reason, the method by Welford [80] is employed to approximate the moving average for window size T_{mov} [68] by

$$\langle p \rangle_t \approx \langle p \rangle_{t-\Delta t} + \frac{\Delta t}{T_{\text{mov}}} \left(p\left(t\right) - \langle p \rangle_{t-\Delta t}\right). \tag{3.56}$$

3.4. STATISTICAL ANALYSIS OF IMPLOSION IMPACT PATTERNS

The aggressiveness of the cavitating flow is assessed from the distribution of the energy e_S accumulated on a sample surface per sample time T, also referred to as the time-averaged impact power e_S/T. In cyclic cavitating flows, the accumulated surface energy distribution is the result of repetitive impact events. However, the frequency and amplitude, at which different surface locations of the sample surface are impacted, can

differ significantly. As a result, one and the same amount of accumulated energy can result either from repetitive small-amplitude impacts, or from one single extreme event. Whether the sample surface is mostly vulnerable to repetitive events, or whether isolated extreme events play a major role in the cavitation erosion process, may depend on the material properties of the sample surface. For this reason, it is useful to have a statistical analysis method available that can isolate surface areas on which the accumulated surface energy level has been achieved by isolated extreme events rather than repetitive low amplitude impacts. The idea is to construct a filter that attenuates low amplitude events such that only the energy levels resulting from high amplitude events remain visible in the time averaged impact power distribution. In Sec. 3.4.1, it is explained how the low amplitude events are attenuated, and in Sec. 3.4.2, the filter function applicable to the surface energy distribution is derived. For better readability, the compact notation $\dot{e}_S$ is used for the local impact power caused by all radiation sources as given by Eqn. (3.44), $\dot{e}_S|_{\mathbf{x}_P}$ is used for the local impact power caused by an isolated point source at $\mathbf{x}_P$ given by Eqn. (3.42), $\dot{e}_{\text{rad}}$ for the radiated power given by Eqn. (3.39), and the surface projection operator given by Eqn. (3.43) is written in the short form G.

3.4.1. POWER MEAN ANALYSIS

The statistical identification of extreme events is based on the idea to amplify the surface impact power by an intensity exponent n. This is achieved by the power or Hölder mean [81] of the impact power per unit surface, given by

$$M_{\{n\}}(\dot{e}_S) = \left(\frac{1}{T} \int_T (\dot{e}_S)^n \, dt \right)^{\frac{1}{n}}. \tag{3.57}$$

The power mean given by Eqn. (3.57) approaches the amplitude of the input signal $\dot{e}_S$ as the intensity exponent n increases. The discrete form of Eqn. (3.57) is given by

$$M_{\{n\}}(\dot{e}_S) = \left[\frac{1}{T} \sum_{i=1}^{I} \left(\dot{e}_{S,i} \right)^n \Delta t_i \right]^{\frac{1}{n}}, \quad \text{where } \sum_{i=1}^{I} \Delta t_i = T. \tag{3.58}$$

In the discrete form, the time step size Δt is interpreted as a weight of the amplified impact power. Eqn. (3.58) evolves into the non-weighted form when the simulation time step size is constant. Substituting Eqn. (3.44) into Eqn. (3.58) gives

$$M_{\{n\}}(\dot{e}_S) = \left[\frac{1}{T} \sum_{i=1}^{I} \left(\sum_{j=1}^{J} G_j \dot{e}_{\text{rad},ij} V_{P,j} \right)^n \Delta t_i \right]^{\frac{1}{n}}. \tag{3.59}$$

The practical problem with Eqn. (3.59) is that the inner sum is non-linear with respect to the outer sum due to the intensity exponent n applied to the inner sum. This means that the inner and the outer sums cannot be interchanged to make the evaluation of Eqn. (3.59) computationally more efficient, analogous to the computation of the accumulated surface energy given by Eqn. (3.55). To this end, Eqn. (3.57) is modified in such a way that the intensity exponent n is applied to the surface impact $\dot{e}_S|_{\mathbf{x_p}}$ caused by the individual source terms, which gives

$$M_{\{n\}}\left(\dot{e}_S|_{\mathbf{x}_P}\right) = \left(\frac{1}{T\ \mathrm{vol}}\int_T\int_{\mathrm{vol}}\left(\dot{e}_S|_{\mathbf{x_P}}\right)^n dV\,dt\right)^{\frac{1}{n}}, \tag{3.60}$$

With the surface impact power caused by an isolated point source, as given by Eqn. (3.42), we now get $\left(\dot{e}_S|_{\mathbf{x_P}}\right)^n = G^n\,(\dot{e}_{\mathrm{rad}})^n$, and hence

$$M_{\{n\}}\left(\dot{e}_S|_{\mathbf{x}_P}\right) = \left[\frac{1}{T\ \mathrm{vol}}\int_{\mathrm{vol}} G^n \int_T (\dot{e}_{\mathrm{rad}})^n\,dt\,dV\right]^{\frac{1}{n}}, \tag{3.61}$$

which is the computationally more efficient equivalent of Eqn. (3.60) as the volume integration needs to be carried out only once at the end of the time integration. In discrete form, Eqn. (3.61) becomes

$$M_{\{n\}}\left(\dot{e}_S|_{\mathbf{x}_P}\right) = \left[\frac{1}{T\ \mathrm{vol}}\sum_{j=1}^{J} G_j^n V_{P,j}\sum_{i=1}^{I}\left(\dot{e}_{\mathrm{rad},ij}\right)^n \Delta t_i\right]^{\frac{1}{n}}, \quad \text{where } \sum_{i=1}^{I}\Delta t_i = T, \quad \sum_{j=1}^{J} V_{P,j} = \mathrm{vol}, \tag{3.62}$$

and where vol is the total volume. Eqn. (3.62) is a two-dimensional weighted power mean of the impact power caused by the individual radiation sources, where now both the time step size Δt and the grid cell volume V_P act as weights. Again, Eqn. (3.62) becomes non-weighted with respect to Δt when the simulation time step size is constant. An entirely non-weighted form is only obtained when also the grid cell volume V_P is constant within the integration volume. For the sake of computationally efficiency, the power mean $M_{\{n\}}\left(\dot{e}_S|_{\mathbf{x}_P}\right)$, given by Eqn. (3.61), is preferred over the power mean $M_{\{n\}}\left(\dot{e}_S\right)$, given by Eqn. (3.57), and used in the further course of this work.

3.4.2. ENSEMBLE AVERAGES

Based on the technique introduced in Sec. 3.4.1, a filter is constructed that attenuates the contributions of low amplitude events to the time averaged surface impact power distribution. Attenuation means that the filter is constructed in such a way that the filtered time averaged impact power distribution, denoted by $\langle\dot{e}_S\rangle_{\{n\}}$, satisfies $\langle\dot{e}_S\rangle_{\{n\}} \le e_S/T$ at any point on the target surface. It is further noted that the unfiltered time averaged impact power e_S/T is obtained for $n = 1$.

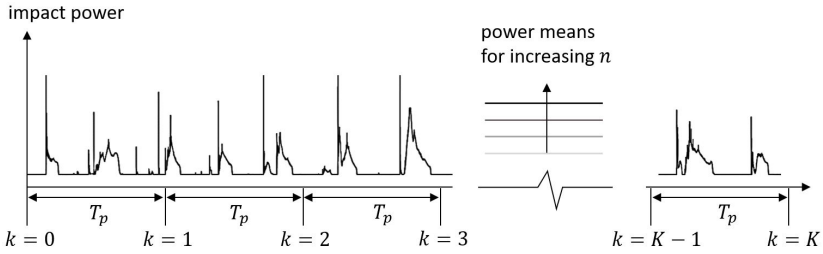

Figure 3.6: Subdivision of the local impact power signal of length T into equidistant intervals of length T_p, where $T = KT_p$; with increasing intensity exponent n, the averaged impact power obtained from the filtering method approaches the (maximum) amplitude of the input signal.

The power mean $M_{\{n\}}\left(\dot{e}_S|_{\mathbf{x}_P}\right)$, given by Eqn. (3.61), involves the integration over a certain sample time T. The sample time T can be divided into sub-intervals T_p, at the end of which the amplified radiation sources $(\dot{e}_{\text{rad}})^n$ are projected on the target surface. Due to the non-linearity introduced for $n \neq 1$, the filtered average may be affected by the choice of the frequency $1/T_p$, at which the amplified radiation sources are projected. For this reason, the projection frequency $1/T_p$ is introduced as an additional parameter in the analysis method. As illustrated in Fig. 3.6, the impact signal is decomposed into equidistant intervals of length T_p, where k indicates the projection time interval, and K is the total number of projection intervals within the length KT_p of the entire signal. The filter is then applied individually to each of the intervals. The power mean given by Eqn. (3.60) is now applied to each of the k time intervals individually, such that

$$M_{\{n\}k}\left(\dot{e}_S|_{\mathbf{x}_P}\right) = \left(\frac{1}{T_p\ \text{vol}}\int_{(k-1)\,T_p}^{kT_p}\int_{\text{vol}}\left(\dot{e}_S|_{\mathbf{x_P}}\right)^n dV\,dt\right)^{\frac{1}{n}}. \tag{3.63}$$

The power mean given by Eqn. (3.63) is applied to the entire impacted surface, and a filter $F_{\{n\}k}$ is constructed by normalizing the $M_{\{n\}k}$ distribution by its maximum value:

$$F_{\{n\}k} = \frac{M_{\{n\}k}\left(\dot{e}_S|_{\mathbf{x}_P}\right)}{\max\left[M_{\{n\}k}\left(\dot{e}_S|_{\mathbf{x}_P}\right)\right]_{\text{surf}}}, \quad \text{where } F_{\{n\}k} \in [0,\ 1] \tag{3.64}$$

The filtered surface energy distribution accumulated during the period T_p of time interval k is then obtained by multiplying the unfiltered surface energy distribution $e_{S,k}$ accumulated in interval k with the filter function, such that

$$\langle e_{S,k}\rangle_{\{n\}} = e_{S,k}F_{\{n\}k}, \quad \text{where } e_{S,k} = \int_{(k-1)\,T_p}^{kT_p}\dot{e}_S\,dt. \tag{3.65}$$

Following the same procedure as for the individual time intervals k, a filter of the entire ensemble comprising of K intervals is derived from the power mean of the individual filtered surface energy distributions, given by

$$M_{\{n\}}\left(\langle e_{S,k}\rangle_{\{n\}}\right) = \left(\frac{1}{K}\sum_{k=1}^{K}\left(\langle e_{S,k}\rangle_{\{n\}}\right)^n\right)^{\frac{1}{n}}. \tag{3.66}$$

Analogous to Eqn. (3.64), the ensemble filter is obtained by dividing the surface distribution, given by Eqn. (3.66), by its maximum value, such that

$$F_{\{n\}}\left(e_S\right) = \frac{M_{\{n\}}\left(\langle e_{S,k}\rangle_{\{n\}}\right)}{\max\left[M_{\{n\}}\left(\langle e_{S,k}\rangle_{\{n\}}\right)\right]_{\text{surf}}}, \quad \text{where } F_{\{n\}} \in [0,\ 1]\,. \tag{3.67}$$

The filtered surface energy distribution accumulated during the entire sample time of duration $KT_p = T$ is then obtained by multiplying the surface energy distribution e_S with the ensemble filter, given by Eqn. (3.67). Dividing by the sample time $KT_p = T$ gives the filtered averaged impact power

$$\langle \dot{e}_S\rangle_{\{n\}} = \frac{e_S}{KT_p}F_{\{n\}}\left(e_S\right), \quad \text{where } e_S\left(T = KT_p\right) = \int_0^T \dot{e}_S\,dt. \tag{3.68}$$

4

APPLICATION OF THE CAVITATION IMPLOSION LOAD MODEL

This chapter includes three numerical test cases to verify and validate the acoustic implosion load model presented in Chap. 3. The first test case in Sec. 4.1 was originally designed by Schmidt et al. *[17]. It involves the numerical simulation of a vapor bubble cloud collapsing close to a target surface. As the initial potential energy content of the cloud is known, based on at least the modeling assumptions, the acoustic model can be verified against analytical predictions for the surface integrated impact energy. Another aspect that makes this test case particularly interesting is the circumstance that the distribution of bubble sizes and locations results in a situation where a few bubbles tend to exhibit a rather isolated behavior, whereas the majority of bubbles collapse in a collective manner. Therefore, this numerical simulation is well suited to test in how far the acoustic model can reflect the cascade of energy in both situations. Finally, the acoustic pressure perturbation predicted by the acoustic model is compared to the cloud collapse pressure computed by Schmidt* et al. *[17], who used a fully compressible density-based approach.*

The second test case in Sec. 4.2 addresses the periodic cavitating flow around a NACA0015 hydrofoil. The main focus is on the model parameters that are involved in the computation of the accumulated surface energy distribution resulting from repetitive cavity collapses. These parameters concern the computation of the collapse driving pressure distribution, needed in the potential energy balance, and the isolation of extreme event contributions to surface energy distribution. As a result of Sec. 4.2, recommendations on the model parameter settings are derived. The obtained surface energy distribution is discussed against experimental paint test observations by van Rijsbergen et al. *[82] and a numerical erosion risk assessment method by Li* et al. *[29] for the same operating conditions. Furthermore, the effect of energy focusing during the cavity collapses is investigated by comparing results obtained from both the focusing and the non-focusing approach, as described in Sec. 3.2.2.*

Parts of this chapter were published in Physics of Fluids **31**, 052102 (2019) [1].

The third test case in Sec. 4.3 aims to reproduce experimental observations on the flow aggressiveness of a cavitating flow in an axisymmetric nozzle experiment by Franc et al. *[83]. Due to its particular design, the experimental set-up by Franc* et al. *[83] can indeed be seen as a prototype example of an aggressive and potentially erosive cavitating flow. Concerning the flow sensitivity study and the acoustic model parameter settings, the approach to the flow problem can be seen as an application of the best practice guidelines derived in Sec. 4.2. Most importantly, it is demonstrated, that both the average vapor content of the cyclic flow and the cavity shedding frequency converge in the limit of large mass transfer coefficients, and furthermore, that this also results in a converged distribution of the accumulated surface impact energy obtained from the acoustic model. This is a step towards quantitative erosion risk predictions. Qualitative comparisons against the erosion damage pattern obtained by Franc* et al. *[83], and results from other numerical studies in literature, are presented.*

4.1. COLLAPSING VAPOR BUBBLE CLOUD

The acoustic cavitation implosion load model derived in Chap. 3 is applied to a cloud of 125 vapor bubbles collapsing under a high ambient pressure of 40 bar. The numerical test case was earlier set up by Schmidt *et al.* [17], where they investigated the characteristic of a numerically computed pressure signal on a virtual pressure sensor located on a solid surface underneath the collapsing cloud. The results by Schmidt *et al.* [17], which they have kindly shared together with the bubble cloud specifications, are considered as a reliable reference data set, because it was obtained from a fully compressible density-based numerical approach, and because grid size independence of the results was demonstrated for a fixed acoustic Courant number[17]. To test the cavitation implosion load model against the collapse pressure signal obtained by Schmidt *et al.* [17], the reconstructed acoustic pressure given by Eqn. (3.51) is employed. Results obtained from both the energy focusing and the non-focusing approaches, as discussed in Sec. 3.2.2, are compared to each other.

4.1.1. COMPUTATIONAL GRID, INITAL AND BOUNDARY CONDITIONS

The bubble cloud consists of 125 non-intersecting, bubbles as depicted in Fig. 4.1. The positions and corresponding radii (0.70 mm to 1.65 mm) are the same as in the study by Schmidt *et al.* [17], who generated a set of bubbles that are randomly distributed both in space and in diameter in such a way that the population density increases towards the cloud center. This data set was kindly provided by TUM/AER (see Schmidt *et al.* [17]) in a private communication as part of the EU H2020 CaFE Project. The cloud is embedded in a cubic inner domain with a 20 mm edge length. The bottom surface of the inner domain depicted in Fig. 4.1 is highlighted in green, and the virtual pressure sensor located exactly in the center of the bottom surface is indicated in black color. The pressure sensor signal is obtained by averaging the reconstructed acoustic pressure p_a over the sensor surface. The entire computational domain is depicted in Fig. 4.2. With the bottom surface area and height being 4 m × 4 m and 2 m, respectively, it is considered to be sufficiently large so that it can be assumed that the far field boundaries are undisturbed. The computational mesh is block structured and consists of uniform cubic cells in the inner domain. The outer domain, connecting the inner domain with the far field boundaries, consists of hexahedral cells. The number of cell layers between the inner domain and the far field boundaries is 25, where the cell expansion ratio towards the far field boundaries is chosen such that a smooth cell size transition to the inner domain is achieved. In order to perform a grid sensitivity study, the inner domain is systematically refined in the x, y and z directions. Three different grid resolutions are investigated in this study. Following the sensitivity study by Schmidt *et al.* [17], the inner domains of grid 1, 2 and 3 contain 28^3, 55^3 and 110^3 cells, respectively. The grids and the corresponding bubble resolutions are depicted in Fig. 4.4 for the central plane cross section view indicated in the upper left sub-figure. The liquid fraction field is initialized such that cells entirely located within one of the bubbles are assigned a liquid fraction of $\gamma = 0$, and cells entirely located in the liquid phase are assigned a value of $\gamma = 1$. A sampling algorithm is applied to determine the liquid fraction of those cells that are cut by any bubble interface [2]. The density field is given by the linear mixture relation given by Eqn. (2.18), where the liquid and vapor densities are assumed to be $\rho_l = 1000\ \mathrm{kg/m^3}$ and

$\rho_v = 0.02$ kg/m^3, respectively. The initial pressure field is determined in exactly the same way, with the vapor pressure being $p_v = 2340$ Pa and the liquid pressure being equal to the far field pressure, i.e. $p_\infty = 40$ bar. This is not yet an appropriate initial condition for the liquid pressure field, which must satisfy the Laplace equation $\nabla \cdot \nabla p = 0$ in order to eliminate spurious acoustics [17]. With one minor modification, the segregated iterative approach described in Appx. A.1 allows to establish this condition during the first time step of the simulation. With the flow being initially at rest, the pressure equation given by Eqn. (A.11) evolves into a Laplace equation for p. Different from the original arrangement of the equations in the PISO (Pressure-Implicit with Splitting of Operators [84]) loop, as implemented in OpenFOAM [64, 85], the pressure equation must be solved before the transport equation of γ in order to avoid numerical instabilities that may occur in the equation for γ as a result of the pressure field initialization in the cut-cells. If the γ equation is solved first, instabilities can result from the sharp initial pressure jump between locations where $\gamma = 1$ and $\gamma = 0$ in combination with the linear interpolation in between, which results in exhaustive mass transfer magnitudes in the cut-cells, and thereby making the equation numerically unstable.

A single near-wall bubble is marked as B1 in Figs. 4.1 and 4.4, because its collapse is shown to cause a localized high impact load on the bottom wall, which is discussed in more detail below. The driving pressure p_d in Eqn. (3.29) is assumed to be constant in space and time and equal to the ambient pressure p_∞.

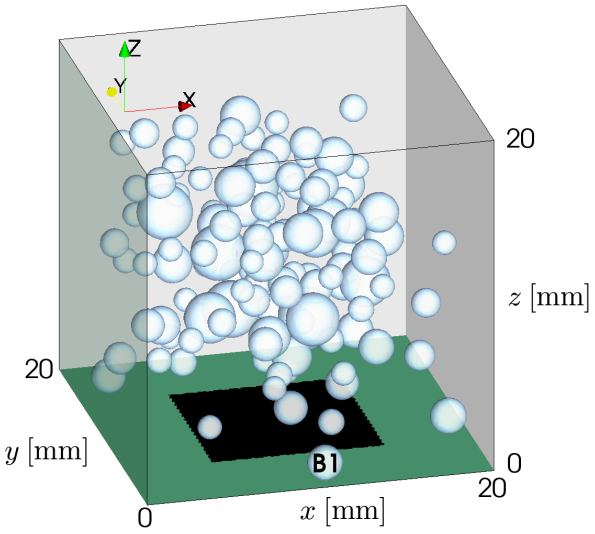

Figure 4.1: Bubble cluster and 1 cm × 1 cm numerical pressure sensor indicated in black color on the bottom surface.

Recall from Sec. 3.3.1 that the negative velocity divergence $\{\nabla \cdot \mathbf{u}\}^-$, needed to compute the material derivative $\{D\gamma/Dt\}^+$ and eventually the acoustic power radiation, is reconstructed from the face fluxes. It was shown [2] that this reconstruction involves numerical errors, which would eventually violate the overall energy balance. To correct

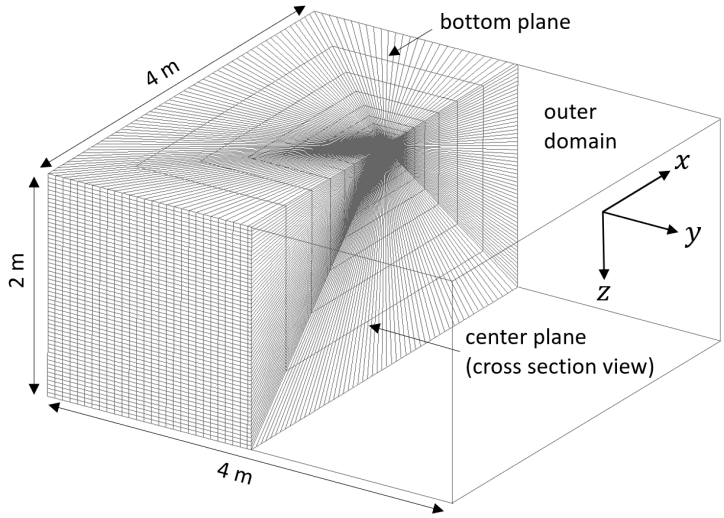

Figure 4.2: Computational domain with 4 m × 4 m bottom surface area and grid refinement towards the inner part of the domain.

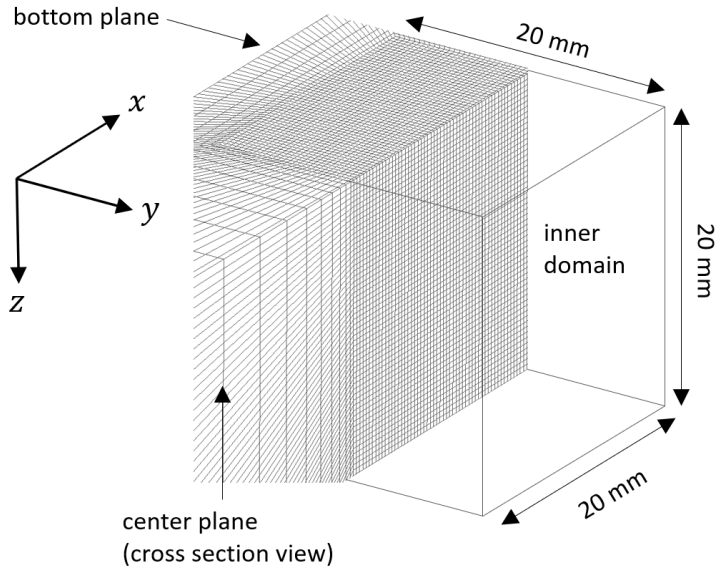

Figure 4.3: Cubic inner part (2 cm × 2 cm × 2 cm) of the computational domain depicted in Fig. 4.1; the inner domain contains the bubble cluster depicted in Fig. 4.1.

for this error in at least an integral sense, we calculate the condensation induced reduction of potential energy, given by Eqn. (3.29), based on a corrected negative velocity

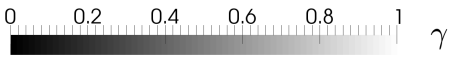

bubble cluster - side view

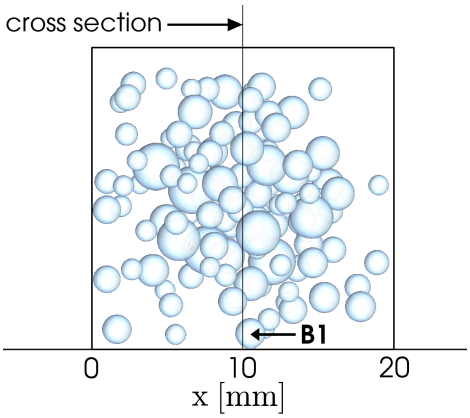

Grid 1: 28^3 cells in the inner domain

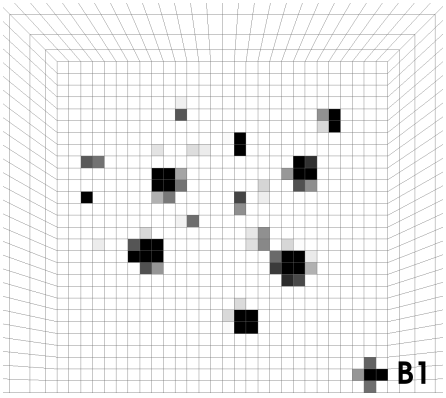

Grid 2: 55^3 cells in the inner domain

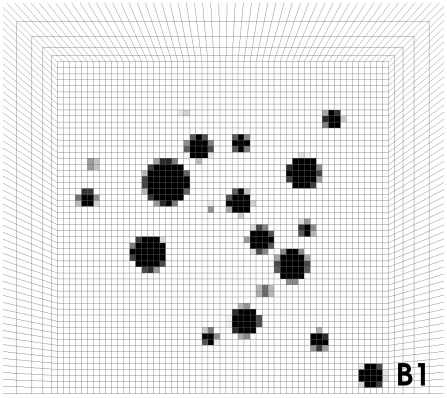

Grid 3: 110^3 cells in the inner domain

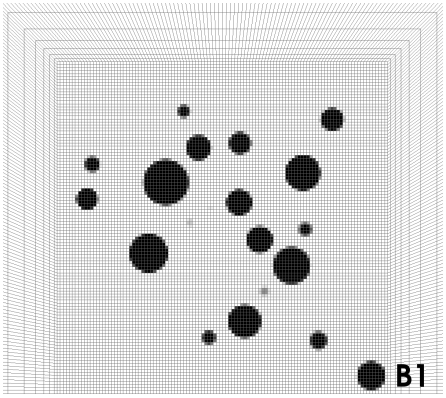

Figure 4.4: Cross section view (indicated in the top left) on the bubble cluster initialalized for different grid densities in the inner domain; the near-wall bubble B1 is also marked in Fig. 4.1.

divergence $\kappa(t)\{\nabla\cdot\mathbf{u}\}^-$, where $\kappa(t)$ is determined such that the balance [2]

$$\kappa(t)\sum_{i=1}^{N_{\text{cells}}}\left[\left(\frac{D\gamma}{Dt}\right)_{C,i}V_{C,i}\right]=\sum_{i=-1}^{N_{\text{cells}}}\left[\left(\frac{\partial\gamma}{\partial t}\right)_{C,i}V_{C,i}\right] \tag{4.1}$$

is satisfied. This correction is motivated by the circumstance that the volume integral of the partial time derivative of γ, represented by the right-hand side of Eqn. (4.1), correctly reflects the overall change of vapor volume because it directly results from solving the transport equation for γ, given by Eqn. (A.16). It is noted that $\partial\gamma/\partial t$ includes an advective component that does not contribute to the change of vapor volume. However,

the advective components cancel each other out in the volume integral. By this means, the numerical errors made during the reconstruction of $\{\nabla \cdot \mathbf{u}\}^-$ are eliminated from the integral balance, and the numerical conversion of radiated power into surface impact power can be checked against the analytical prediction, given by Eqn. (3.49). The correction factor $\kappa(t)$ must be re-computed at each time step, because the error that is made in the reconstruction of $\nabla \cdot \mathbf{u}$ changes when the magnitude of the cavitation model source term changes. It is important to note that this correction can be done in this particular case only. As there is only condensation involved during the cavity collapse, the volume change cannot be subject to the cancellation of competing condensation and evaporation processes at different locations in the domain, which again may be subject to different error magnitudes. For this reason, the velocity divergence correction cannot be applied to arbitrary flow situations involving both condensation and evaporation. It can only serve as a means to isolate the numerical error that stems from the reconstruction of $\{\nabla \cdot \mathbf{u}\}^-$ in a cavity collapse test case in order to verify that both the transport equation of collapse induced kinetic energy and the term to achieve the surface projection of radiated energy, as derived in Sec. 3.2, are correctly implemented.

4.1.2. SENSITIVITY STUDY

In order to obtain a physically converged result for the collapse characteristic of the bubble cloud, it is essential to investigate the sensitivity of the collapse time τ with respect to the mass transfer coefficients of the cavitation model and the temporal resolution. This is done for grid 2. Fig. 4.5 shows the evolution of the total vapor volume over time for a fixed time step size of $\Delta t = 10^{-8}$ s and for different magnitudes of the condensation constant C_c. For very small values of C_c, a significant delay of the collapse time is observed. In the limit $C_c \to 0$, no condensation can take place at all. For values of $C_c \geq 1$ kg·s/m^5, the curves collapse. However, this independence with respect to the model parameter can only be achieved when the time step Δt is sufficiently small. Fig. 4.6 shows the evolution of vapor volume over time for a systematic variation of Δt, where the condensation constant is kept constant at $C_c = 1000$ kg·s/m^5. Significant delays of the collapse time are observed for large time step sizes. As Δt approaches 10^{-8} s, the curves converge to a solution that is independent of the time step size. Fig. 4.7 further depicts the evolution of vapor volume over time for the three different grids in Fig. 4.4. It is found that the evolution of total vapor volume is practically insensitive of the grid resolution. This finding is in line with the results by Schmidt *et al.* [17], even though their results were obtained from a fundamentally different method based on a thermodynamic equation of state describing the mixture fluid, and a density-based numerical solution technique. The results are further supported by similar findings in related studies [66, 67, 69]. The collapse time of the bubble cloud is identified by a change of sign of $\dot{V}$ at the final collapse stage and found to be $\tau = 6.5 \cdot 10^{-5}$ s, which is in good agreement with the results by Schmidt *et al.* [17]. The insensitivity of τ with respect to the grid resolution is explained by the circumstance that the bubble population density of the cloud is so high that is does not allow for any significant pressure recovery between the bubbles. This is illustrated in Fig. 4.8, which is depicting cross sectional views of the pressure field at $t = 0.08\tau$. The above findings can be generalized in so far that the time step size must be chosen sufficiently small, while the mass transfer coefficients must be adequately large. In this limit, the

mass transfer model always has sufficient capacity to achieve phase transition within the time scale that is determined by the inertia driven flow, and the local phase transition event is adequately resolved in time so that no truncation errors occur. Based on this sensitivity study, the configuration of $C_c = 10$ kg·s/m^5, $\Delta t = 10^{-8}$ s and grid 2 is found to provide a converged solution that is independent of the mass transfer coefficients.

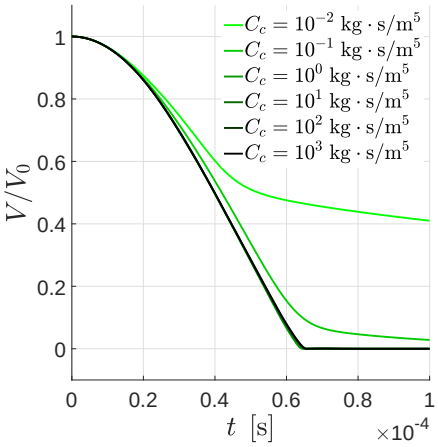

Figure 4.5: Evolution of the dimensionless vapor volume over time (V_0 is the initial vapor volume of the cloud) for grid 2 in Fig. 4.4, $\Delta t = 10^{-8}$ and a systematic variation of the condensation mass transfer constant C_c in Eqn. (A.16).

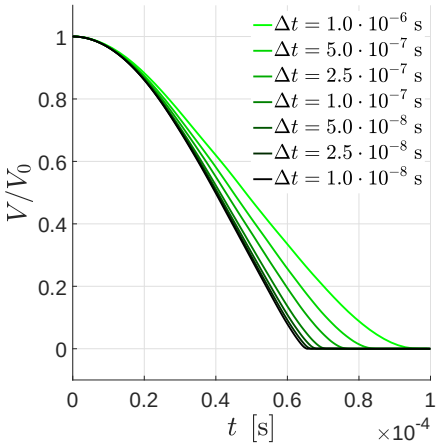

Figure 4.6: Evolution of the dimensionless vapor volume over time (V_0 is the initial vapor volume of the cloud) for grid 2 in Fig. 4.4, $C_c = 1000$ kg·s/m^5 and a systematic variation of the time step size Δt.

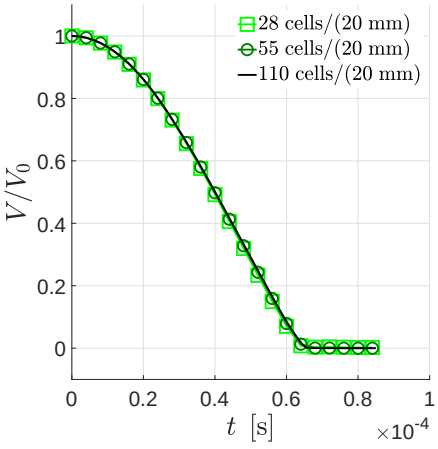

Figure 4.7: Evolution of the dimensionless vapor volume over time (V_0 is the initial vapor volume of the cloud) for $\Delta t = 10^{-8}$, $C_c = 1000$ kg·s/m^5 and for the three different grids depicted in Fig. 4.4.

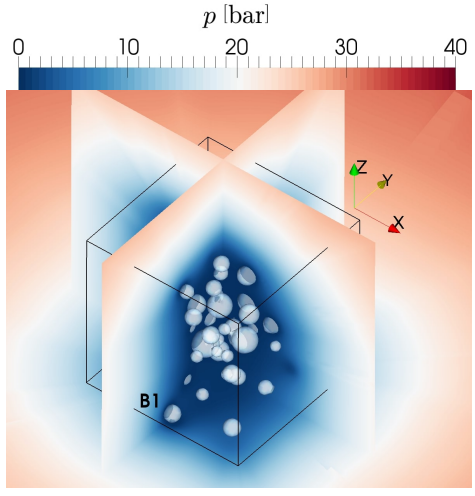

Figure 4.8: $\gamma = 0.5$ iso-surfaces of the vapor bubbles at time instant $t = 0.08\tau$ and cross sectional views on the corresponding pressure field for grid 2 in Fig. 4.4, $C_c = 1000$ kg·s/m^5 and $\Delta t = 10^{-8}$.

4.1.3. THE EFFECT OF ENERGY FOCUSING ON THE ACOUSTIC POWER AND ACOUSTIC PRESSURE SIGNATURE

Fig. 4.9 depicts the evolution of the dimensionless accumulated surface energy $E_S/E_{\text{pot},0}$, obtained from integration of the surface impact power over time and over the entire 4 m × 4 m bottom surface area. The red dashed line represents the result obtained from the non-focusing approach, where the condensation induced change of potential energy is instantaneously converted into radiated acoustic power (see Eqn. (3.41)). The black solid line is obtained from the energy focusing approach introduced in Secs. 3.2.1 and 3.2.2. If no potential energy focusing is applied, then the amount of E_S relative to $0.5E_{\text{pot},0}$ corresponds exactly to the percentage of dimensionless volume V/V_0 by which the cavity has shrunk. When the transport equation of collapse induced kinetic energy (see Eqn. (3.37)) is applied, the initial potential energy is focused towards the collapse center in the form of collapse induced kinetic energy, thereby delaying the main impact towards the final stage of the collapse. In both cases, however, the amount of accumulated surface energy converges to the analytically predicted value of 50% initial potential energy (see Eqn. (3.49)) with reasonable accuracy. With the energy focusing approach, a major amount of energy is focused towards the final collapse stage and then released in a rather sudden step.

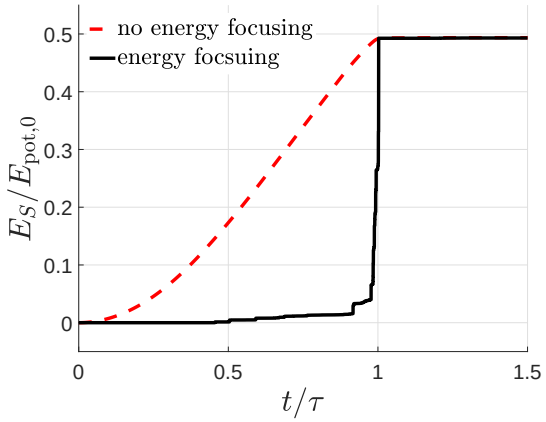

Figure 4.9: Evolution of the dimensionless energy accumulated on the entire bottom surface for the focusing and the non-focusing approach.

In view of the acoustic pressure analysis, it is noted that the total pressure computed by Schmidt *et al.* [17], depicted by the red solid line in Fig. 4.11, is not entirely comparable with the acoustic pressure p_a. The most obvious difference is that the total pressure must be equal to the far field pressure p_∞ once the pressure perturbations caused by the cloud collapse have decayed, whereas the acoustic pressure is a pressure perturbation itself which tends to zero after the collapse event. At the beginning of the collapse, the total wall pressure in close vicinity to the vapor bubble cloud is significantly lower than the far field pressure. This is explained by the fact that the small distance of the vapor bubble cloud to the solid wall hardly allows the liquid pressure to recover on the bottom wall.

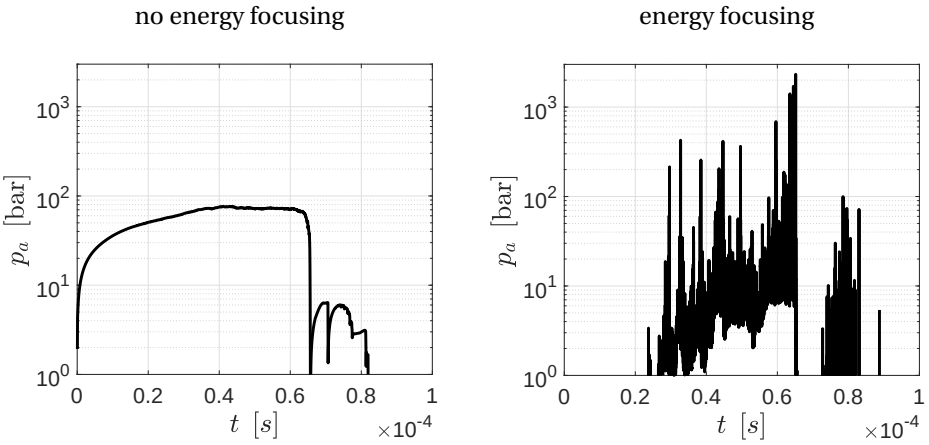

Figure 4.10: Evoution of the acoustic pressure signal averaged over the numerical pressure sensor surface depicted in Fig. 4.1 for the focusing (right) and the non-focusing (left) approach.

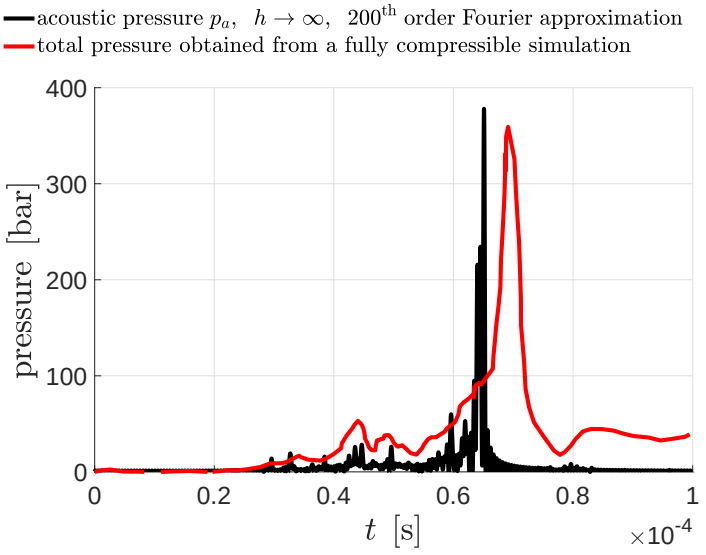

Figure 4.11: Comparison of the acoustic pressure signal obtained from the energy focusing approach with the total pressure signal computed by Schmidt *et al.* [17]; the focusing parameter h is defined in [1], where $h \to \infty$ represents the energy focusing method as described in Sec. 3.2.

However, the collapse peak pressure computed by Schmidt *et al.* [17], is supposed to be governed by the energy transported by the shock wave through the nearly incompressible liquid phase, and it should therefore exhibit a similar characteristic as the acoustic peak pressure reconstructed from the acoustic model.

Fig. 4.10 shows the acoustic pressure signals obtained from averaging the acoustic

pressure p_a over the virtual pressure sensor depicted in Fig. 4.1 for the focusing (right) and the non-focusing (left) approach. Compared to the results by Schmidt *et al.* [17], a strong smearing of the signal is observed for the non-focusing approach. The pronounced peak at the end of the collapse that is observed in the results by Schmidt *et al.* [17], is not at all present in the acoustic pressure signal obtained from the non-focusing approach. This clearly demonstrates the inability of the non-focusing approach to reflect the instantaneous energy balance, as discussed in Sec. 3.1.1. The energy focusing approach on the other hand results in a pronounced peak of the acoustic pressure perturbation due to the delay of power radiation towards the final collapse stage. However, various spurious high amplitude peaks are observed before the final collapse stage. They are identified as spurious peaks, because of the fact that most of the energy is impacting the surface at the end of the collapse event (see Fig. 4.9), which implies that there is no significant energy content in the peaks before the final collapse stage. This is further supported by Fig. 4.11, which shows a Fourier reconstruction of the p_a-signal obtained from the energy focusing approach (see Fig. 4.10, right). The Fourier reconstruction involves the first 200 modes, such that modes higher than that are filtered out. It can be seen that the spurious peaks before the final collapse stage are not present in the reconstructed acoustic pressure signal. In accordance with the distribution of accumulated surface energy versus time in Fig. 4.9, this indicates that the spurious acoustic pressure peaks before the final collapse stage contain very little energy. This behavior is further explained by Eqn. (3.12), which suggests that despite the large amplitude of the spurious acoustic pressure peaks, their impact energy contribution is small because of their very short impact duration. When significantly more than 200 modes are included in the Fourier reconstruction of the acoustic pressure signal, the spurious peaks before the final collapse stage start to become noticeable. Fig. 4.11 further depicts for reference the total pressure signal computed by Schmidt *et al.* [17]. It is observed that the total pressure peak value occurs somewhat later than the acoustic pressure peak. This delay is due to the time that it takes for the pressure wave to propagate from the cloud collapse center to the bottom wall in the compressible simulation by Schmidt *et al.* [17], whereas the wave propagation speed of the associated wave in the acoustic model is assumed to be infinite. A rough estimation of the wave propagation time can be made by assuming a propagation speed of $c_l = 1500$ m/s and by assuming that the cloud collapse center is in the middle of the inner domain, which gives an approximate propagation time of $6.7 \cdot 10^{-6}$ s. Also, the impact duration of the acoustic pressure peak is found to be significantly smaller than the impact duration of the total pressure peak by Schmidt *et al.* [17]. As discussed in Sec. 3.2.2, this difference is attributed to the tendency of the energy focusing approach to convert the accumulated collapse induced kinetic energy into radiated acoustic energy in a sudden step at the final collapse stage.

A measure of the impact aggressiveness is given by the distribution of surface energy accumulated on the bottom surface throughout the cloud collapse. Fig. 4.12 depicts the accumulated surface energy distribution on the bottom wall underneath the cloud, normalized by the cloud collapse time $\tau = 6.5 \cdot 10^{-5}$ s. The left figure shows the distribution obtained from the non-focusing approach and the right figure the distribution obtained from focusing approach described in Secs. 3.2.1 and 3.2.2. In both cases, one distinct isolated footprint is observed, which is caused by the isolated close wall bubble

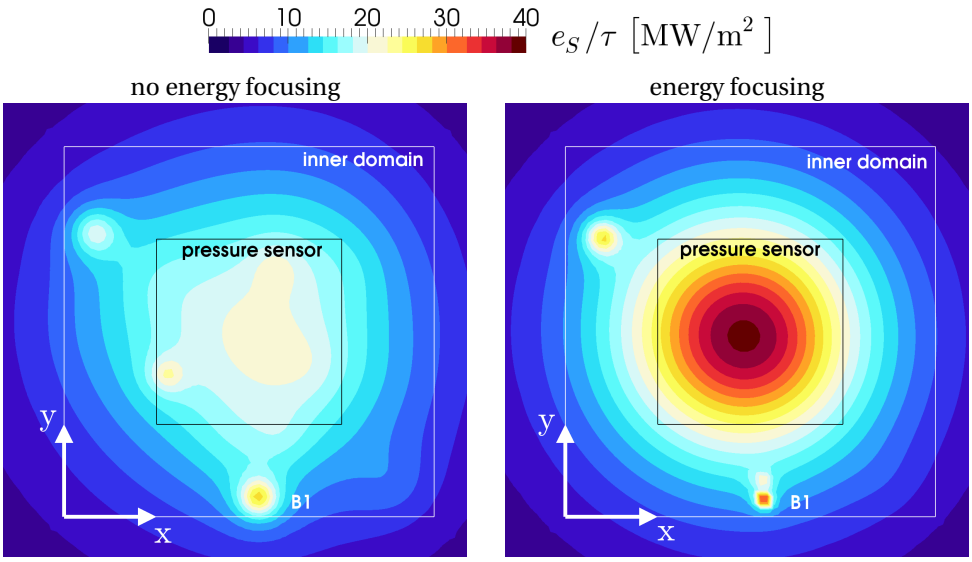

Figure 4.12: Distribution of the accumulated surface energy normalized by the cloud collapse time $\tau = 6.5{\cdot}10^{-5}$ s for the non-focusing approach (left) and the focusing approach (right); the accumulated surface energy is obtained from time integration of the surface impact power per unit surface.

marked as B1 in Fig. 4.1. The energy focusing approach predicts only one more isolated footprint, which is located outside the virtual pressure sensor surface and which was caused by a bubble initially located in the outer periphery of the cloud. The original approach predicts another isolated footprint located on the virtual pressure sensor surface and generally tends to leave a more asymmetric impact pattern. With the major part of the initial potential cloud energy being focused towards the collapse center, the focusing approach leaves a rather axisymmetric footprint on the virtual pressure sensor as would be observed if the impact was caused by an isolated point source. The surface energy distribution obtained from the energy focusing approach is also of larger magnitude as compared to the original approach. Another effect of the collective focusing of potential energy is that the peak value of the accumulated surface energy distribution is caused by the collective collapse event, whereas the original approach predicts the peak value in the vicinity of the isolated collapse of bubble B1.

The collective cloud collapse behavior observed in the present study is in agreement with the findings by Schmidt *et al.* [17], who showed that, in this particular case, the bubble cloud can be replaced by a homogeneous structure of equivalent volume fraction without changing the collapse characteristics. As shown by Wang and Brennen [16], it strongly depends on the density of the bubble population whether a bubble cloud exhibits this collective behavior. In sparsely populated clouds, the bubbles tend to behave as individual bubbles [16]. Based on their early numerical computations on collapsing vapor bubble clouds, Wang and Brennen [16] suggest that the focusing of potential energy across the individual bubbles into the inner peripheries of a densely populated cloud is governed by an inward directed bubbly shock or condensation shock wave. The

bubbly shock in bubbly mixtures of high vapor fraction can be thought to exhibit the same wave propagation behavior as a condensation shock in a homogeneous water-vapor mixture of equivalent vapor fraction [86]. This mechanism is supported by the model of the kinetic energy transport term $\phi(\mathscr{E})$, which allows for a redistribution of energy between coherently collapsing cavities, together with Eqn. (3.38), which suppresses the energy radiation until the pressure in the liquid phase has exceeded the driving pressure. Thus, the potential cavity energy is accumulated and transported on the low pressure side of the bubbly shock front. This also means that the capability of the energy focusing approach to reflect the potential energy focusing driven by the inward directed condensation shock strongly depends on the capability of the flow solver to resolve this flow phenomenon. It was shown that even semi-empirical mass transfer approaches involving adjustable model coefficients can resolve condensation shock states [66, 77], when the prerequisites discussed in Sec. 4.1.2 are met. Indeed, the formation of an inward directed bubbly shock, as described by Wang and Brennen [16] is shown in Fig. 4.13, which depicts a cross sectional view of the distribution of the total pressure (left) and the velocity magnitude (right) for different time instants. It can be seen how a discontinuity in both the pressure and the velocity field forms across the outer periphery of the cloud at $t = 0.83\tau$, which becomes more pronounced as $t = \tau$ is approached.

The focusing of collapse induced kinetic energy is further illustrated by Fig. 4.14, which depicts the distribution of accumulated kinetic energy $\mathscr{E}$ obtained from Eqn. (3.22). It can be seen how the collapse induced kinetic energy accumulation starts in the outer cloud periphery, and how it focuses and intensifies towards the cloud collapse center as the collapse time τ is approached. A significant portion of the initial potential cloud energy is thereby focused into the cloud collapse center. One isolated region of pronounced kinetic energy accumulation prior to the final collapse stage is observed at the collapse location of bubble B1 in Fig. 4.1, which is also in agreement with the results by Schmidt *et al.* [17].

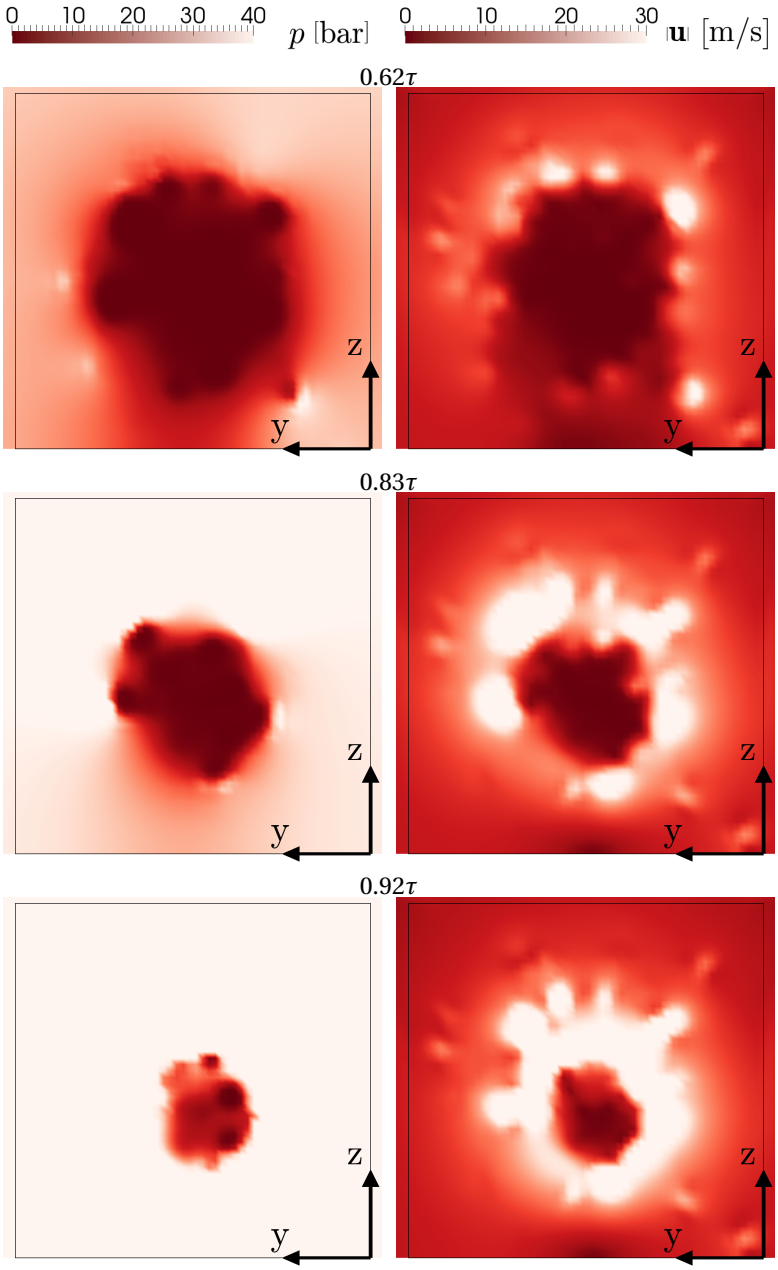

Figure 4.13: Cross section view (as indicated in Fig. 4.4) on the distribution of the total pressure (left) and the velocity magnitude (right) for different time instants relative to the cloud collapse time $\tau = 6.5 \cdot 10^{-5}$; the black outline represents the cubic inner domain (2 cm × 2 cm × 2 cm).

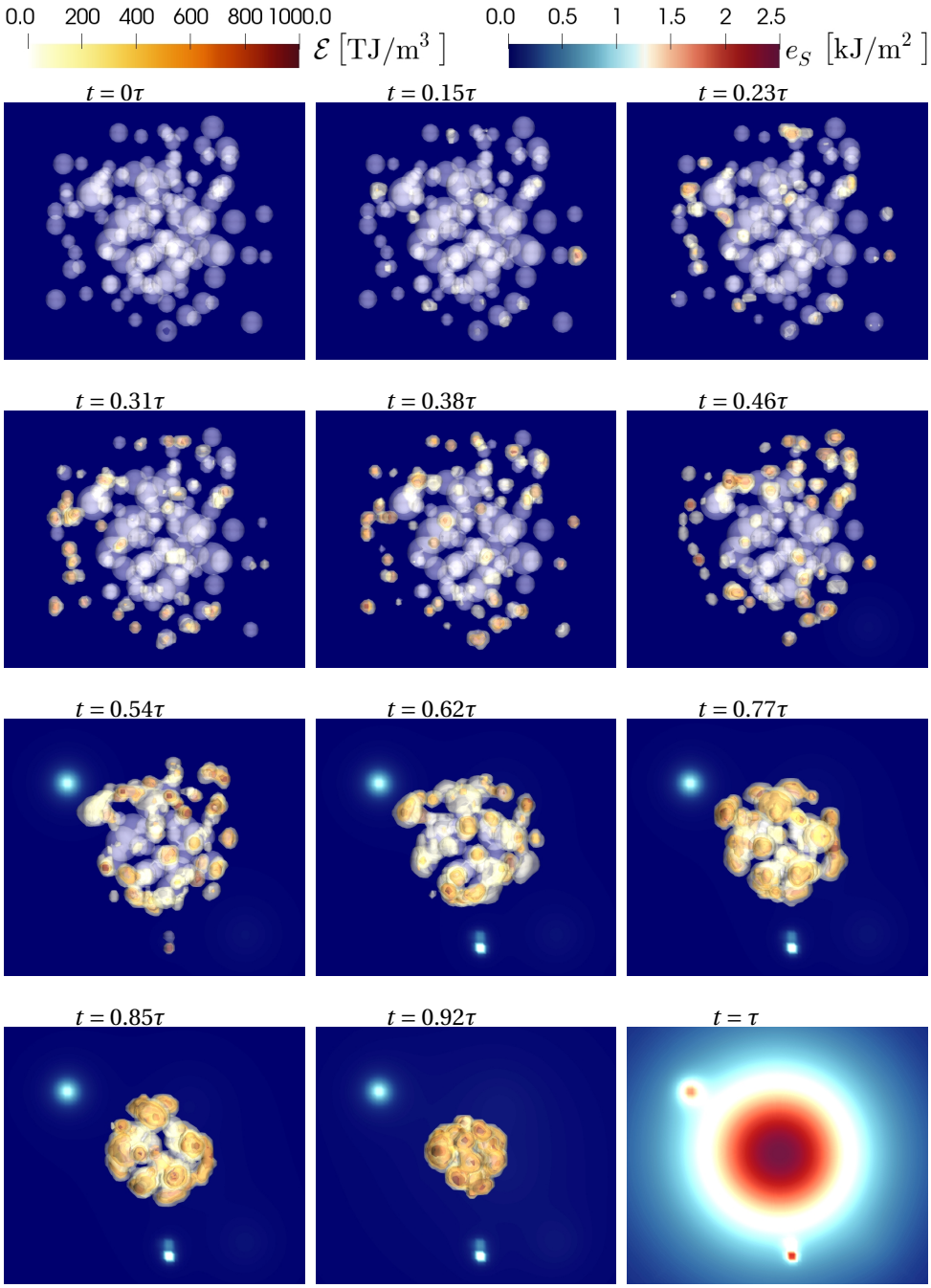

Figure 4.14: Top view on the collapsing vapor bubble cloud and iso-surfaces of the accumulated collapse induced kinetic energy per unit volume $\mathscr{E}$ (see Eqn. (3.28)) absorbed in the bubble interfaces at different time instants of the bubble cloud collapse; the bubble interfaces are indicated by $\gamma = 0.5$ iso-surfaces of the liquid fraction.

4.1.4. REMAINING UNCERTAINTIES IN THE ENERGY BALANCE

Despite the fact that the impact load characteristics are well captured by the method presented in this study, some uncertainties remain. One uncertainty concerns the driving pressure p_d in Eqn. (3.29), which is assumed to be constant and equal to the ambient pressure p_∞ for the entire cloud surface. However, due to the effects of wall interaction and the interaction of rather isolated bubbles with the close by bubble cloud, the driving pressure distribution is in fact neither constant in space nor constant in time and the assumption that $p_d(t,\mathbf{x}_P) = p_\infty$ can only be an approximation of the actual condition experienced by the collapsing cloud. The problem of not exactly knowing the effective driving pressure p_d in the potential energy balance was discussed in detail in previous work [2]. It is also noted that, as discussed in Sec. 3.2.2, one cannot expect an entirely time accurate representation of the acoustic impact signal. Nevertheless, the present modeling approach captures the delay of the collapse impact towards the final collapse stage due to the temporal and spatial focusing of the implosion energy, and therefore reflects the bubble cloud dynamics more accurately than the original non-focusing approach. However, the exact events at the final collapse stage are beyond the model resolution. As a result, the model theoretically allows to radiate the shock wave energy within an infinitely thin wave front. It is also mentioned that the transmitted shock wave energy computed in the present study is associated with the idealized situation of zero non-condensable gas content. The relation between gas content and shock wave energy derived by Tinguely *et al.* [14], Patella *et al.* [34], and Brennen [87] might be employed in future work to complement the model by the effect of non-condensable gas. Finally, the reconstruction of the velocity divergence needed for the computation of the local acoustic power source terms, is subjected to numerical errors, which is why the correction given by Eqn. (4.1) was applied. By means of this correction, the volume integrated energy balance could be satisfied in the present study. However, as already discussed in previous work [2], this correction cannot be applied to any arbitrary flow situation. Therefore, a best possible reconstruction of the velocity divergence field is a key factor for the reliability of the method presented in this study.

4.2. NACA0015 HYDROFOIL

The hydrofoil test case is based on an experiment by van Rijsbergen *et al.* [82], where a NACA0015 hydrofoil is mounted in a cavitation tunnel section under 8° angle of attack. Despite the steady state inflow condition, the involved sheet cavitation dynamics lead to a periodic cavitating flow. Next to acoustic measurements and high-speed video observations of the cavitating flow, van Rijsbergen *et al.* [82] have also conducted paint tests in order to identify erosive zones on the suction side of the hydrofoil surface. The erosion damage patterns obtained by van Rijsbergen *et al.* [82] allow for a qualitative comparison against potentially erosive zones identified by the cavitation implosion load model. The extent of potentially erosive zones, as indicated by the surface impact energy distribution obtained from the simulation for a periodic cavitating flow, depends on the non-uniform and unsteady driving pressure distribution, which is approximated by the moving time averaged pressure distribution as discussed in Sec. 3.1.3. A sensitivity study on the moving time window length is carried out 4.2.4. Extreme collapse events are identified with the statistical analysis method introduced in Sec. 3.4. The statistical method

involves the definition of another time window, for which a sensitivity study is carried out as well in Sec. 4.2.5. Based on the sensitivity studies, recommendations are derived for the length of both time windows.

4.2.1. NUMERICAL SET-UP

Fig. 4.15 shows the dimensions of the computational set-up. The dimensions of the tunnel cross section, the foil and its position and angle of attack are in line with the experimental set-up by van Rijsbergen *et al.* [82] and a corresponding numerical set-up by Li *et al.* [29]. The tunnel width is $w_t = 0.04$ m and equal to the foil span, and the tunnel height is $h_t = 2w_t$, with the cord center of the foil located at $h_t/2$. The tunnel length is $l_t = 0.57$ m. Cord length and span of the foil are 0.06 m and 0.04 m, respectively. The study is carried out for a downstream ambient pressure of $p_\infty = 302.3$ kPa, a uniform horizontal inflow speed of 17.3 m/s and an angle of attack of 8°. The fixed value velocity boundary condition is specified at the inlet and the fixed value pressure boundary condition at the outlet as indicated in Fig. 4.15. In order to get rid of pressure fluctuations at the outlet boundary, where a fixed value pressure boundary condition is applied, the flow is diffused in a diffuser section, starting at 6.5 cord lengths downstream from the foil's leading edge (x =0.39 m in Fig. 4.15). Since the flow is inviscid, mass continuity and Bernoulli's equation can be used to determine the outlet pressure such that the aimed tunnel tunnel pressure p_∞ is obtained under wetted flow conditions and, on average over time, under cavitating flow conditions [88]. The liquid volume fraction γ is constrained by a zero gradient boundary condition at all boundaries except for the inflow boundary, where a fixed value of $\gamma = 1$ is applied. The unstructured mesh as depicted in Fig. 4.16 includes four refinement levels. The cell length is scaled by 2^{-n}, with $n = 0$ for the base mesh, and $n = 4$ on the finest level. A variation of grid density is achieved by changing the number of cells in the base mesh. For all refinement levels and all grids, the characteristic cell dimensions are $\Delta x = \Delta y = 0.5\Delta z$. By this means, geometrically similar grids are obtained, and a uniformly spaced grid is achieved in the region where the flow is expected to cavitate. The characteristic longitudinal cell lengths Δx on the finest level for the four different grid configurations investigated in this study are listed at the bottom of Table 4.1. The grid depicted in Fig. 4.16 corresponds to grid 1 from Table 4.1. The time step size Δt is systematically decreased until a converged solution is obtained.

Since the dynamics of the larger scale cavitation structures are of primary interest in this study, the frequency of large pressure pulses, associated with the cyclic collapse of larger scale structures, and hence the shedding frequency, is employed as a measure for the convergence of the unsteady flow solution. The collapse frequency is obtained from a frequency analysis procedure that is further described in Sec. 4.2.2. Following the study by Li *et al.* [29], the vapor pressure is $p_v = 1854$ Pa, and the densities of the vapor and the liquid phases are $\rho_v = 0.014$ kg/m^3 and $\rho_l = 998.85$ kg/m^3, respectively. This corresponds to a downstream cavitation number of $\sigma = 2.01$. From previous studies [88], the values $C_c = 5000$ kg·s/m^5 and $C_v = C_c/2$ for the mass transfer coefficients (see Eqn. (2.19)) were found to be large enough to obtain a cavity shedding frequency that is independent of the model parameter value. Gravitational forces are taken into account, although they are presumably negligible. The operating conditions are summarized in Tab. 4.1.

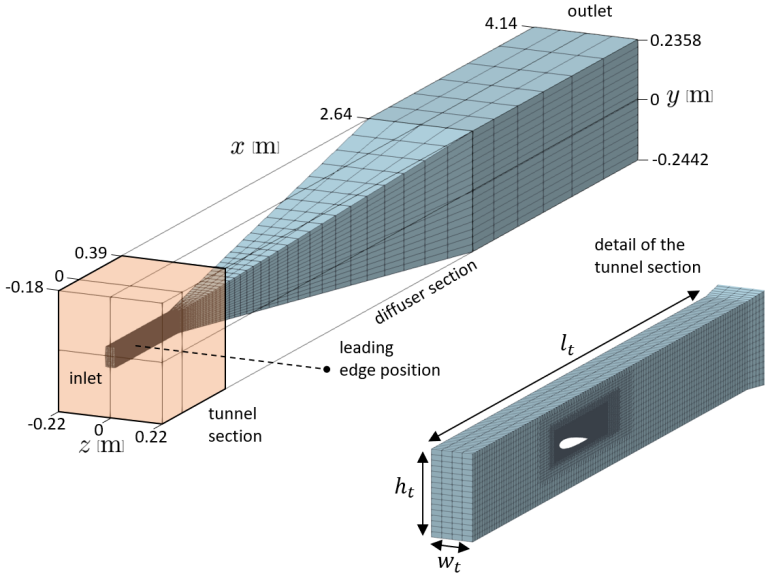

Figure 4.15: Computational domain including the tunnel section and a downstream diffuser section; the origin of the coordinate system is located at the leading edge of the foil.

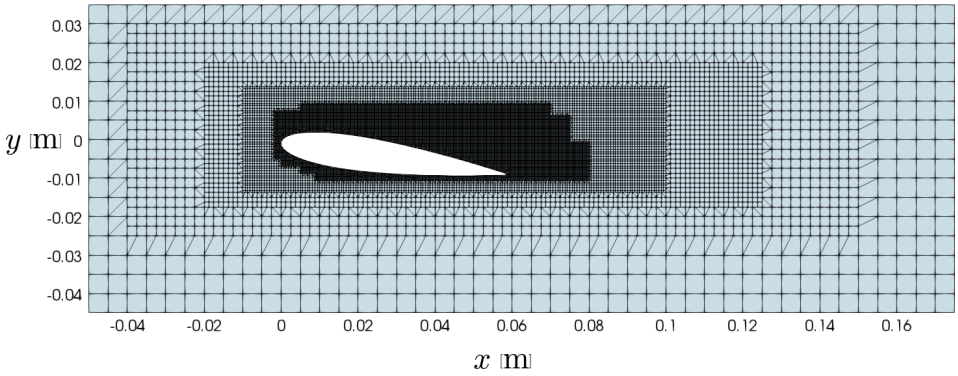

Figure 4.16: Refinement levels around the NACA0015 hydrofoil for grid 1 from Table 4.1; the origin of the coordinate system is located at the leading edge of the foil.

Table 4.1: Geometrical specifications, operating conditions and grid densities for the NACA0015 hydrofoil

Geometry specifications	
Profile: NACA0015	Angle of attack: $\alpha = 8°$
Tunnel length: $l_t = 0.57$ m	Cord: $c_{\text{foil}} = 0.06$ m
Tunnel width: $w_t = 0.04$ m	Foil span: $s = 0.04$ m
Tunnel height: $h_t = 0.08$ m	Cord center pos.: $0.5h_t$
Leading edge position: $6.5c_{\text{foil}}$ from diffuser	
Fluid properties	
Liquid density: $\rho_l = 998.85$ kg/m^3	
Vapor density: $\rho_v = 0.014$ kg/m^3	
Vapor pressure: $p_v = 1854$ Pa	
Ambient tunnel pressure: $p_\infty = 302.995$ kPa	
Boundary conditions	
Uniform inflow speed: $u_x = 17.3$ m/s	
Diffuser outlet pressure: $p_{\text{out}} = 451.759$ kPa	
Solid walls: free slip condition ($\mathbf{u} \cdot \mathbf{n} = 0$)	
Grid densities	
$\Delta x = \Delta y = 0.5\Delta z$ on the finest level in Fig. 4.16:	
Grid 0: $\Delta x = 0.15625$ mm (1794140 cells)	
Grid 1: $\Delta x = 0.31250$ mm (919944 cells)	
Grid 2: $\Delta x = 0.62500$ mm (393096 cells)	
Grid 3: $\Delta x = 1.25000$ mm (114694 cells)	

4.2.2. FREQUENCY ANALYSIS

The dominant frequency, i.e. the cavity shedding frequency of the flow, is identified from the power spectral density (PSD) estimates of several local (virtual) pressure probes. The PSD is estimated by the square of the discrete Fourier transform (DTF) obtained using a fast Fourier transform (FFT) algorithm of the input signal $p(t)$. A number of n_{probes} pressure probes is sampled at different locations in the computational domain at which the dominant frequency can be expected to be noticeable. An average PSD distribution is determined from the individual PSD distributions, such that $\overline{\text{PSD}} = 1/n_{\text{probes}} \sum_{i=1}^{n_{\text{probes}}} \text{PSD}_i$. A low pass filter is applied to the input signal $p(t)$ to attenuate frequencies that are significantly higher than the expected dominant frequency. The low pass filtered signal is obtained from the Welford [80] approximation of the moving time average of $p(t)$, as given by Eqn. (3.56), where $1/T_{\text{mov}}$ is the cut-off frequency from which on the signal is increasingly attenuated. Furthermore, the $p(t)$ signal of length T_s is split into half overlapping equidistant windows of length T_h, such that the total number of overlapping windows is $n_h = 2T_s/T_h - 1$. Each of these windows is multiplied by the Hanning function $h(t) = \sin^2(\pi t/T_h)$ to avoid effects of discontinuities at the periodic Fourier domains.

4.2.3. SENSITIVITY STUDY ON THE CAVITY SHEDDING FREQUENCY

Fig. 4.18 depicts the density-pressure trajectory at observation P_0 in Fig. 4.17, located on the foil surface at half span and 20% cord length. The trajectory stays close to vapor pressure during phase transition and only evolves into high amplitude pressure peaks at the final stage of the condensation process. This confirms that the mass transfer coefficients are large enough to enforce a scale separation between the phase transition and the driving pressure range, as discussed in Sec. 2.1.3. In this regime, the characteristic frequency of the inertia driven flow can be expected to be insensitive with respect to the mass transfer coefficients. With the fluid properties and ambient conditions in Table 4.1 and an associated mixture sound speed of $c_m = 2.0$ m/s (see Sec. 2.1.3), the inverse Mach number given by Eqn. (2.14) becomes $\text{Ma}^{-1} = 0.12$. Since $\text{Ma}^{-1} << 1$, the scale separation enforced by the large mass transfer coefficients is physically justified due to the reasons discussed in Sec. 2.1.3.

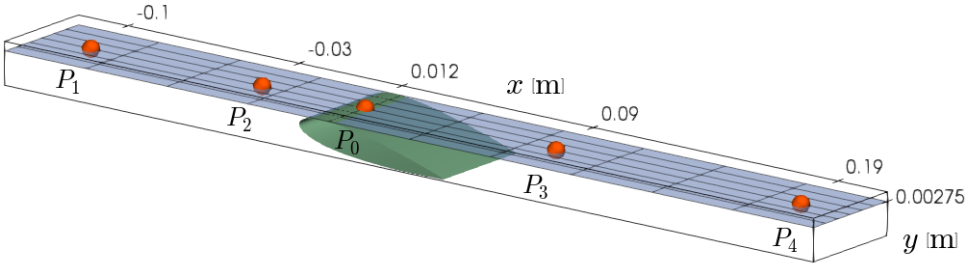

Figure 4.17: Centerline ($z = 0$) observation points at the indicated x-y coordinates for the (virtual) pressure and density probes.

The grid and time step sensitivity of the flow around the NACA0015 hydrofoil is as-

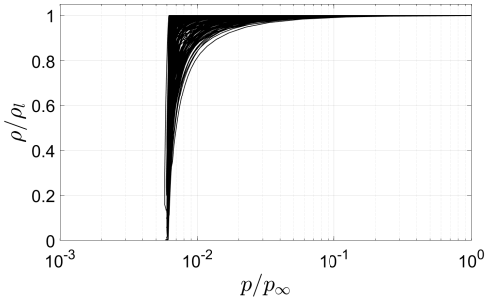

Figure 4.18: ρ-p trajectory on the foil surface at observation point P_0 in Fig 4.17 (half span and 20% cord length) for Δt =7.5 $\cdot 10^{-7}$ s and grid 1 from Table 4.1.

sessed from the pressure fluctuations at the observation points P_1, P_2, P_3 and P_4 in Fig. 4.17. The frequency analysis described in Sec. 4.2.2 is applied to obtain the averaged power spectral density $\overline{\text{PSD}}$, with the number of probes being n_{probes}=4. For each probe, the sample time is T_s = 0.18 s, and the length of the half overlapping Hanning windows is $T_h = T_s/3$, such that the total number of Hanning windows is n_h = 5. The moving average frequency/cut-off frequency of the low pass filter is $1/T_{\text{mov}}$ = 2000 Hz.

Fig. 4.19 depicts the $\overline{\text{PSD}}$ distributions for different grid densities, where Δt =7.5·10^{-7} s. As the magnitude of the distribution is not of interest for the frequency analysis, all distributions are normalized by the maximum peak value max($\overline{\text{PSD}}$) of all four distributions. It is observed that coarse grids tend to result in rather low frequencies of the first harmonic. The frequency of the first harmonic converges to a mesh independent value with increasing grid resolution. The same analysis is carried out for grid 1 from Table 4.1 and different time step sizes. For rather large time steps, the $\overline{\text{PSD}}$ distribution tends to get smeared out into the low frequency regime. The dominant frequencies are determined from a second order polynomial least square regression through the peak value of the $\overline{\text{PSD}}$ distribution, its two left-hand neighbors, and its two right-hand neighbors. The smallest time step size Δt =7.5 $\cdot 10^{-7}$ s in combination with grid 1 from Table 4.1 is considered to provide a physically converged solution for the further course of this study. The corresponding frequency of 192 Hz is in good agreement with the frequency of 188 Hz found by van Rijsbergen *et al.* [82] in the experiment. It is assumed that the solution of the unsteady cavitating flow field that is obtained in this manner provides a reasonable estimate of the flow conditions in the experiment by van Rijsbergen *et al.* [82], even though viscosity effects, such as the viscous pressure drop along the tunnel section or tunnel sidewall effects, are not present in the numerical simulation.

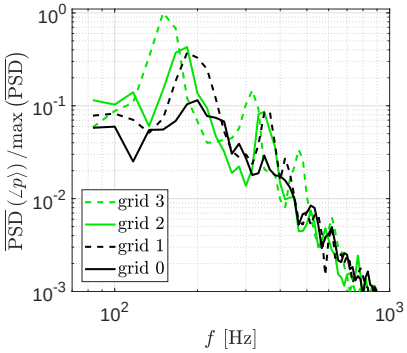

Figure 4.19: Power spectral density (PSD) of the moving time averaged pressure $\langle p \rangle$ against frequency, averaged over the observation points P_1, P_2, P_3 and P_4 in Fig. 4.17 for the different grid densities in Tabel 4.1 and fixed time step size $\Delta t = 7.5 \cdot 10^{-7}$ s.

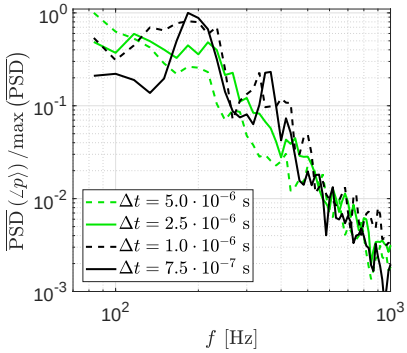

Figure 4.20: Power spectral density (PSD) of the moving time averaged pressure $\langle p \rangle$ against frequency, averaged over the observation points P_1, P_2, P_3 and P_4 in Fig. 4.17 for different time step sizes Δt and grid 1 in Tabel 4.1.

4.2.4. EFFECT OF THE MOVING AVERAGE WINDOW SIZE ON THE DRIVING PRESSURE AND SURFACE ENERGY DISTRIBUTION

The accumulated surface energy computed from Eqn. (3.55) is evaluated on the hydrofoil surface. It is investigated how the sliding window size T_{mov} affects the distribution of the driving pressure p_d given by Eqn. (3.24), which again has an effect on the surface energy distribution, because the driving pressure difference $p_d - p_v$ is needed to compute the change of potential energy given by Eqn. (3.29). For the longest sliding window, which comprises an entire simulation length, the exact moving average, as given by Eqn. (3.24), can be computed by successively integrating the entire pressure signal at each grid cell, and by dividing by the sample time at the end of the simulation. This was done in a separate simulation, and the driving pressure distribution obtained in this manner is used as a steady state field in Eqn. (3.29). For the smaller moving time windows, where the computation of the exact average requires to store the window data in a buffer that is updated at each time step, the Welford [80] approximation, given by Eqn. (3.56), is employed. Table 4.2 gives an overview over the averaging methods applied to the different test case configurations. Both the moving average window size and the sample time are expressed as a fraction of the characteristic shedding period $T_{\mathrm{shedd}} = f_{\mathrm{shedd}}^{-1}$, where the characteristic cavity shedding frequency for this test case is identified as $f_{\mathrm{shedd}} = 192$ Hz in Sec. 4.2.3.

Figs. 4.21 and 4.22 depict the time averaged pressure at the observation points P_0 and P_3 in Fig. 4.17, each for two different sliding window sizes applied to the same pressure signal. The black solid line represents the exact moving average, and the red solid line represents the corresponding approximation of the moving average obtained from the method by Welford [80], as given by Eqn. (3.56). The mean value obtained from averaging over the entire signal length is depicted by the yellow circular markers for reference. As the sliding window length is reduced, the moving average approaches the input signal more accurately and eventually tends to reproduce its high amplitude peaks caused

Table 4.2: Test case configurations to investigate the effect of the moving average window size on the time averaged pressure distribution.

Averaging method	Welford [80]			Exact
Moving average window sizes $T_{\text{mov}}/T_{\text{shedd}}$	0.1	0.5	1.0	69
Sample time	$T_{\text{sample}}/T_{\text{shedd}} = 53.8$			
Shedding frequency	$T_{\text{shedd}}^{-1} = f_{\text{shedd}} = 192$ Hz			

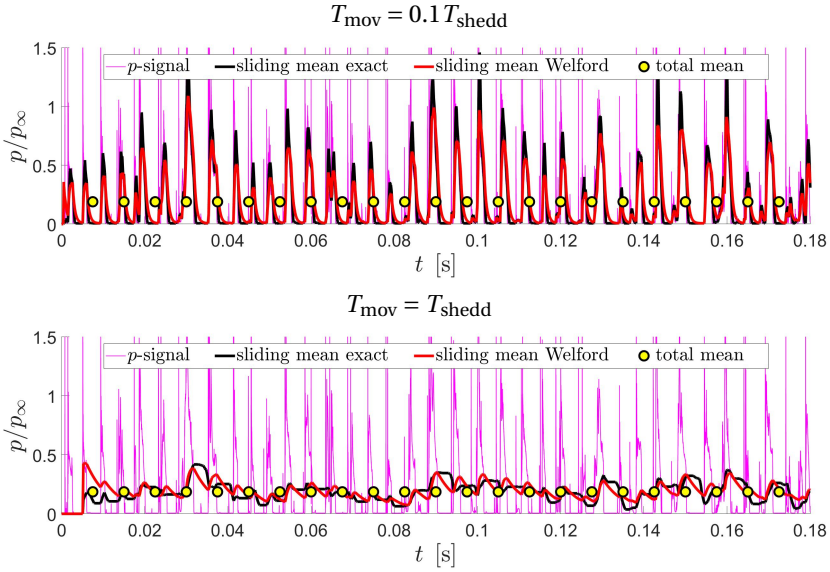

Figure 4.21: Exact moving average, its Welford [80] approximation and the total mean for a pressure signal sampled at observation point P_0 in Fig. 4.17 for two different sliding windows.

by periodic cavity collapses, where the exact moving average exhibits a somewhat more sensitive response than the Welford [80] approximation. When the moving window size approaches the characteristic shedding period T_{shedd} of the cavitating flow, the oscillations of the moving average signal around the absolute mean appear to be small relative to the ambient pressure p_∞. Consequently, the distribution of the driving pressure p_d, which is assumed to be equal to the time averaged pressure $\langle p \rangle$, can be expected to be rather insensitive to the sliding window size T_{mov} when T_{mov} is of the order of the charac-

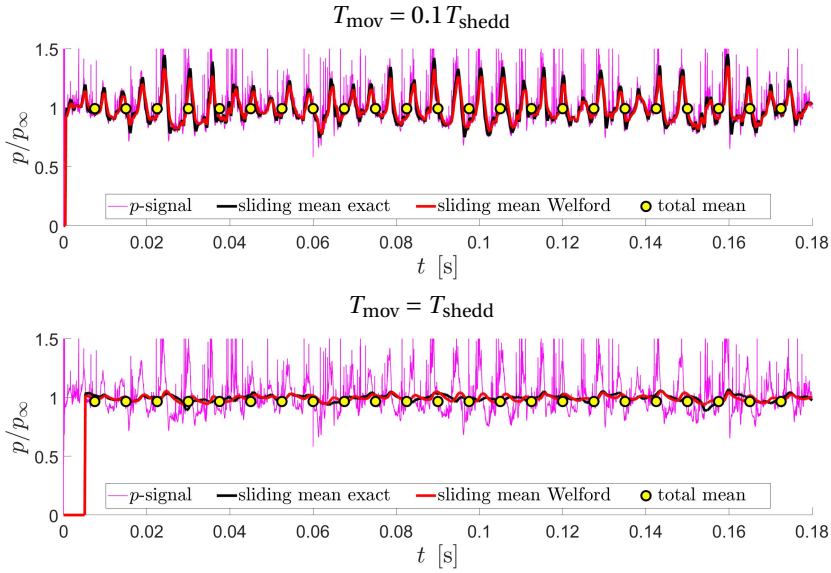

Figure 4.22: Exact moving average, its Welford [80] approximation and the total mean for a pressure signal sampled at observation point P_3 in Fig. 4.17 for two different sliding windows.

teristic shedding period T_{shedd} or larger. This is further supported by Fig. 4.23, depicting the instantaneous distribution of the time averaged pressure $\langle p \rangle$ on the foil surface and the tunnel side wall for four different sliding window sizes (see Table 4.2) and the same instantaneous flow situation. The distributions appear to be very similar, except for the smallest sliding window $T_{mov} = 0.1\,T_{shedd}$, where the low pressure footprints caused by the presence of the cavities become more noticeable. The reason for this behavior is that a large sliding window gives more time to filter out the cavity footprint as it passes some observation point.

Fig. 4.24 shows the distribution of surface energy accumulated on the hydrofoil surface per sample time, given by $\langle \dot{e}_S \rangle_{\{n=1\}} = \langle \dot{e}_S \rangle = e_S\left(T_{sample}\right)/T_{sample}$. The results are obtained from the energy focusing approach. Again, the four sliding windows given in Table 4.2 were employed to compute the driving pressure p_d in Eqn. (3.29). For the larger sliding windows $T_{mov} \geq 0.5\,T_{shedd}$, the surface energy distribution appears to be rather insensitive to the sliding window size, which is due to the insensitivity of the driving pressure distribution in this sliding window range. However, for the small sliding window $T_{mov} = 0.1\,T_{shedd}$, a pronounced decrease of the surface energy magnitude is observed in Fig. 4.24. Again, this is explained by the fact that the local moving average of the pressure is increasingly affected by the low pressure footprint of the cavities as the sliding window size is reduced. In the limit $T_{mov} \to 0$, where the driving pressure would be equal to the instantaneous pressure p, we would have $p_d \approx p_v$ in the phase transition regime. From Eqn. (3.29) then follows $\left(De_{pot}/Dt\right)_c \approx 0$, such that the resulting surface energy distribution would practically become zero.

Fig. 4.24 reveals another effect of the sliding window size on the surface energy dis-

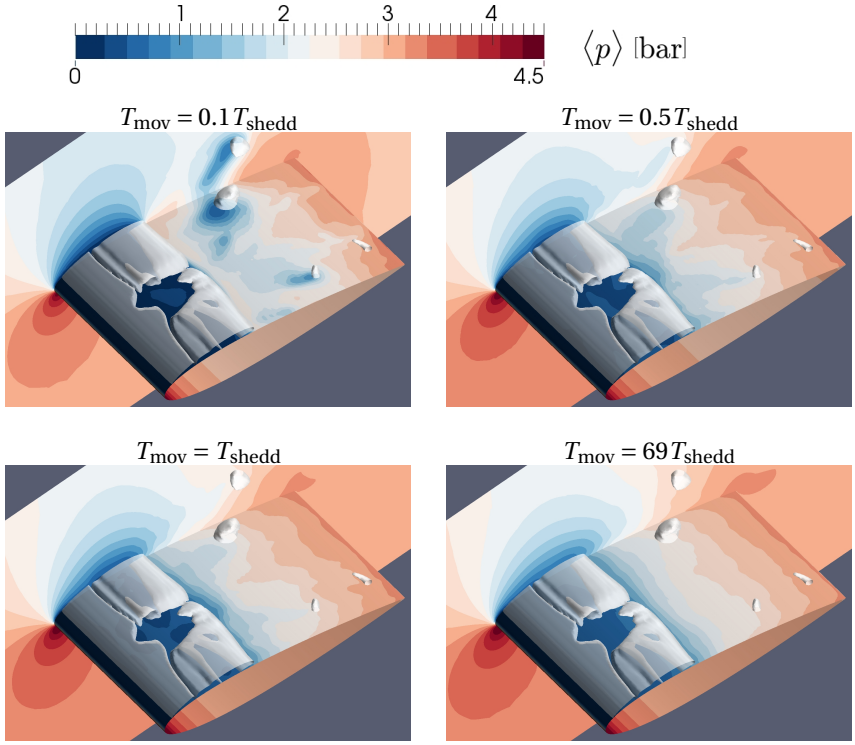

Figure 4.23: Instantaneous distribution of the time averaged pressure $\langle p \rangle$, which is assumed to be a measure of the driving pressure p_d in Eqn. (3.29). The different distributions represent different sliding time windows, over which p is averaged. The distribution for $T_{mov} = 69\,T_{shedd}$ represents the exact time average of the pressure field, whereas the remaining three distributions are obtained from the Welford [80] approximation (see Eqn. (3.56)) of the moving average.

tribution. For the case $T_{mov} = 0.1\,T_{shedd}$, the distribution peak values are observed from approximately $0.4\,c_{foil}$ onward towards the trailing edge of the foil, whereas for the larger sliding windows, the maximum values are observed close to the leading edge of the foil. This relative shift occurs because the local moving average $\langle p \rangle$ is most effectively reduced by the presence of the large sheet cavities developing at the leading edge of the foil. A larger initial cavity volume means that it takes more time for the cavity to entirely collapse or to be entirely advected along some fixed observation point, so that this observation point is subjected to the low cavity pressure for a longer time. It can be concluded from these considerations that the driving pressure computed from a sliding window significantly smaller than T_{shedd} may not give an appropriate estimate of the ambient condition that the collapsing cavities experience throughout a shedding cycle. A sliding window size of the order of the characteristic cavity shedding period or larger is therefore recommended.

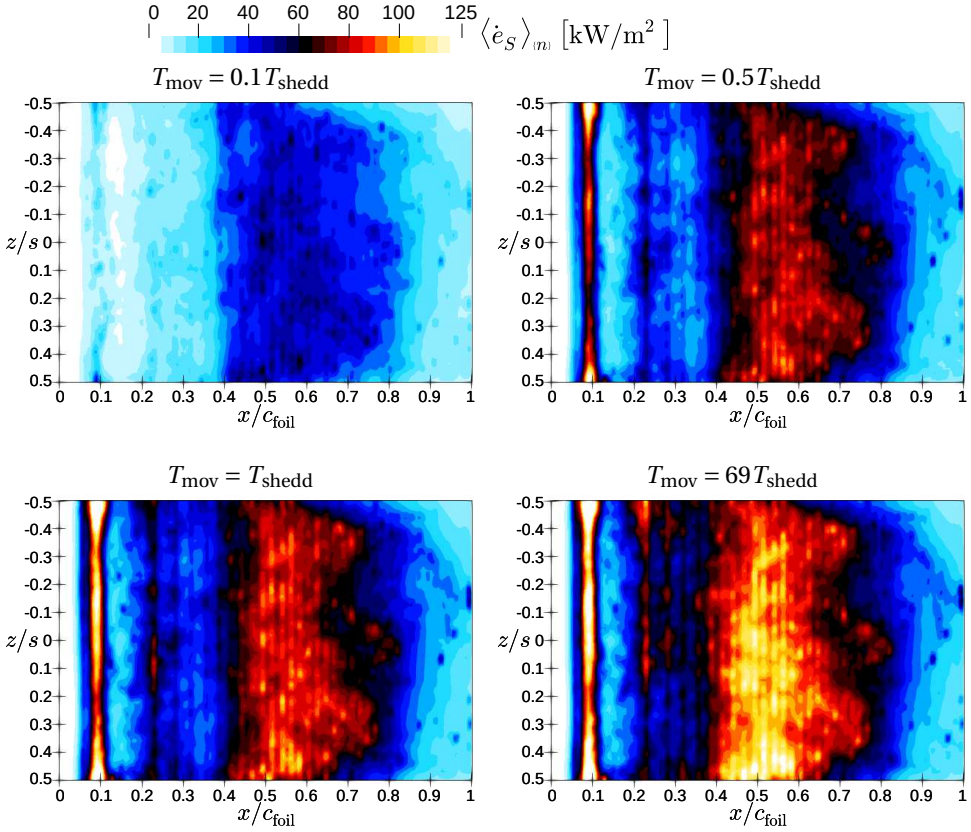

Figure 4.24: Distribution of surface energy accumulated per sample time $T_{sample} = 53.8\,T_{shedd}$ for the different sliding windows T_{mov} in Table 4.2 to compute the driving pressure p_d in Eqn. (3.29); flow from left to right; the results are obtained from the energy focusing approach; $\langle \dot{e}_S \rangle = e_S\left(T_{sample}\right) / T_{sample}$, which corresponds to the unfiltered distribution $\langle \dot{e}_S \rangle_{\{n=1\}}$.

4.2.5. IDENTIFICATION OF EXTREME EVENTS

Prior to applying the statistical analysis method introduced in Sec. 3.4 to the accumulated surface energy distribution, a typical cavity collapse sequence is investigated in detail. Figs. 4.25 and 4.26 depict exactly the same collapse sequence for both the non-focusing and the focusing approaches, respectively. The sequence shows multiple vapor structures collapsing directly downstream from the region of the maximum pressure recovery gradient at $0.4c_{foil}$, and one structure collapsing towards the trailing edge of the foil. It can be seen from Fig. 4.25 that the non-focusing approach has a tendency to smear out the radiated energy across the foil surface. This smearing occurs because the energy is radiated continuously throughout the cavity collapses, while the cavities are advected downstream by the mean flow. Especially the structure collapsing towards the trailing leaves a pronounced trace-like footprint. In comparison, Fig. 4.26 shows much more focused energy footprints, which is the result of the energy being radiated only at

the final stage of a cavity collapse. Where the non-focusing approach predicts the largest energy concentration right downstream from the pressure recovery region, the focusing approach predicts the largest concentration at the spot where the trailing edge collapse occurs. Also, the impact energy magnitudes predicted by the focusing approach are significantly higher than the ones predicted by the non-focusing approach.

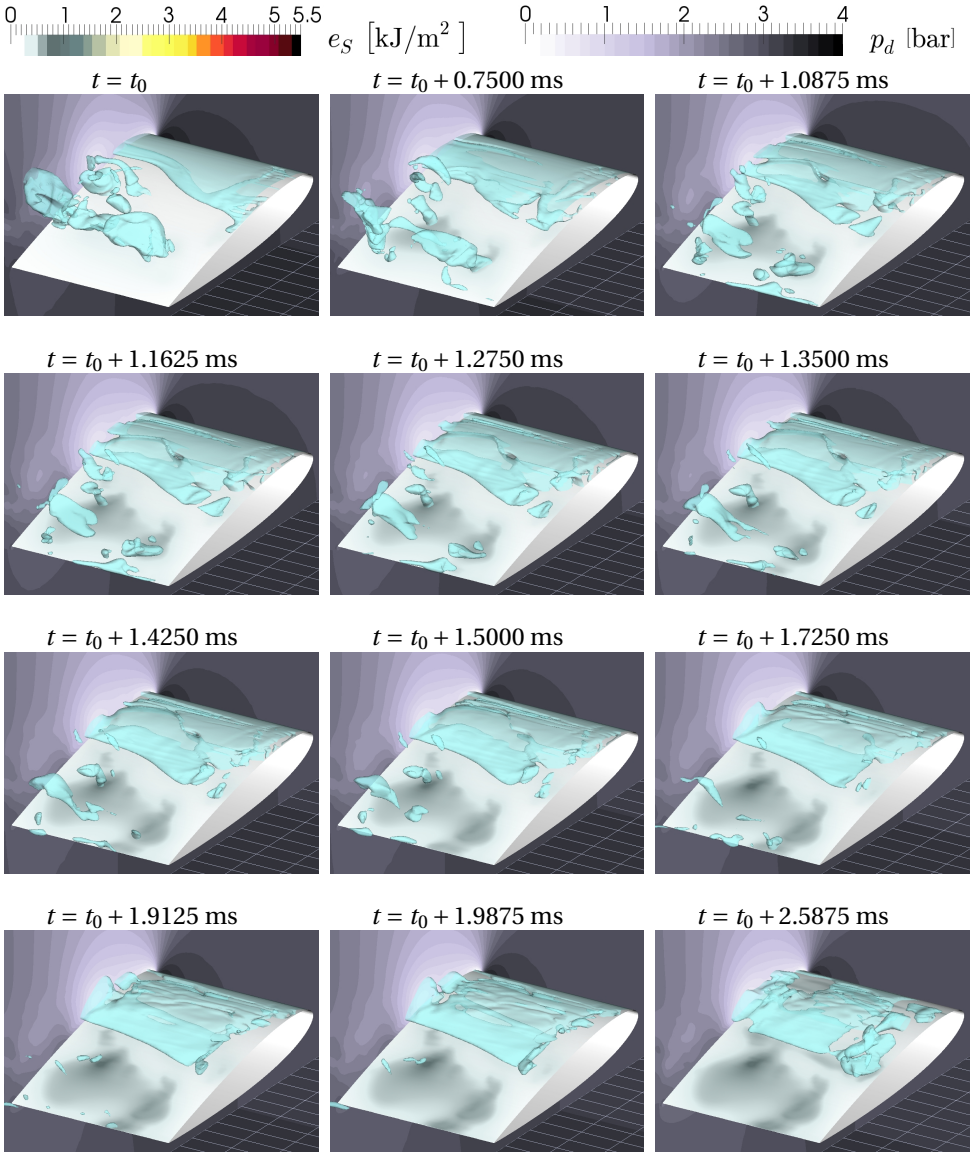

Figure 4.25: Visualization of the surface energy accumulation process over time for a typical collapse sequence obtained from the non-focusing approach (instantaneous conversion of the potential energy change induced by condensation into radiated acoustic energy).

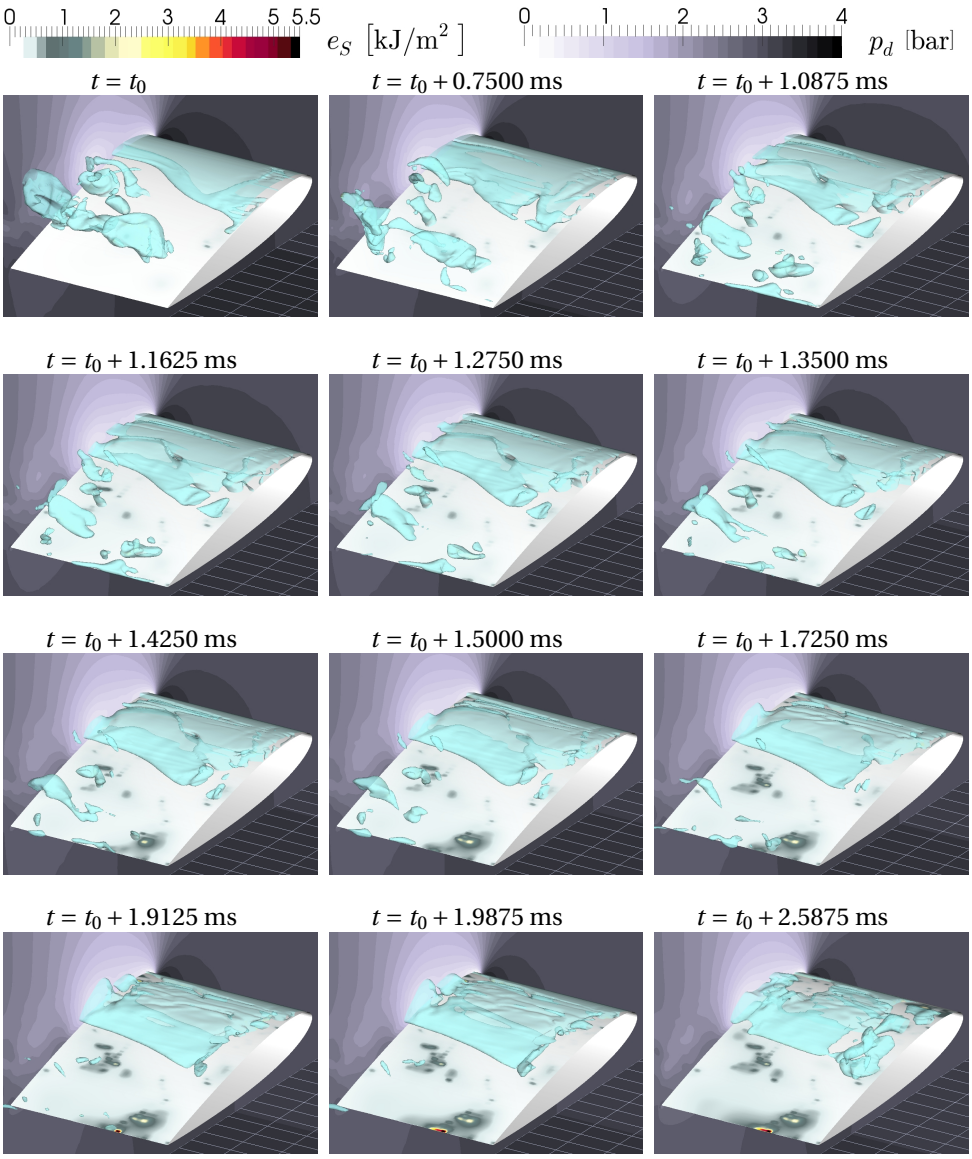

Figure 4.26: Visualization of the surface energy accumulation process over time for a typical collapse sequence obtained from the focusing approach (instantaneous conversion of the potential energy change induced by condensation into kinetic energy of the liquid and conversion of the accumulated kinetic energy into radiated acoustic energy at the final collapse stage).

To investigate the long term distribution of accumulated surface energy per sample time as well as the distribution of its extreme events, the statistical analysis method introduced in Sec. 3.4 is applied to a simulation long enough for the impact distribution to exhibit convergent behavior. As explained in Sec. 3.3.2, the surface energy distribution

is determined from the computationally efficient form given by Eqn. (3.55), where the rather expensive projection of the radiated energy accumulated from the time integrated radiation source terms is only carried out after a certain time T. In the same way, Eqn. (3.61) is employed to isolate the extreme events from the surface energy distribution. As explained in Sec. 3.4.2, the power mean analysis to attenuate the low amplitude events is again applied to the ensembles obtained from the evaluation over the individual time windows of length T_p. Where the choice of the projection frequency $1/T_p$ has no effect on the unfiltered surface energy distribution per sample time, it may well affect the filtered distribution due to the non-linearity introduced by the intensity exponent n. For this reason, the filtered time averaged impact power distribution $\langle \dot{e}_S \rangle_{\{n\}}$ is not only computed for a variation of the intensity exponent n, but also for a variation of the projection frequency $1/T_p$.

In order to investigate the effect of the intensity exponent n on the filtered averaged impact power distribution, the projection frequency is kept constant at $1/T_p = 1/T_{\text{shedd}}$. The simulation time is 0.469 s, which corresponds to 90 shedding cycles at a shedding frequency of $f_{\text{shedd}} = 192$ Hz. As it can be seen from Eqn. (3.61), $n = 1$ gives the unfiltered accumulated surface energy distribution per sample time. Two more variations of the intensity exponent ($n = 1.5$ and $n = 5.0$) are investigated. Fig. 4.27 shows the results for both the non-focusing (left) and the focusing approach (right). For both approaches, the impact scatter increases with increasing n, because the extreme events are highly local phenomena. It can also be seen that the impacts occurring downstream from the pressure recovery region at $0.4c_{\text{foil}}$ become more pronounced relative to the leading edge impacts as the intensity exponent n increases. This observation indicates that not only the impact scatter, but also the intensity of the individual events, increases towards the trailing edge. Close to the leading edge, the impact events are mostly associated with the collapse of some part of the sheet cavity. The downstream surface energy distribution is governed by the cyclic collapse of vapor structures pinched off from the sheet cavity. In this particular case, the re-entrant jet mechanism is the driving shedding mechanism [29, 82, 88], where the adverse pressure gradient caused by the stagnation point at the sheet cavity closure drives a thin upstream liquid film. When this liquid jet looses its momentum, it is deflected away from the foil surface, thereby pinching off some part of the sheet cavity [89]. The pinch-off leads to the formation of vorticity [89]. In the simulation of cavitating flows, the formation of vorticity is observed even in the absence of viscous forces [90], and it is interpreted as an intrinsic inertia controlled instability [71, 90]. Furthermore, baroclinic instabilities may occur when the gradients of pressure and densities are not aligned [91]. However, this can only be the case in non-barotropic flows [46]. As the shed cavities are advected downstream, the flow vorticity is further amplified in regions where the divergence of the mixture fluid is negative [92], as well as by vortex stretching [91]. Due to the enhanced vorticity, the shed cavities can break up into secondary vortical ring structures [93], which may form horseshoe type cavitating vortices when attached to the solid surface [94]. Compared to the scattered impacts caused by the collapse of vortical vapor structures downstream from the pinch-off region, the collapses close to the leading edge can, despite their lower amplitude, more efficiently accumulate in the unfiltered surface energy distribution, because they occur at practically every cycle and in a very confined area around $0.1c_{\text{foil}}$. The more the lower

amplitudes are attenuated by the intensity exponent n, the more they are filtered away from the energy distribution, and hence from the time averaged impact power distribution. Fig. 4.27 further shows that the filtered time averaged impact power distribution obtained from the focusing approach is less sensitive to a variation of n compared to the filtered distribution obtained from the non-focusing approach. This can be explained by the fact that the focusing approach itself already leads to more isolated and extreme impacts compared to the non-focusing approach.

The effect of the projection frequency $1/T_p$ on the filtered time averaged impact power distribution is investigated for $n = 2$ and three different projection frequencies as shown in Fig. 4.28. Again, the simulation time is 0.469 s (90 shedding cycles). For both the non-focusing approach (left) and the focusing approach (right), the lower magnitudes of the distribution tend to become more attenuated with increasing T_p. That is, because extreme events are more likely to occur within the period T_p when T_p increases.

From the analysis so far, it can also be seen that especially the averaged impact power distribution obtained from the focusing approach requires a significant amount of shedding cycles until the statistics exhibit sufficient convergence. This behavior is due to the focusing of the radiated energy into the collapse center, which enhances the scatter of the surface energy distribution. For this reason, a long simulation involving 200 shedding cycles (1.04175 s) is carried out to investigate the averaged impact power distribution obtained from both the non-focusing and the focusing approach. The corresponding unfiltered distributions ($n = 1.0$) shown in Fig. 4.29 appear to be very similar as far as the magnitude downstream from the pressure recovery region at $x = 0.4c_{\text{foil}}$ is concerned. In particular, the difference in surface energy magnitude observed in this area is significantly smaller than what is obtained from a short duration analysis. This effect can be seen by comparing the $n = 1.0$ distributions in Fig. 4.29 with the accumulated surface energy distribution depicted in Fig. 4.30. The surface energy distributions in Fig. 4.30 were obtained from a relatively short sample time of $1.43T_{\text{shedd}}$, where the differences in energy magnitude are much more pronounced than in Fig. 4.29. The reason for this difference is that the events computed from the focusing approach can only form a smooth surface energy distribution in a statistical sense, when the sample time T is large enough. As the time averaged amount of radiated energy is the same for both approaches, the surface energy distribution obtained from the focusing approach eventually resembles the one obtained from the non-focusing approach, despite the fact the individual events computed from the focusing approach are of significantly larger amplitude. However, it is also observed that the energy extent obtained from the focusing approach reaches further downstream by a distance of approximately $0.1c_{\text{foil}}$. This is the result of the shed cavities being advected downstream during their collapse. As the focusing approach allows the energy radiation to take place only at the final collapse stage, the involved advection has a tendency to stretch the surface energy distribution further downstream compared to the non-focusing approach. For the same reason, the focusing approach has a tendency to focus the energy radiated in the vicinity of the leading leading onto a more confined surface area. The same behavior is observed for the filtered time averaged impact distributions ($n = 5.0$). However, even after 200 shedding cycles, the filtered distribution obtained from the focusing approach appears to be highly scattered and far from forming a smooth time averaged distribution.

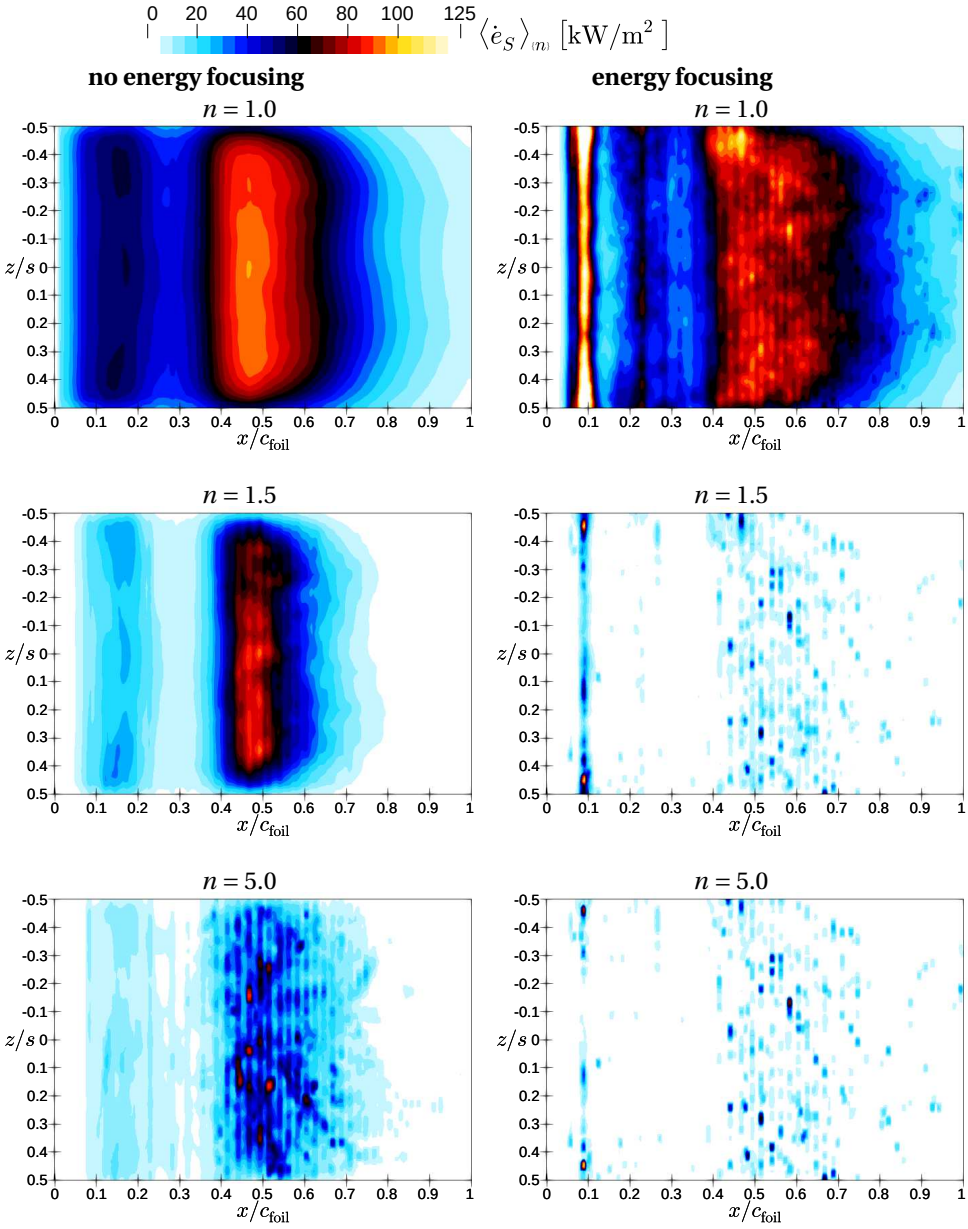

Figure 4.27: Distribution of the accumulated surface energy per sample time (involving 90 shedding cycles) obtained from the non-focusing approach (left) and the focusing approach (right) for a variation of the intensity exponent n introduced in Sec. 3.4, where $n = 1$ represents the unfiltered surface energy distribution and $n > 1$ the filtered surface energy distribution in which the contributions resulting from low amplitude impacts are attenuated to an extent governed by the value of n; the projection frequency $1/T_p$ (see Sec. 3.4.2) is equal to the shedding frequency $1/T_{\text{shedd}}$; flow from left to right.

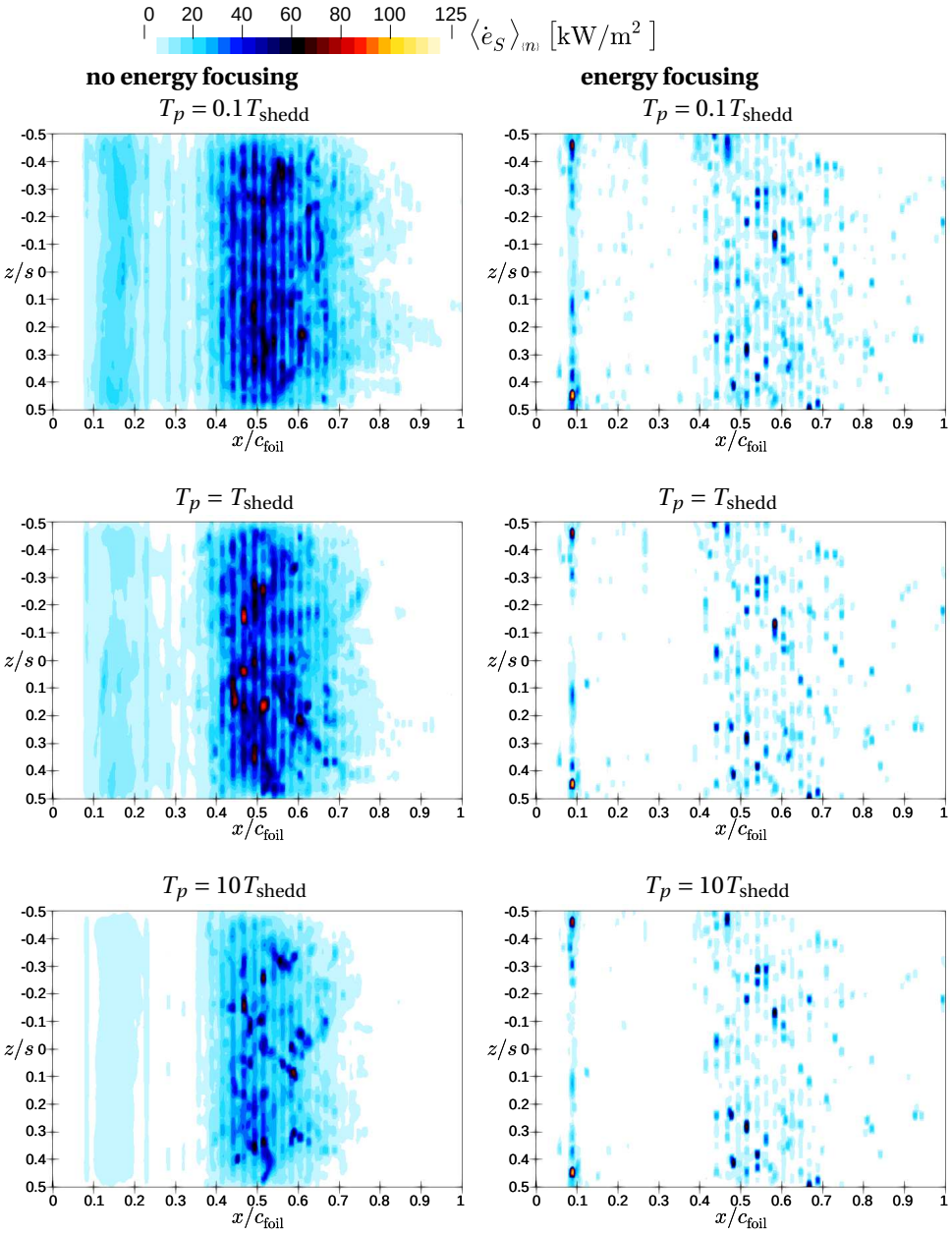

Figure 4.28: Distribution of the accumulated surface energy per sample time (involving 90 shedding cycles) obtained from the non-focusing approach (left) and the focusing approach (right) for a variation of the projection frequency $1/T_p$ introduced in Sec. 3.4.2, where $1/T_p$ is the frequency at which the accumulated filtered radiation source terms are projected onto the foil surface and where T_{shedd} is the cavity shedding frequency; the value of the intensity exponent (see Sec. 3.4) is constant and equal to $n = 2$; flow from left to right.

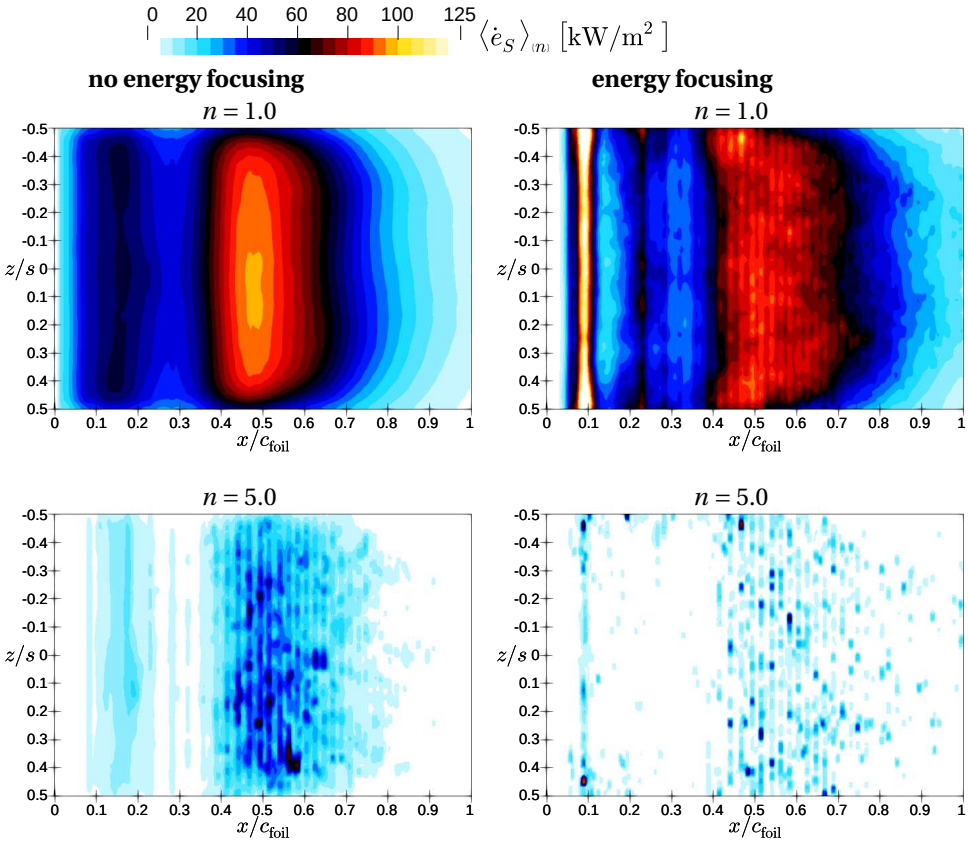

Figure 4.29: Distribution of the unfiltered (top, $n = 1$) and the filtered (bottom, $n = 5$) accumulated surface energy per sample time obtained from the non-focusing approach (left) and the focusing approach (right) after 200 shedding cycles.

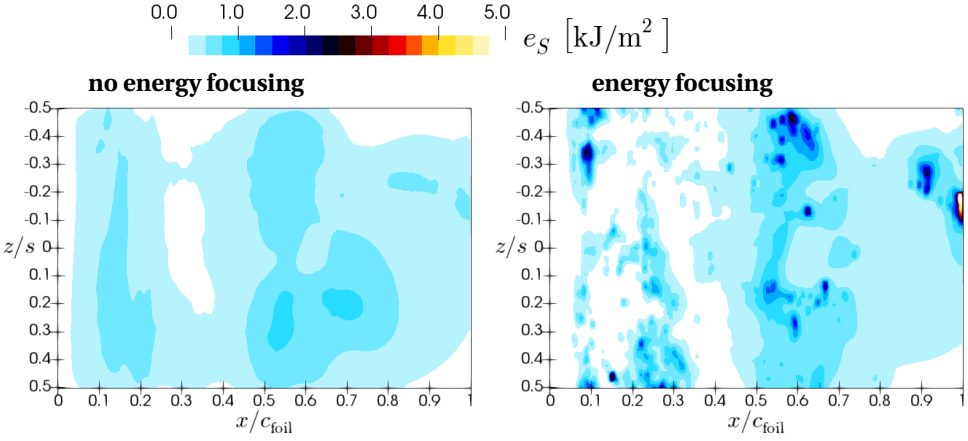

Figure 4.30: Distribution of the accumulated surface energy ($n = 1$) obtained from the non-focusing approach (left) and the focusing approach (right) after 1.43 shedding cycles.

4.2.6. COMPARISON AGAINST EXPERIMENTAL PAINT TEST RESULTS

Fig. 4.31 shows a comparison of the extreme event distribution ($n = 5.0$) obtained from both the focusing (A) and the non-focusing (B) approaches against the experimental damage pattern found by van Rijsbergen *et al.* [82] (C) and numerical results by Li *et al.* [29] (D). The damage pattern obtained by van Rijsbergen *et al.* [82] from experimental paint tests shows qualitative agreement with the numerical results in the sense that the main impact region stretches from approximately $0.1c_{\text{foil}}$ onward towards the trailing edge of the foil up to approximately $0.9c_{\text{foil}}$. It is noted that the comparison can be of qualitative nature only. It was shown by Mantzaris *et al.* [95] that the reproducibility of paint tests is limited, because the painting procedure or other parameters such as paint thickness, can strongly affect the results. Different from the numerical results, the experimentally obtained damage pattern is more focused towards the mid-span of the foil. This difference is most likely attributed to viscous forces causing a deflection of the re-entrant jet from the tunnel side wall, thereby focusing the shed cavities towards the mid-span [82, 89]. Different from the approach presented in the present work, Li *et al.* [29] assumed the local partial time derivative of the pressure $\partial p/\partial t$ to be a measure for the impact aggressiveness. They derived an erosion risk indicator $I_{\text{Erosion}} = 1/N \sum_{i=1}^{N} I_i$, where $I_i = \partial p/\partial t$ if $\partial p/\partial t$ exceeds a predefined threshold level and $I_i = 0$ otherwise [29]. The aggressiveness distribution obtained by Li *et al.* [29] for the same test case and operating conditions in Fig. 4.31 (D) indicates the most aggressive region right next to the leading edge, where the threshold level was equal to $3 \cdot 10^9$ [29]. Even though the close vicinity of the leading edge had to remain unpainted in the experiment by van Rijsbergen *et al.* [82], due to the presence of roughness grains, it is likely that Li *et al.* [29] overpredict the flow aggressiveness at the leading edge relative to the flow aggressiveness further downstream. However, the most important difference is that the relative flow aggressiveness predicted from the pressure time derivative does not seem to shift towards the trailing edge when the threshold level is increased. The downstream impacts even disappeared in the study by Li *et al.* [29] when exceeding a certain threshold, whereas the leading edge impacts were still captured. On the contrary, the cavitation implosion load model and the statistical analysis method introduced in the present work, predict an increasing aggressiveness of the downstream collapse events as the value of the intensity exponent n increases. Another beneficial feature of the present model is that it is designed to rigorously control the energy balance of the macroscopic cavitating structures, thereby allowing for quantitative predictions of the impact loads. On the other hand, Li *et al.* [29] predict a distinct impact region close to the tunnel side wall, which is also observed in the experiment by van Rijsbergen *et al.* [82]. Such a distinct region is not observed in the present work, which is again attributed to neglecting viscous forces, because the deflection of the re-entrant jet due to the presence of the side-wall boundary layer [29] may lead to the formation of a cavitating vortex in the corner between the foil surface and the tunnel side wall.

A) energy focusing, $n = 5.0$

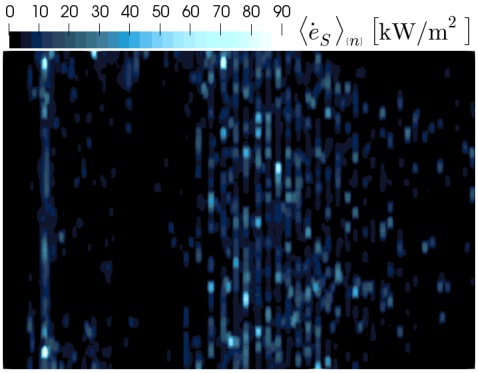

B) no energy focusing, $n = 5.0$

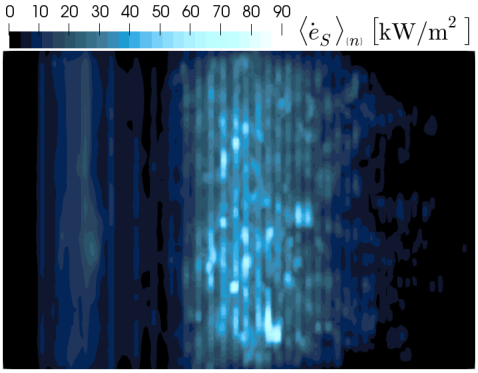

C) experimental damage pattern [82]

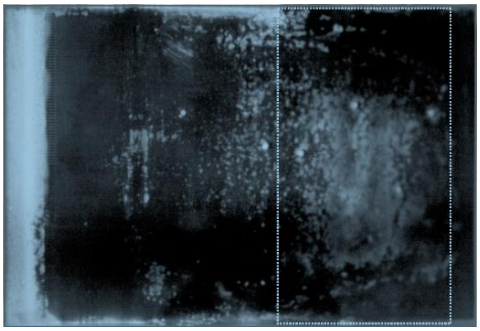

D) $\partial p/\partial t$-criterion [29]

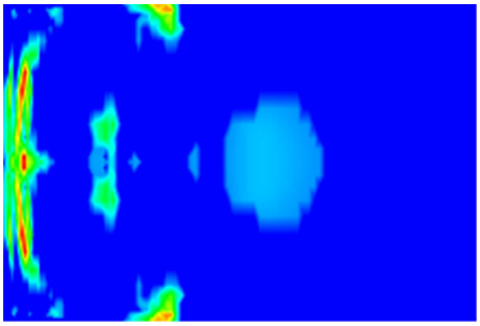

Figure 4.31: Comparison of the extreme event distribution ($n = 5.0$) obtained from the energy focusing (A) and the non-focusing approach (B) to the damage pattern (C) on the NACA0015 hydrofoil surface obtained by van Rijsbergen *et al.* [82] from experimental paint tests (rotated by 180°) and high erosion risk areas identified by Li *et al.* [29] (D) from numerical modeling (the colored figure is found in [96], rotated by 180°); the results by Li *et al.* [29] are obtained from the erosion risk indicator $I_{\text{Erosion}} = 1/N \sum_{i=1}^{N} I_i$, where $I_i = \partial p/\partial t$ if $\partial p/\partial t \geq$ threshold (=$3 \cdot 10^9$) and $I_i = 0$ otherwise; the flow is from left to right.

4.2.7. RECOMMENDATIONS FOR THE AGGRESSIVENESS ASSESSMENT OF PERIODIC CAVITATING FLOWS

The summarized findings from the study of the cyclic cavitating flow around the NACA0015 hydrofoil address three parameters that must be specified in the analysis procedure to assess the aggressiveness of periodic cavitating flows.

The first parameter is the length of the moving time window T_{mov} to estimate the instantaneous driving pressure distribution. The driving pressure p_d is assumed to be equal to the moving time averaged pressure for which the approximation by Welford [80] (see Eqn. (3.56)) is employed. It is concluded from a systematic variation of the time window length T_{mov} that the driving pressure distribution is rather insensitive to T_{mov} when $T_{\text{mov}} \geq T_{\text{shedd}}$, where T_{shedd} is the characteristic shedding period. Exhaustively large moving time windows are not preferred, because the initial build-up of the mov-

ing time averaged pressure takes at least as long as the time window length itself. It is therefore recommended to choose T_{mov} equal to T_{shedd} or, in case of doubt, somewhat larger.

The second parameter is the frequency $1/T_p$ at which the accumulated radiation energy is projected from the sources onto the target surface. In order to keep the simulation computationally efficient, T_p should be much larger than the simulation time step Δt, especially for simulations involving a large number of grid cells. Where the choice of T_p has no effect on the unfiltered surface energy distribution, it may well affect the extent by which the low amplitude events are attenuated in the filtered energy distribution due to the non-linearity introduced by the intensity exponent n in Eqn. (3.61). Irrespective of whether the unfiltered energy distribution or the extreme event distribution is of interest, it is recommended to choose the projection frequency $1/T_p$ equal to the characteristic shedding period T_{shedd}. The reason is that the energy distribution per shedding cycle that is obtained in this manner can be assumed to approximately represent the distribution of isolated events that occurred during that specific cycle. Knowledge of the energy content resulting from isolated events may allow a coupling of the implosion load model to material properties of the target surface.

The third parameter is the intensity exponent n needed in the filtering method to attenuate the low amplitude events from the surface energy distribution as described in Sec. 3.4. Large values of $n \geq 2$ are generally recommended to obtain a clear indication of the extreme event distribution. In order to prevent precision errors, n should not be chosen arbitrarily large, because of the excessive magnitudes of the amplified radiation source terms $(\dot{e}_{\text{rad}})^n$ that are possible in Eqn. (3.61). If necessary in future work, this numerical problem could be solved by an appropriate normalization of the radiation source term $\dot{e}_{\text{rad}}$ prior to its amplification by the intensity exponent n.

4.3. AXISYMMETRIC NOZZLE

4.3.1. NUMERICAL SET-UP

The axisymmetric nozzle test case was originally designed and investigated experimentally by Franc *et al.* [83]. The geometry depicted in Fig. 4.32 essentially consists of a circular vertical inflow section of tube diameter r_t at the end of which the flow is deflected into a small gap of height h_g between two horizontal discs. The connection between the vertical inflow section and the horizontal upper disc is rounded, with r_a being the rounding radius. At the center of the lower disc, the incoming flow forms a stagnation point. The geometry of the set-up and the flow conditions are such that the cavitating flow is very likely to result in erosive cavitation. Such conditions are achieved by rather high inflow speeds in the vertical tube section at high ambient pressure, such that the inflow has a relatively high energy content. Due to the high ambient pressure, a strong local flow acceleration is needed to achieve a pressure drop large enough for cavitation to occur. This acceleration is for one part achieved by forcing the flow into the small gap between the discs and for the other part by the small rounding radius r_a. Downstream from the location of cavitation inception, the rapid increase of cross sectional area in radial direction causes a pronounced pressure recovery gradient. As a result, the vapor cavities rapidly implode under relatively high ambient pressure and in a rather

confined zone around the disc center. The dimensions and geometrical specifications of the computational domain depicted in Fig. 4.32 as well as the fluid properties and operating conditions for the numerical simulation are given in Table 4.3. The fluid properties are associated with water at 20°C, keeping in mind, however, that the simplifying mass transfer cavitation model employed in this work cannot reflect the exact variation of thermodynamic states during operation. The inflow speed u_{in} and the corresponding inflow cross sectional area πR_1^2 as well as the exit pressure p_{out} at the outlet are in line with the numerical set-ups used by Mihatsch *et al.* [97], Peters *et al.* [98], and Schreiner *et al.* [99]. With these operating conditions, the experimental conditions at which a pressure drop of $\Delta p = p_{\text{up}} - p_{\text{out}} = 21.1$ bar was obtained, are mimicked. This corresponds to a cavitation number of $\sigma = \left(p_{\text{out}} - p_v\right)/\Delta p = 0.9$ [83]. The large downstream reservoir attenuates pressure fluctuations at the outlet, where a fixed value (Dirichlet) boundary condition for the pressure is applied. Further boundary conditions are specified in Table 4.3. The computational grid depicted in Fig. 4.33 corresponds to the second coarsest mesh in Table 4.3 with 15 cells over the gap height h_g. A slight refinement of the overall expansion ratio of 2 towards the upper disc is applied to better capture the sheet cavity development and the shedding process. In order to conduct a grid sensitivity study, the grid density is systematically varied in the cavitating region, where the number of cells in the vertical, radial, and circumferential directions are varied by the same factor, such that geometrically similar grids are obtained.

In the experiment by Franc *et al.* [83], the lower disc is chosen to be the sample disc to measure the pitting rate and the erosion pattern caused by the cavitating flow. An example of the eroded target disc obtained by Franc *et al.* [83] is depicted in Fig. 4.34, where the red circles at $r_1 = 19$ mm and $r_2 = 32$ mm were added by Mihatsch *et al.* [97] to indicate the region of most erosive cavitation. This erosion pattern is compared to the distribution of accumulated surface energy predicted by the acoustic model introduced in Sec. 3.2, where r_1 and r_2 are indicated for reference. The driving pressure p_d needed to determine the potential energy content in the collapse energy balance, is assumed to be given by the moving time averaged pressure as specified in Sec. 3.1.3. The frequency of the moving time window is chosen to be $1/T_{\text{mov}} = 1000$ Hz. This choice is based on the finding from Sec. 4.2.4 that the surface energy distribution obtained from the acoustic model becomes insensitive with respect to T_{mov} if T_{mov} is larger than the characteristic cavity shedding period T_{shedd}. As it will be shown from the flow sensitivity analysis for the present set-up, that non of the obtained shedding frequencies falls below 1000 Hz, which means that also the convergence of the surface energy distribution can be checked for this frequency without being affected by the choice of T_{mov}.

It is further important to note that the radius of curvature r_a of the rounded edge connecting the inlet throat with the upper horizontal disc is not consistently reported in literature, where both the values 1.5 mm [17, 100] and 1.0 mm [97, 98, 101] are found. Therefore, we briefly reflect here to what extent the value of r_a may affect the sheet cavitation dynamics. With the velocity definitions in Fig. 4.35, the flow velocity $u_\theta(\theta)$ along the rounded edge is expressed as follows:

$$u_\theta = \left(\overline{u}_2 - \overline{u}_1\right) f(\theta) + \overline{u}_1 \tag{4.2}$$

In Eqn. (4.2), $\overline{u}_2 - \overline{u}_1$ represents the velocity increase due to the reduction of cross

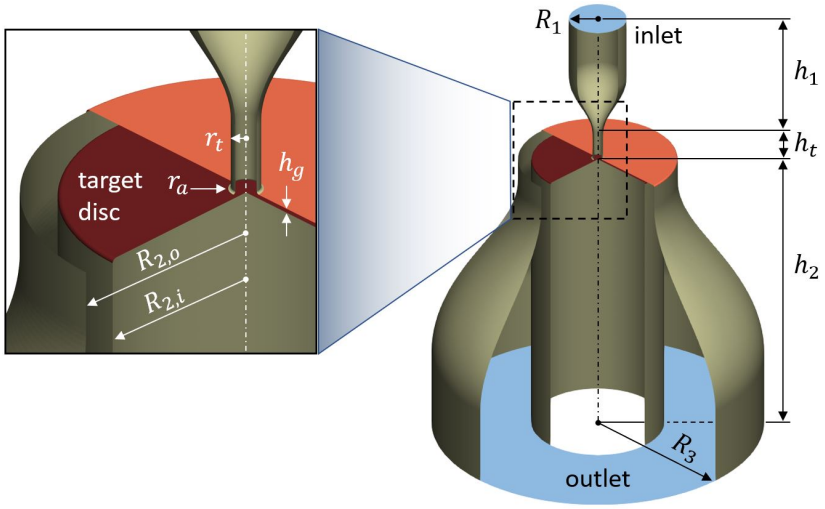

Figure 4.32: Computational domain of the axisymmetric nozzle; cavitation develops at the small rounding (radius r_a) conntecting the inlet throat with the upper horizontal disc; the lower horizontal disc is the target surface on which the erosive aggressiveness of the cavitating flow is observed.

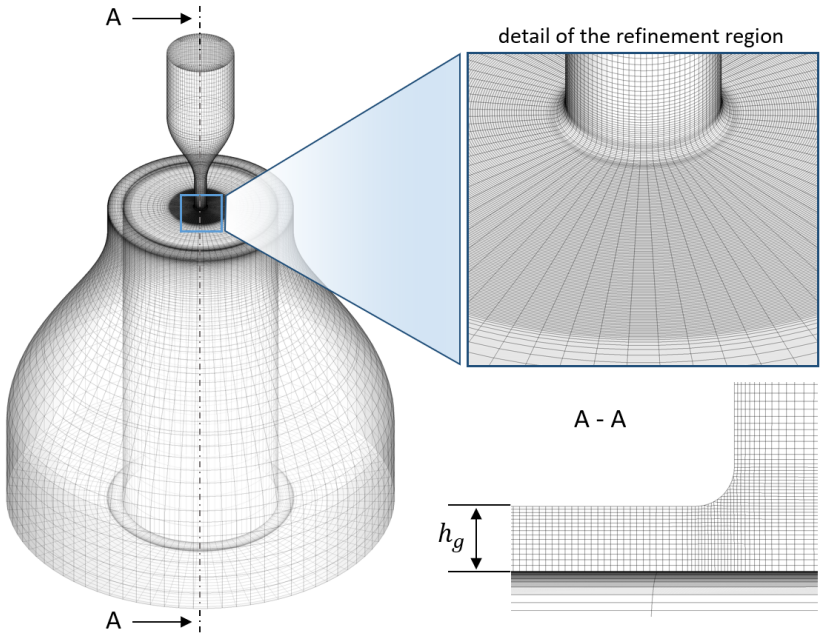

Figure 4.33: Computational grid corresponding to a resolution of 15 cells/h_g in Table 4.3 with a cross-sectional view (A-A) at the gap (height h_g) between the upper and the lower disc.

sectional area, where $\overline{u}_1$ and $\overline{u}_2$ are the velocities averaged over the cross section areas

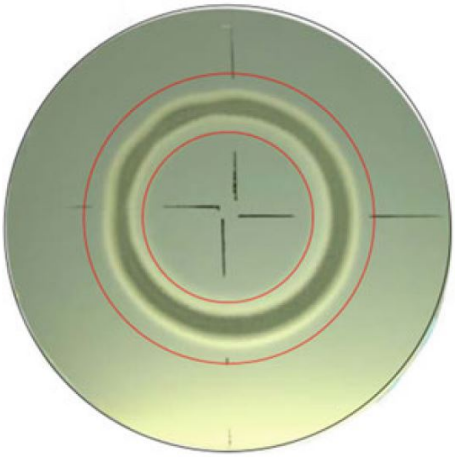

Figure 4.34: Eroded target disc from the experiment by Franc *et al.* [83], image taken from [97] who have included the red circles at $r_1 = 19$ mm and $r_2 = 32$ mm to indicate the erosive zone.

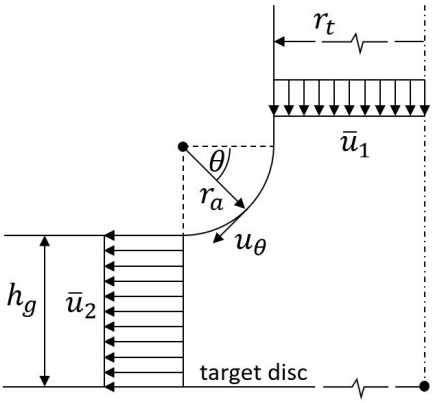

Figure 4.35: Illustration of the velocities obtained from simplifying considerations based on Bernoulli's equation; cavitation inception is expected at the point of maximum flow velocity u_θ, where the maximum value of u_θ depends on the change of cross-sectional area between the reference locations 1 and 2 and the rounding radius r_a.

indicated in Fig. 4.35. A_2 is evaluated at the downstream end of the rounded edge and A_1 at some arbitrary point in the throat section of radius r_t just upstream from the bend. From mass continuity follows that $\overline{u}_2 - \overline{u}_1 = \overline{u}_1 (A_1/A_2 - 1)$, where $A_1 = \pi r_t^2$ and $A_2 = 2\pi(r_t + r_a)h_g$, which makes A_2 a function of r_a. The function $f(\theta)$ represents the local increase of the cross sectional velocity change $\overline{u}_2 - \overline{u}_1$ due to the curvature of the rounded edge. The cavitation inception velocity u_{inc} follows directly from Bernoulli's equation, where $p_{\text{out}} = p_v + \rho u_{\text{inc}}^2/2$. Also, $p_{\text{out}} = \overline{p}_1 + \rho \overline{u}_1^2/2$. Assuming that cavitation inception occurs when the local pressure is equal to the vapor pressure, we find from Bernoulli's equation that the function value of $f(\theta)$ in Eqn. (4.2) must become

$$f_{\text{inc}}(r_a) = \frac{A_2(r_a)}{A_1 - A_2(r_a)} \left(\sqrt{\frac{p_{\text{out}} - p_v}{p_{\text{out}} - \overline{p}_1}} - 1 \right) \tag{4.3}$$

somewhere along the bend to achieve cavitation inception. In the case that $f_{\text{inc}} \leq 1$, the reduction of cross sectional area is already enough to achieve cavitation inception. For the operating conditions at hand, Eqn. (4.3) gives $f_{\text{inc}}(r_a = 1.0\text{ mm}) = 1.23$ and $f_{\text{inc}}(r_a = 1.5\text{ mm}) = 1.49$. Since $f_{\text{inc}} > 1$, the reduction of cross section area is not enough to achieve cavitation inception, such that cavitation inception can only occur as a result of the flow acceleration along the rounded edge for both values of r_a. Assuming a non-cavitating flow, one can further determine the maximum flow velocity along the rounded edge from a numerical flow simulation, which gives $u_{\max} = 83$ m/s. This gives the corresponding velocity increase factor

Table 4.3: Geometrical specifications, operating conditions, and grid densities for the axisymmetric nozzle test case

Geometry specifications	
Length of convergent inlet: $h_1 = 200$ mm	Inlet radius: $R_1 = 43.5$ mm
Throat height: $h_t = 40$ mm	Throat radius: $r_t = 8$ mm
Gap height: $h_g = 2.5$ mm	Rounding radius: $r_a = 1.5$ mm
Target disc radius: $R_{2,i} = 100$ mm	Upper disc radius: $R_{2,o} = 120$ mm
Outer reservoir radius: $R_3 = 250$ mm	Reservoir height: $h_2 = 456$ mm
Fluid properties	
Liquid density: $\rho_l = 999$ kg/m^3	Vapor density: $\rho_v = 0.017$ kg/m^3
Vapor pressure: $p_v = 2340$ Pa	
Boundary conditions	
Uniform inflow speed: $u_{\text{in}} = 1.37$ m/s	Outlet pressure: $p_{\text{out}} = 18.9$ bar
Solid walls: free slip condition ($\mathbf{u}\cdot\mathbf{n} = 0$)	Liquid fraction: $\gamma_{\text{in}} = 1$
Zero gradient (Neumann boundary condition) if not further specified	
Grid densities	
Grid density in the refinement region (detail in Fig. 4.33)	
vertical: 10 cells/h_g, circumferential: $\Delta\varphi = \pi/28$: (308700 cells in total)	
vertical: 15 cells/h_g, circumferential: $\Delta\varphi = \pi/42$: (659282 cells in total)	
vertical: 20 cells/h_g, circumferential: $\Delta\varphi = \pi/56$: (1208816 cells in total)	
vertical: 25 cells/h_g, circumferential: $\Delta\varphi = \pi/70$: (2018768 cells in total)	

$$f_{\max}(r_a) = \frac{A_2(r_a)}{A_1 - A_2(r_a)}\left(\frac{u_{\max}}{\overline{u}_1} - 1\right) \tag{4.4}$$

under wetted flow conditions. The ratio

$$\eta_{\text{inc}} = \frac{f_{\max}}{f_{\text{inc}}} = \left(\frac{u_{\max}}{\overline{u}_1} - 1\right) \Big/ \left(\sqrt{\frac{p_{\text{out}} - p_v}{p_{\text{out}} - \overline{p}_1}} - 1\right) \tag{4.5}$$

is then interpreted as the available capacity to achieve cavitation inception at the point of maximum flow velocity along the rounded edge, where $\eta \geq 1$ for cavitation inception to occur. With these values at hand, we get $\eta_{\text{inc}} = 2$ for the rounding radius $r_a = 1.5$ mm. The corresponding wetted flow pressure following from Bernoulli's equation is $p_{\min} = -15.5$ bar. For $r_a = 1.0$ mm, η_{inc} further increases, because f_{inc} decreases and $u_{\max}$ increases due to the larger rounding curvature. Therefore, cavitation inception is likely to occur for both rounding radii. As it was shown for both rounding radii that

cavitaiton inception can only occur along the rounding surface and that the cavitation inception capacity is large, it is concluded that the evolution of the sheet cavity is not affected by the choice for either of these two radii.

4.3.2. SENSITIVITY AND UNCERTAINTY STUDY ON THE CAVITY SHEDDING FREQUENCY, THE VAPOR VOLUME CONTENT AND THE IMPACT ENERGY DISTRIBUTION

The frequency analysis described in Sec. 4.2.2 is employed to investigate the sensitivity of the dominant shedding frequency with respect to grid density, time step size, and the magnitude of the mass transfer coefficients C_c and C_v as given in Eqn. (2.19). Analogous to the procedure described in Sec. 4.2.3, the averaged power spectral density $\overline{\text{PSD}}$ is computed from the pressure signals at the eight probe locations (n_{probes}=8) indicated in Fig. 4.36. The probe locations are on the upper disc, right after the small rounding at a radial distance of 9.5 mm from the center line and at equidistant circumferential distances from each other. For each probe, the sample time is $T_s = 0.013$ s, and the length of the half overlapping Hanning windows is $T_h = T_s/4$ such that the total number of Hanning windows is $n_h = 5$. The moving average window is $T_{\text{mov}} = 5 \cdot 10^{-5}$ s, which gives a cut-off frequency of 20000 Hz of the low pass filter.

It should be mentioned that the pressure probe locations are different from the ones in the experiment by Franc *et al.* [83] and the fully compressible simulations by Mihatsch *et al.* [97], who sampled the pressure signals further downstream. The reason for choosing the pressure sample locations close to the rounded edge is that this region can be expected to be subject to the cyclic development of sheet cavities, which can be expected to exhibit a more homogeneous and stable behavior in this region as compared to further downstream. This applies to the pressure field in particular, because locations occupied by liquid are likely to experience a significant pressure drop caused by nearby vaporous structures of the growing sheet. Therefore, it is expected that the power spectral density distribution of pressure obtained from the chosen probe locations give a good indication of the characteristic cavity shedding frequency identified by Mihatsch *et al.* [97] for the same operating condition.

The time averaged vapor volume present in the computational domain is measured for each configuration of the grid density, time step size, and mass transfer coefficient values. It is shown that the averaged vapor content appears to be very sensitive to the settings when the temporal or spatial resolution of the simulation is insufficient, or when the mass transfer coefficients are too small, such that the scale separation between the phase transition pressure range and the driving pressure range as discussed in Sec. 2.1.3 is not established. For this reason, an uncertainty analysis is carried out for the vapor content.

The uncertainty analysis essentially follows the method developed by Eça and Hoekstra [102], where the non-linear power function $\phi_f(h) = \phi_{f0} + \alpha h^{\mathfrak{p}}$ is fitted to the discrete data set given by n data points (h_i, ϕ_i) following the Richardson extrapolation [103]. The coefficients ϕ_{f0}, α and $\mathfrak{p}$ are determined such that the least square error estimate $S_{RE} = \sum_{i=1}^{n} \left(\phi_i - \phi_f(h_i)\right)^2$ is minimized. Eça and Hoekstra [102] derived a straightforward way to determine the solution for $\mathfrak{p}$, α and ϕ_{f0} from the conditions $\partial S_{RE}/\partial \mathfrak{p} = 0$, $\partial S_{RE}/\partial \alpha = 0$, and $\partial S_{RE}/\partial \phi_{f0} = 0$. The standard deviation σ, as derived in the work by

Eça and Hoekstra [102] for this non-linear regression, is an uncertainty measure for the entire data set. The uncertainties corresponding to the individual data points (h_i, ϕ_i) are further composed of two additional measures. One is given by the deviation of each data point ϕ_i from the corresponding fitted power function value $\phi_f(h_i)$, i.e. $|\phi_i - \phi_f(h_i)|$. The other one is given by the discretization error $\epsilon_\phi(\phi_i) = |\phi_i - \phi_{f0}|$ with respect to the extrapolated value ϕ_{f0}. Eça and Hoekstra [102] further define different uncertainty measures depending on the convergence behavior of the data set. However, in this study the same uncertainty measure is used for all data sets for better comparability between the data sets, which are given by the averaged vapor volume in the computational domain for the systematic variations of the grid resolution, the time step size, and the mass transfer coefficients, respectively. With the definitions above, the uncertainty is given by $\mathfrak{U}_\phi(\phi_i) = F_s\epsilon_\phi(\phi_i) + \sigma + |\phi_i - \phi_f(h_i)|$ [102]. In the context of grid convergence studies, the safety factor F_s is chosen according to the Grid Convergence Index (GCI) [102, 104, 105]. In this study, F_s is chosen to be equal to 1 for all data sets, again for the sake of better comparability between the data sets.

The data ϕ is represented by the time averaged vapor volume V_{vap}. Since the time step size Δt, the mass transfer coefficients $C_{c,v}$, and the characteristic cell volume V_C in the region of interest are approximately varied on a logarithmic scale, they are transformed on approximately equidistant scales as follows: $h_{\Delta t,i} = \log(\Delta t_i/\Delta t_{\min})+1$, $h_{C_{c,v}i} = \log(C_{c,v,\max}/C_{c,v,i})+1$, and $h_{V_C i} = \log(V_{C,i}/V_{C,\min})+1$, respectively. For the uncertainty estimation with respect to the grid density, a weighting factor $w_i = 1/\left(h_i \sum_{i=1}^{n} 1/h_i\right)$ is included in the S_{RE}-function, such that $S_{RE} = \sum_{i=1}^{n} w_i \left(\phi_i - \phi_f(h_i)\right)^2$ and $\sum_i^n w_i = 1$ [102]. This weighting yields a smaller standard deviation of the fitted function in this case, where the h_i-values of the data set are increasingly densely distributed towards $h = 1$. Since the number of grid cells is varied by the same factor in vertical, radial and circumferential direction, the ratio $V_C/V_{C,\min}$ can be expressed by $(1/n_{\text{cells}})^3/(1/25)^3$, where n_{cells} is the number cells per height h_g as given in Table 4.3 and indicated in Fig. 4.33, and where $n_{\text{cells}} = 25$ for the finest grid.

Figs. 4.37 to 4.39 depict the normalized averaged power spectral density distribution of the pressure obtained from the procedure described in Sec. 4.3.2 for a systematic variation of grid density, time step size Δt, and the value of the mass transfer coefficients $C_{c,v} = C_c = C_v$, respectively. As explained in Sec. 4.3.2, the frequency obtained from this analysis can be seen as characteristic for the cavity shedding process. The sample time is 0.013 s in all cases. For the configuration that is shown to give a converged solution, the sample time corresponds to 20.5 shedding cycles. The grid sensitivity analysis in Fig. 4.37 shows that the characteristic frequency is rather insensitive with respect to the grid density. Only a slight tendency towards higher frequencies is observed for the coarser grids. The time step size Δt on the other hand appears to have more effect on the shedding behavior, where too large time steps in the order of 10^{-6} s tend to decrease the characteristic frequency. However, with decreasing Δt, a convergent behavior of the power spectral density distribution in Fig. 4.38 is observed. Fig. 4.39 shows that the characteristic frequency also converges with increasing values of the mass transfer coefficients $C_{c,v}$. In this particular case, convergence is achieved for magnitudes of 5 kg·s/m^5 or larger. Only for the smallest magnitude $C_{c,v} = 0.5$ kg·s/m^5, the higher frequencies become strongly attenuated. For the largest magnitude $C_{c,v} = 5 \cdot 10^4$ kg·s/m^5,

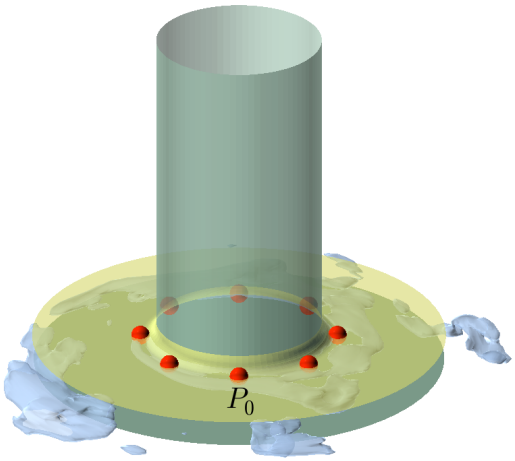

Figure 4.36: Instantaneous vapor structures between the horizontal discs; pressure probes are taken at the eight indicated locations on the upper disc ($r = r_t + r_a$, uniformly distributed in circumferential direction);

a slight stretch of the $\overline{\text{PSD}}$ distribution to lower frequencies is observed. As it can be seen from Fig. 4.40, this stretch is counteracted by further decreasing the time step from $\Delta t = 1 \cdot 10^{-7}$ s to $\Delta t = 5 \cdot 10^{-8}$ s. This indicates that a converged solution can only be obtained when sufficient temporal resolution in combination with sufficient mass transfer capacity is provided.

The convergence behavior of the time averaged vapor volume V_{vap} in the computational domain is investigated for the same variations of grid densities, time step sizes, and mass transfer coefficient values as for the frequency analysis. Again, the simulation time is 0.013 s. The results are shown in Figs. 4.41, 4.42 and 4.43, where the varied quantities are shown on a logarithmic scale to apply the uncertainty estimation procedure described in Sec. 4.3.2. At this scale, the value 1 represents the finest grid, the smallest time step, and the largest mass transfer coefficient, respectively. All data sets exhibit convergent behavior with increasing grid resolution, decreasing time step size and increasing mass transfer coefficient values, respectively. Also, for all three data sets, the uncertainties of the individual data points are predominantly governed by the difference between the simulated value V_{vap} and the extrapolated value for infinitesimal grid cells, time steps, and infinitely large mass transfer coefficient values, respectively. Fig. 4.41 shows that the uncertainty obtained for the finest grid (25 cells/h_g) is still relatively large compared to the uncertainties for the smallest time step and the largest mass transfer coefficient in Figs. 4.42 and 4.43. One of the possible reasons for this behavior is the smaller amount of data points involved in the uncertainty estimation. While insufficient spatial resolution leads to an underestimation of the vapor volume content, Fig. 4.42 shows that insufficient temporal resolution results in an overestimation of vapor content. An underestimation of vapor volume is again obtained for very small values of the mass transfer coefficients $C_{c,v}$ in Fig. 4.43. Obviously, no vapor can be produced

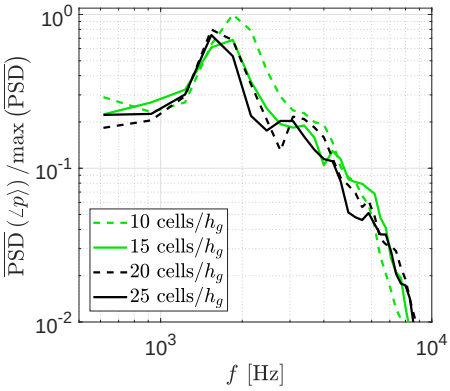

Figure 4.37: Normalized power spectral density distribution of pressure (averaged over the probe locations in Fig. 4.36) for different grid densities; $\Delta t = 1.0 \cdot 10^{-7}$ s and $C_{c,v} = 5 \cdot 10^3$ kg·s/m^5.

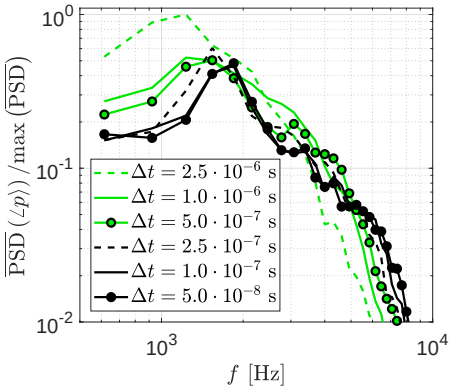

Figure 4.38: Normalized power spectral density distribution of pressure (averaged over the probe locations in Fig. 4.36) for different time steps; 15 cells/h_g and $C_{c,v} = 5 \cdot 10^3$ kg·s/m^5.

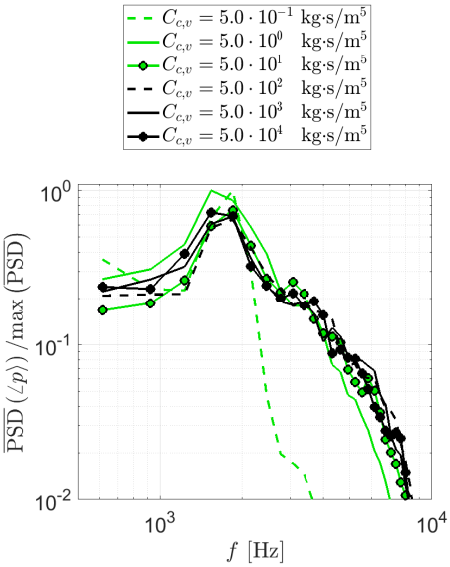

Figure 4.39: Normalized power spectral density distribution of pressure (averaged over the probe locations in Fig. 4.36) for different mass transfer coefficient magnitudes; 15 cells/h_g and $\Delta t = 1.0 \cdot 10^{-7}$ s.

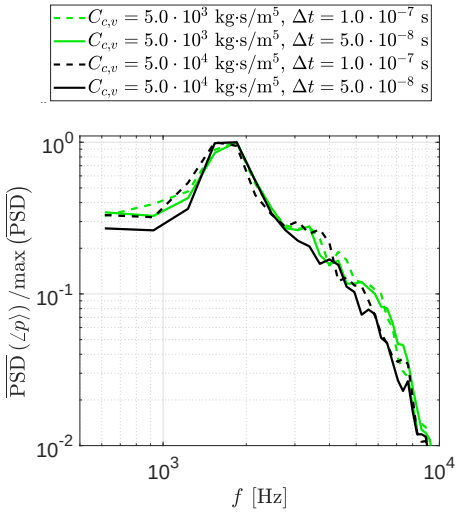

Figure 4.40: Normalized power spectral density distribution of pressure (averaged over the probe locations in Fig. 4.36) for both different time steps and mass transfer coefficient values; 15 cells/h_g.

in the limit $C_{c,v} \to 0$ kg·s/m^5. Compared to the spatial and the temporal resolutions, the value of the mass transfer coefficient $C_c = C_v$ is associated with the smallest uncertainty at $h = 1$.

The convergence of both the characteristic shedding frequency and the time aver-

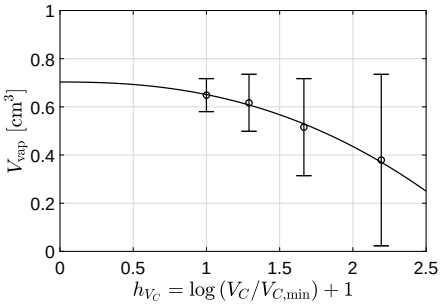

Figure 4.41: Uncertainty of the average vapor volume V_{vap} in the computational domain for a variation of the grid density; $h_{V_C} = 1$ corresponds to the finest grid; $\Delta t = 1.0 \cdot 10^{-7}$ s ($h_{\Delta t} = 1.3$); $C_{c,v} = 5 \cdot 10^3$ kg·s/m^5 ($h_{C_{c,v}} = 2.0$).

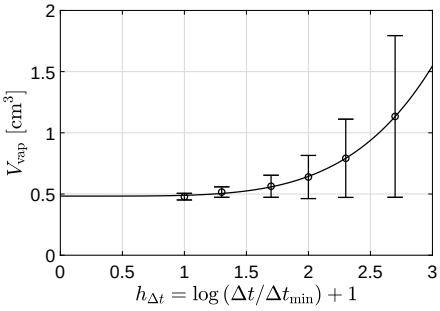

Figure 4.42: Uncertainty of the average vapor volume V_{vap} in the computational domain for a variation of the time step size; $h_{\Delta t} = 1$ corresponds to the smallest time step; 15 cells/h_g ($h_{V_C} = 1.7$); $C_{c,v} = 5 \cdot 10^3$ kg·s/m^5 ($h_{C_{c,v}} = 2.0$).

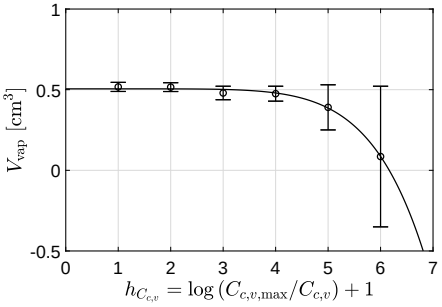

Figure 4.43: Uncertainty of the average vapor volume V_{vap} in the computational domain for a variation of the mass transfer coefficients; $h_{C_{c,v}} = 1$ corresponds to the largest coefficient value; 15 cells/h_g ($h_{V_C} = 1.7$); $\Delta t = 1.0 \cdot 10^{-7}$ s ($h_{\Delta t} = 1.3$).

aged vapor volume content with respect to the investigated parameters is explained by the phase transition behavior of the cavitation model. In order to indicate the flow states during phase transition, Fig. 4.44 depicts the density-pressure trajectory recorded at observation point P_0 indicated in Fig. 4.36. The trajectory is again shown for a systematic variation of grid density, time step size, and mass transfer coefficient values. It can be seen that on statistical average and for fixed Δt and $C_{c,v}$, the evolution of the trajectory is hardly affected by the grid density. The same applies to the variation of the time step size Δt for fixed grid density and $C_{c,v}$ value. On the contrary, the value of the mass transfer coefficient appears to have significant influence on the evolution of the ρ-p trajectory. It is observed that the ρ-p trajectories tend to sway increasingly around the vapor pressure p_v for a decreasing value of $C_{c,v}$. For $C_{c,v} = 50$ kg·s/m^5 and even more for $C_{c,v} = 0.5$ kg·s/m^5, this results in the occurrence of negative pressures as well as unphysically high pressures in the cavitating mixture regime. This behavior is typical for the mass transfer model and can be explained by the proportionality of the observed flow compressibility

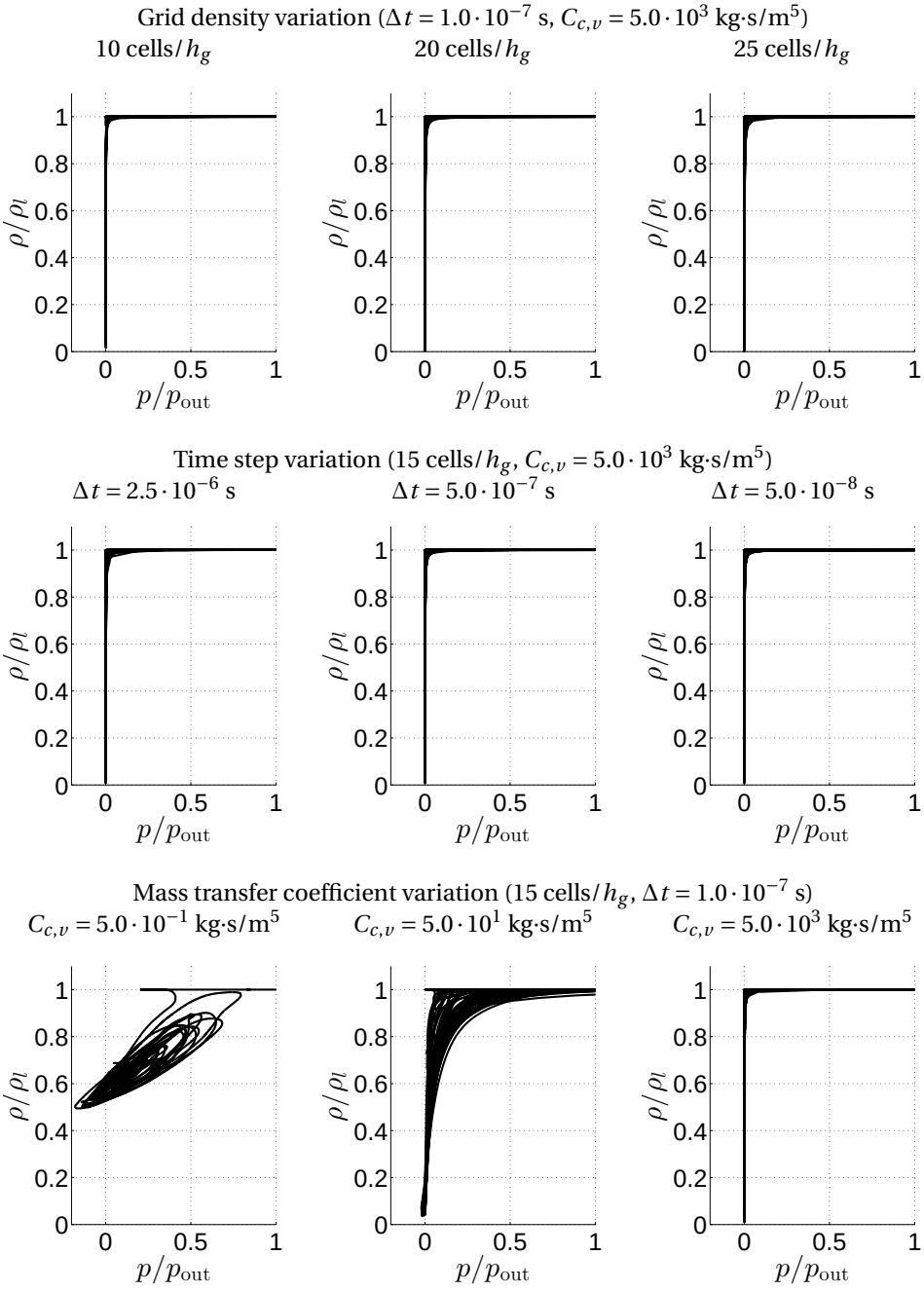

Figure 4.44: Density-pressure trajectories at probe location P_0 in Fig. 4.36 for a variation of the grid density (first row), the time step size (second row) and the mass transfer coefficient value (third row)

$\partial\rho/\partial p$ to the mass transfer coefficient value as discussed in Secs. 2.1.2 and 2.2. These two sections further predict a proportionality of the observed compressibility to $1/\left(\partial p/\partial t\right)$, which suggests that those trajectories evolving at smaller slopes are associated with more rapid temporal pressure changes along the trajectory. In the limit of large values of $C_{c,v}$, the trajectories are kept close to the vapor pressure p_v relative to the pressure difference $p_{\text{out}} - p_v$. Thereby, a scale separation between the driving pressure range and the phase transition pressure range is established, as discussed in Sec. 2.1.3, which makes the inertial flow dynamics insensitive to the exact flow states in the phase transition regime. With the fluid properties and operating conditions given in Table 4.3 and assuming an associated mixture sound speed of $c_m = 2.0$ m/s (see Sec. 2.1.3), the inverse Mach number as defined in Sec. 2.1.3 becomes $\text{Ma}^{-1} = c_m\sqrt{\rho_l/\left(P_{\text{out}} - p_v\right)} = 0.05 << 1$, suggesting that the assumption of an inertia driven flow is physically justified.

Finally, the accumulated surface impact energy distribution obtained from the acoustic model derived in Sec. 3.2 is computed for the same variation of the grid density, time step size, and mass transfer coefficient values. Only the energy focusing approach as specified in Sec. 3.2.2 is employed in the present study. While the simulation time is still 0.013 s, the effective sample time is only 0.010 s, because the moving time averaged pressure $\langle p \rangle$, which is assumed to be equal to the collapse driving pressure p_d in the potential energy balance (see Sec. 3.1.3), requires a build-up time of at least one shedding cycle.

Fig. 4.45 shows the distribution of accumulated surface energy e_S per sample time for the different grid densities. It can be seen that the surface energy distribution per sample time converges with increasing grid resolution. For the coarsest grid (10 cells/h_g), the surface integrated energy content is only half of the one observed for the two finest grids. The finest grid (25 cells/h_g) only results in a slightly higher energy content than the second finest grid (20 cells/h_g). The differences in surface energy content are attributed to the differences in average vapor volume content as found from Fig. 4.41, also having in mind that the frequency at which vapor, and hence potential cavity energy, is periodically generated and reduced, was found to be approximately the same for all grids from Fig. 4.37.

Fig. 4.46 shows the surface energy distributions accumulated per sample time for the time step variation. Convergent behavior of the surface energy distribution with decreasing time step size Δt is observed. It can be seen from the two largest time steps, i.e. $\Delta t = 2.5 \cdot 10^{-6}$ s and $\Delta t = 1.0 \cdot 10^{-6}$ s, that insufficient temporal resolution has two effects. The first effect is an overestimation of the surface energy content relative to the converged distribution. This overestimation is attributed to the overestimation of the average vapor volume in the domain, as is observed in Fig. 4.42. However, the accumulated surface energy content also depends on the rate at which potential energy is periodically increased and reduced and hence on the characteristic shedding frequency. Fig. 4.38 shows a decrease of frequency for large time steps, which counteracts the increase of surface impact energy accumulation resulting from the higher average vapor volume. However, the average vapor volume obtained from the largest time step $\Delta t = 2.5 \cdot 10^{-6}$ s exceeds the vapor volume obtained from the smallest time step by more than a factor of 2, which is more than the relative decrease of the characteristic frequency. The second effect of insufficient temporal resolution is that the distribution of accumulated surface

impact energy stretches significantly further downstream as compared to the converged distributions. As discussed in Sec. 2.3, this effect is explained by the circumstance that the local phase transition process is insufficiently resolved when the time step size is too large, which results in a delayed collapse of the vapor cavities while they are advected downstream by the mean flow.

The convergence behavior of the surface impact energy accumulated per sample time with respect to the mass transfer coefficients $C_{c,v}$ can be seen from Fig. 4.47. For the smallest mass transfer coefficient, i.e. $C_c = C_v = 0.5$ kg·s/m^5, practically no surface energy is visible on the depicted scale. Fig. 4.47 shows that with the convergence of the average vapor volume in the computational domain for increasing values of the mass transfer coefficients (see Fig. 4.43), also the accumulated surface energy converges to a distribution that is independent from the value of the mass transfer coefficient. As Fig. 4.39 shows that the dominating frequency is very similar for all tested values of $C_{c,v}$, the underprediction of surface energy magnitude for small values of $C_{c,v}$ relative to the converged distribution can be fully attributed to the smaller average vapor volume content in the computational domain.

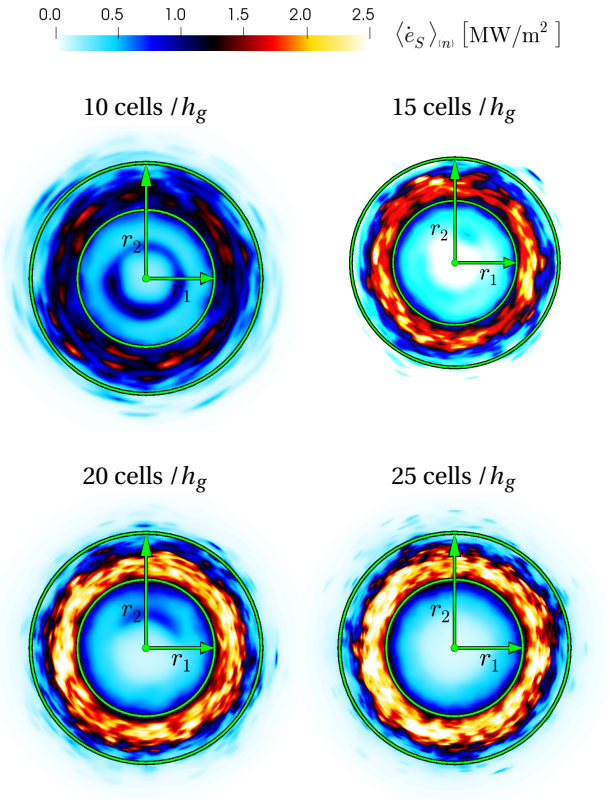

Figure 4.45: Accumulated surface energy distribution per sample time (0.010 s) on the target disc for a systematic variation of the grid density; $\Delta t = 1.0 \cdot 10^{-7}$ s and $C_{c,v} = 5 \cdot 10^3$ kg·s/m^5.

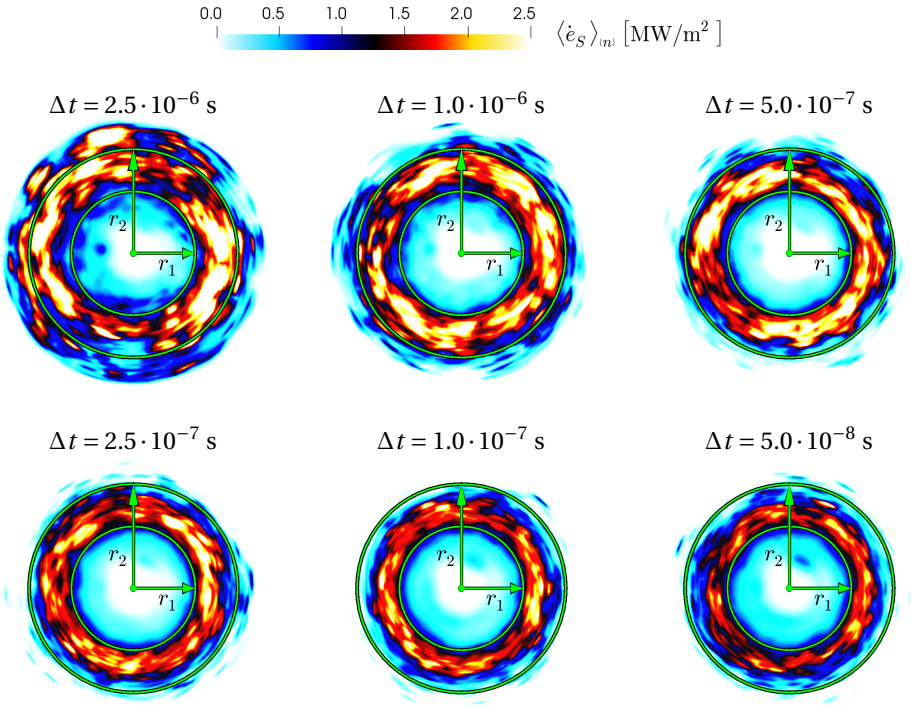

Figure 4.46: Accumulated surface energy distribution per sample time (0.010 s) on the target disc for a systematic variation of the time step size; 15 cells/h_g and $C_{c,v} = 5 \cdot 10^3$ kg·s/m^5.

It is observed that for large mass transfer coefficients and small time steps, most of the surface impact energy accumulates right downstream from the reference position r_1. This is explained by the location of the pressure recovery gradient as indicated by Fig. 4.48, which depicts the time averaged pressure distribution on the target disc after 0.010 s for the second coarsest grid in Table 4.3. On average, a stagnation pressure forms at the center of the disc, where the flow is deflected in radial direction. In the vicinity of the gap entrance, the strong flow acceleration causes a rapid pressure drop, which can be maintained further downstream due to the presence of sheet cavities, in which the pressure must be close to vapor pressure. A region of pronounced pressure recovery approximately starts at the inner reference radius r_1, from which on the most erosive events were observed in the experiment by Franc *et al.* [83]. In addition, Fig. 4.49 shows three instantaneous cross sectional views on the velocity magnitude distribution (left) and the pressure distribution (right), where the left and right images depict the same cross sectional view, but only mirrored with respect to each other. Vapor cavities are indicated by white iso-lines of the liquid fraction $\gamma = 0.0...0.5$. The time instant t_0 shows a larger scale vapor structure that separated from the sheet cavity. At time instants $t_0 + 2$ ms and $t_0 + 4$ ms, developed sheet cavities are observed. In all three situations, the blockage due to the increase of specific volume caused by the presence of vapor cavities in the gap results

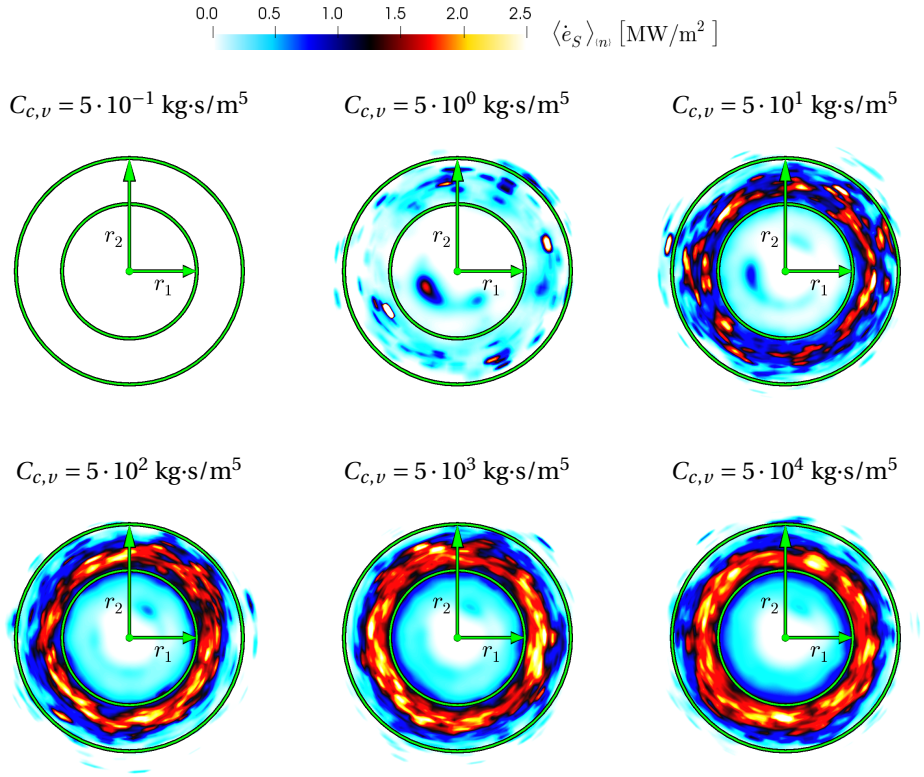

Figure 4.47: Accumulated surface energy distribution per sample time (0.010 s) on the target disc for a systematic variation of the mass transfer coefficient magnitude; 15 cells/h_g and $\Delta t = 1.0 \cdot 10^{-7}$ s.

in an upstream stagnation pressure at the lower disc center that is significantly higher than the exit pressure p_{out}. However, the absolute upstream pressure of 40 bars that is found in the experiments [83], tends to be underpredicted. This may well be explained by the neglecting the viscous forces in the present flow simulation. For a Large Eddy Simulation (LES) without a cavitation model, but otherwise identical operating conditions, Gavaises *et al.* [101] found a pressure drop reduction by 38% as compared to their cavitating flow simulation. This suggests that the viscous pressure drop along the radial direction between the discs makes a significant contribution to the upstream working pressure. Franc *et al.* [83] further estimated the flow velocity along the cavity surface from Bernoulli's equation applied to the liquid phase under the assumption that $p = p_v$ on the cavity surface. Their estimated value of 90 m/s appears the to be well in line with the velocity distribution in Fig. 4.49.

Based on the convergence study of the characteristic shedding frequency, the time averaged vapor content, and the accumulated surface impact energy distribution, it is concluded that the grid resolution is associated with the largest uncertainty for the given variation of input parameters. For this reason, only the finest grid from Table 4.3 is employed for the study. Concerning the temporal resolution, the second smallest time step

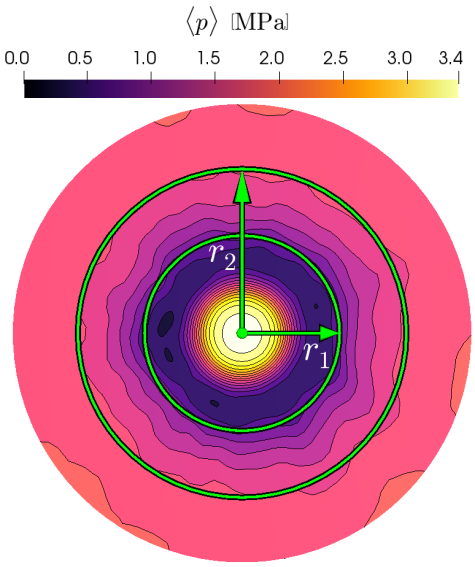

Figure 4.48: Time averaged pressure distribution on the lower disc for 15 cells/h_g, $\Delta t = 1.0 \cdot 10^{-7}$ and $C_{c,v} = 5 \cdot 10^3$ kg·s/m^5 after a sample time of 0.010 s; a pronounced pressure recovery gradient is observed from r_1 onward in downstream direction.

size $\Delta t = 1 \cdot 10^{-7}$ s is considered to provide a sufficiently converged solution. For the mass transfer coefficients $C_{c,v}$, the second largest value $C_c = C_v = 5 \cdot 10^3$ is considered as large enough. From the above mentioned configuration of grid density, time step size, and mass transfer coefficient value, the dominating shedding frequency is determined from a second order polynomial fit through the peak value of the $\overline{\text{PSD}}$ distribution and its two neighbors. The peak location of this interpolation curve gives a dominant shedding frequency of $f_{\text{shedd}} = 1595$ Hz, which is in close agreement with the frequency of 1550 Hz that was found by Mihatsch *et al.* [97]. A comparison with the experimental result by Franc *et al.* [83], which can be found in the work by Mihatsch *et al.* [97], shows that both the numerical results by Mihatsch *et al.* [97] and from the present work slightly underpredict the characteristic shedding frequency found in the experimental data. However, most importantly, the sensitivity study indicates that a converged distribution of the accumulated surface impact energy can be obtained. This surface energy distribution becomes independent of the grid density, the time simulation time step size and the values of the cavitation model coefficients, when converged results for the time averaged amount of vapor volume and the characteristic cavity shedding frequency are achieved. As far as the grid density is concerned, such a convergent behavior is achieved by providing sufficiently high spatial resolution to resolve the growth and decay of the periodic sheet cavity and the larger scale cavitating structures shed from the sheet. Convergence with respect to time step size and mass transfer coefficient magnitude is achieved in the limit of sufficiently small time steps in combination with large values of the mass transfer coefficients. However, in order to avoid numerical inaccuracies due to source term

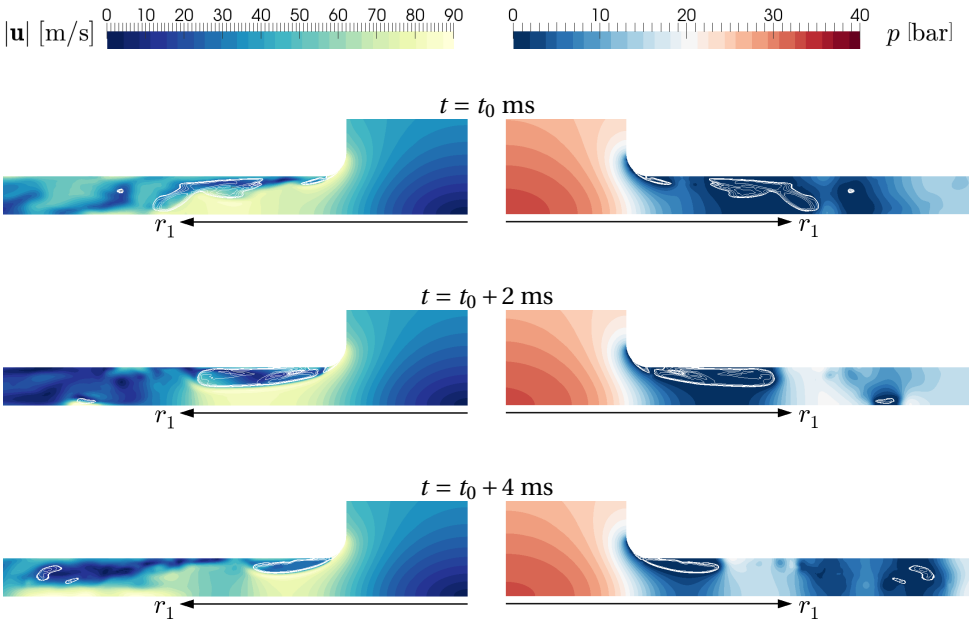

Figure 4.49: Cross-sectional view of the instantaneous velocity magnitude distribution (left) between the horizontal discs and the corresponding instantaneous pressure distribution (right) obtained for 25 cells/h_g, $\Delta t = 1.0 \cdot 10^{-7}$ and $C_{c,v} = 5 \cdot 10^3$ kg·s/m^5; vapor structures are indicated by iso-lines of γ from 0.0 to 0.5; figures on the left and right are mirrored views and depict the same flow situation.

dominance, the mass transfer coefficients should not be chosen exhaustively large, but only as large as necessary to achieve a converged solution. The mass transfer coefficient values are considered sufficiently large when the scale separation between the phase transition or mixture pressure range Δp_m and the driving pressure range $p_\infty - p_v$ as discussed in Sec. 2.1.3 is established. So far, it is checked by visual examination whether the density-pressure trajectories as shown Fig. 4.44 are sufficiently steep relative to the driving pressure range for the scale separation to be established. In future work, a metric should be defined to evaluate the averaged steepness of the trajectories in the phase transition regime relative to the driving pressure range.

4.3.3. IDENTIFICATION OF POTENTIALLY EROSIVE ZONES

The erosive aggressiveness of the flow is investigated by isolating those contributions to the accumulated surface energy distribution that were caused by extreme events. Contributions of extreme events to the distribution $\langle \dot{e}_S \rangle_{\{n\}}$ are identified by means of the statistical analysis method introduced in Sec. 3.4. It is recalled that $n = 1$ represents the unfiltered accumulated surface energy distribution per sample time. For $n > 1$, the contributions caused by low amplitude impacts are attenuated to an extent governed by the value of n in such a way that the filtered distribution satisfies $\langle \dot{e}_S \rangle_{\{n>1\}}\big|_{\mathbf{x}_S} \leq \langle \dot{e}_S \rangle_{\{n=1\}}\big|_{\mathbf{x}_S}$ at any surface location $\mathbf{x}_S$. The intensity exponent is chosen to be $n = 2$. This value was shown to strongly attenuate the lower amplitudes in Sec. 4.2.5. The source term projec-

tion frequency is $1/T_p = 1000$ Hz, which is equal to the frequency $1/T_{\text{mov}}$ of the moving averaged pressure field to compute the driving pressure distribution. Fig. 4.50 shows a comparison between the unfiltered surface energy distribution per sample time (left) and the corresponding filtered distribution (right) after a sample time of 0.010 s. Two differences between the two are observed from the raw data distributions depicted at the top of the figure. First, the filtered distribution ($n = 2$) appears to be more scattered than the unfiltered one ($n = 1$). This is the result of attenuating the low amplitude impact contributions, such that the less frequent and more scattered extreme events appear more prominently. Second, the filtered distribution is more concentrated in radial direction, and it also appears to have a slight shift downstream along the radial direction relative to the unfiltered distribution. This downstream shift becomes even more visible in the circumferential averages of the two distributions, which are depicted at the bottom of Fig. 4.50. The shift is explained by the radial pressure recovery. With increasing radial distance r from the disc center, cavities are more and more unlikely to be present, but if they are, they can collapse more violently due to their larger potential energy content. These rather rare but high amplitude implosions become more prominent in the filtered surface energy distribution, whereas the more frequent upstream events can more efficiently accumulate in the unfiltered distribution.

For further comparison, the filtered surface energy distribution ($n = 2$), associated with the distribution of the most aggressive impact loads, is compared to the experimental erosion damage pattern by Franc *et al.* [83] and several numerical results from literature. The corresponding results are depicted in Fig. 4.51. For reference, the $\langle \dot{e}_S \rangle_{\{n=2\}}$ distributions from Fig. 4.50 are shown at the top, with the circumferential averaged distribution on the left (A) and the raw data distribution on the right (B). The experimental erosion damage pattern obtained by Franc *et al.* [83] is depicted in sub-figure C. Sub-figure D is found in the work by Peters *et al.* [98], who used an unsteady Reynolds-averaged Navier-Stokes (URaNS) approach and a mass transfer approach with incompressible liquid phase to model the cavitating flow. The left half of sub-figure D shows the distribution of a deformation coefficient derived by Peters *et al.* [98]. The deformation coefficient is based on a liquid micro-jet model by Dular and Coutier-Delgosha [10], where the distribution of water hammer pressure impacts above a critical threshold level occurring on the sub-grid level is estimated from the macroscopic local flow conditions provided by the numerical simulation. Sub-figures E and F are taken from the work by Mihatsch *et al.* [97], who developed a collapse detector methodology to identify high erosion risk areas. Sub-figure E shows the distribution of near-wall (distance < 0.5 mm) collapse pressures in the computational domain. The distribution of maximum surface pressures obtained from the simulation is depicted by sub-figure F. The results by Mihatsch *et al.* [97] are obtained from a fully compressible density-based approach to model the cavitating flow.

The comparison shows all numerically obtained impact distributions to be in satisfactory qualitative agreement with the experimental erosion pattern. A quantitative comparison is not possible, because the metrics used by the different authors are very different. The deformation coefficient by Peters *et al.* [98] is dimensionless per definition. Even though the impact load model applied in the present work is based on the spherical propagation of energy radiation sources, the obtained impact distribution can-

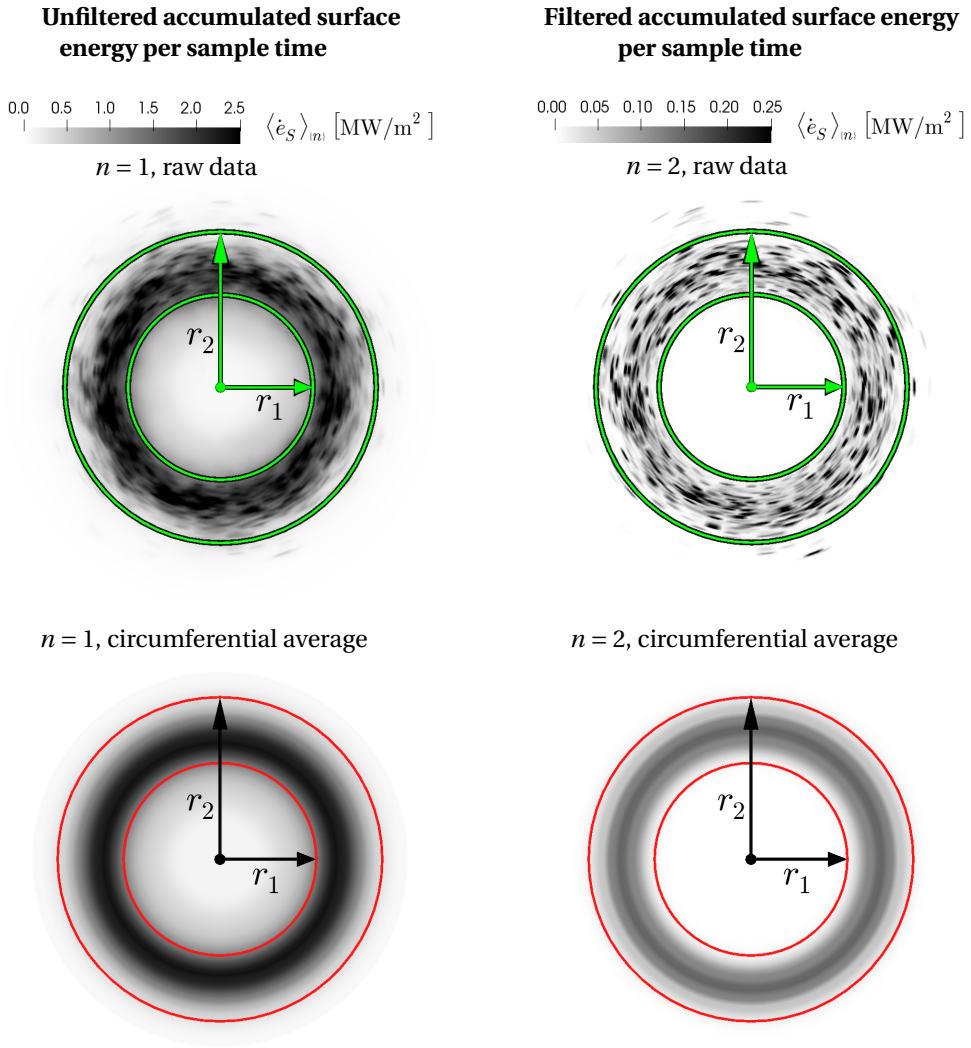

Figure 4.50: Distribution of the accumulated surface energy per sample time, where $n = 1$ represents the unfiltered distribution (left), whereas for $n = 2$ (right), the low impact amplitudes have been attenuated according to the extreme event filtering technique introduced in Sec. 3.4.

not directly be compared to the collapse pressures and surface pressure lofads reported by Mihatsch *et al.* [97]. The essential difference is that the fully compressible approach by Mihatsch *et al.* [97] allows to directly compute the pressure rise at the cavity collapse center and the subsequent propagation of the pressure wave impacting the surface. In the present work, the transport equation of collapse induced kinetic energy allows to compute the energy content of the radiated shock wave, which is then projected on the impacted surface in a discrete event. Therefore, the model can give a reliable estimate

of the time integrated impact power and acoustic pressure, but not a time accurate solution of the instantaneous acoustic power and pressure. The exact temporal evolution of the impact power signals would require an additional assumption in the modeling about the impact duration of the individual events.

The capability of a cavitation erosion model to allow for quantitative erosion risk predictions strongly depends on its capability to provide physically converged solutions of the surface impact distribution for different grid densities, time step sizes, and possibly other flow model parameters. For the fully compressible density-based numerical approach employed by Mihatsch *et al.* [97], it was shown by Schmidt *et al.* [17] that the maximum local pressure of a collapse scales with the inverse of the characteristic cell length. As a result, the obtained pressure decreases with the linear decay law of spherical waves [17]. In order to compensate for this grid density effect, Mihatsch *et al.* [97] scale the local collapse pressure with a non-dimensionalized characteristic cell length. The surface pressure obtained from the fully compressible density-based approach was shown to be independent of the grid size even without correction [17], given that the distance from the collapse center to the impacted wall, hence, the spherical wave propagation is resolved. The linear decay law, as referred to by Mihatsch *et al.* [97], is also found back in the reconstructed acoustic pressure given by Eqn. (3.51), if only a single radiation source is considered, such that $p_a(t,\mathbf{x}_S) \sim \sqrt{\dot{e}_{\mathrm{rad}}}/\|\mathbf{x}_P - \mathbf{x}_S\|$. Even though the modeling approach in the present work is conceptually very different from the erosion risk assessment procedure, as proposed by Mihatsch *et al.* [97] in the context of fully compressible flow simulations, the underlying mechanism to achieve grid independence is very similar. By focusing the potential energy of a collapsing cavity into the collapse center, the resolution of the focusing process is still limited by the characteristic cell size. However, as the focused energy content in the limiting grid cells is tracked down from the volume change of the imploding structures, it can be conserved across the spherical front of the radiated shock wave. This makes the present model inherently energy conserving, provided that the volume change, and therefore the change of potential energy of the resolved cavitating structures, is accurately captured. A best possible numerical reconstruction of the local velocity divergence plays a key role when an accurate reconstruction of the potential energy change, according to Eqns. (3.29) and (3.30), is the principal aim.

A) See Fig. 4.50, $n = 2$, circumf. average

B) See Fig. 4.50, $n = 2$, raw data

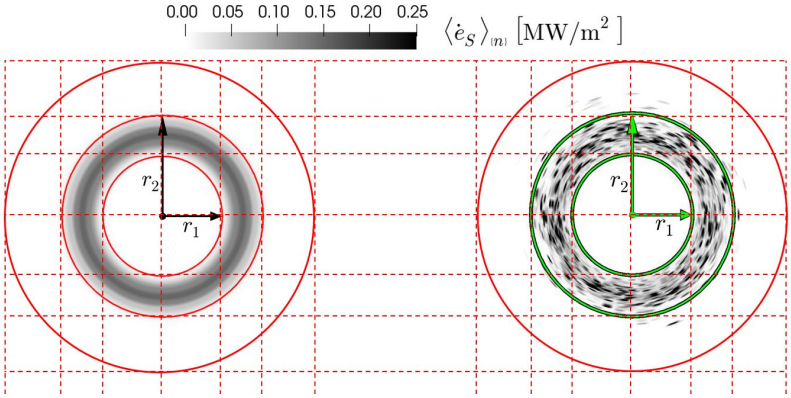

C) Erosion pattern from the experiment by Franc *et al.* [83], image taken from [97]

D) Distribution of the deformation coefficient c_{def} in the work by Peters *et al.* [98]

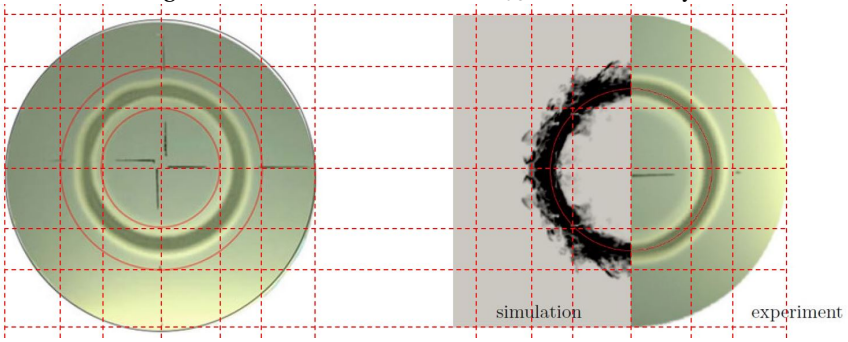

E) Detected collapse pressures scaled with the linear decay law for spherical waves [97], figure taken from Mihatsch *et al.* [97]

F) Maximum surface pressure distribution, figure taken from Mihatsch *et al.* [97]

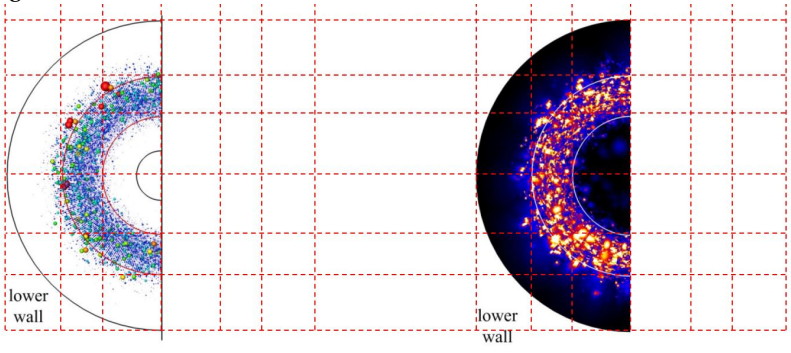

Figure 4.51: Qualitative comparison of the high amplitude impact load distribution computed in the present work (A, B) with the experimentally obtained erosion pattern [83] (C), the deformation coefficient distribution by Peters *et al.* [98] (D), and the collapse pressures by Mihatsch *et al.* [97] (E, F).

4.3.4. DISCUSSION OF THE RESULTS

A recently developed cavitation implosion load model based on a model transport equation to describe the collapse energy cascade is applied to the cavitating flow in an axisymmetric nozzle. The accumulated surface energy distribution on the erosion target disc obtained from the implosion load model is in satisfactory agreement with the damage pattern observed in an experiment by Franc *et al.* [83]. This particularly applies to the distribution of extreme impact events. The impact energy distribution is further compared to other numerical results reported in literature. Even though the erosion risk metrics of the presented results are fundamentally different from each other, they all yield good qualitative agreement with the experimentally observed damage pattern. In this case it may be attributed to the high operating pressure and the pronounced pressure recovery gradient, which forces the shed cavitites to collapse in a very confined area on the target disc.

The main added value of the present study is to demonstrate that the recently developed implosion load model is able to give numerically converged results in agreement with physical properties for the impact energy distribution. This means that the surface energy distribution accumulated per sample time becomes independent of the grid density, the simulation time step, and the mass transfer coefficient magnitude of the cavitation model. Grid size independence of the accumulated surface energy distribution is an integral part of the modeling approach. The prerequisite to achieve grid size independence is that the large-scale cavitating structures, which can be assumed to include most of the potential energy, are reasonably well resolved. More specifically, the average volume of the separated vapor structures imploding on the target surface needs to be captured, without the necessity to capture the detailed break-up of those structures into small-scale structures. The conversion of the potential energy content into surface impact energy is strictly governed by the transport equation of the energy cascade and the spherical wave propagation law. By this means, the energy content radiated from the cavity collapses is not derived from local instantaneous quantities such as pressure, but rather from the history of the cavity collapse, which again is reliably predicted by the numerical flow solver. Next to the minimum spatial resolution that is needed to resolve the large-scale cavitating structures, the temporal resolution and the mass transfer coefficient magnitude play an important role to obtain a converged solution for the characteristic shedding frequency of these structures. It is shown that a converged shedding frequency is obtained in the limit of large mass transfer coefficients in combination with sufficiently small time steps.

5

CONCLUSION

5.1. SUMMARY OF THE RESEARCH FINDINGS

A novel model transport equation describing the energy cascade involved in vapor cavity collapses has been proposed in this research. The design of this transport equation is strongly driven by the capability of engineering flow simulation tools to predict flow quantities that can be linked to the erosive aggressiveness of the cavitating flow. To this end, the present research has two goals. The first goal is an improved understanding of the capabilities and limitations of engineering flow solvers to predict cavitation implosion loads. It has been found that the kinematic features of the cavitating flow, e.g. cavity collapse times and characteristic cavity shedding frequencies, are reliably predicted if the cavitating flow can be classified as predominantly inertia driven. Based on the improved understanding of the flow solver capabilities and limitations, the second goal is the development of a cavitation implosion load model that allows for quantitative predictions of cavitation implosion loads.

5.1.1. FINDINGS ABOUT CAVITATING FLOW DYNAMICS

Flow solvers labeled as "engineering tools" in the context of this work have two main features that distinguish them from physically more correct but also computationally more expensive flow simulation tools. First, the pure liquid phase is treated as incompressible. This means that implosion impacts are not the result of propagating waves, but the result of instantaneous pressure pulses associated with an infinite propagation speed. Second, the cavitation model is a (semi-) empirical mass transfer source term, whereas high fidelity models would rather explicitly enforce the thermodynamic equilibrium states of the macroscopic mixture fluid.

As discussed in Sec. 2.1.2, the mass transfer rate to support unique equilibrium states of the cavitating mixture can be derived from the constraint that the apparent compressibility of the mixture fluid must be invariant with respect to the observer's reference frame. In engineering mass transfer models, the violation of this equilibrium constraint is accepted for the sake of numerical robustness and computational efficiency. However,

these models can be tuned by means of mass transfer coefficients. In the limit of large coefficient values, a scale separation is enforced between the phase transition pressure range and the pressure range driving the collapse of vapor cavities. As a result of this scale separation, the flow dynamics get insensitive to the exact flow states of the cavitating mixture. The inverse Mach number Ma^{-1} is proposed in Sec. 2.1.3 to check whether the flow can be classified as predominantly inertia driven and whether the enforced scale separation is physically justified. This is the case if $Ma^{-1} << 1$, which typically applies to flow situations encountered in engineering problems. In the limit of large mass transfer coefficients and with sufficient temporal resolution, the mass transfer model has enough capacity to achieve the local phase transition within the time scale that is dictated by the inertia driven flow. Thereby, the mass transfer model can mimic the mixture compressibility behavior of high fidelity equilibrium models in the sense that the inertial flow dynamics are not affected by the violation of the equilibrium constraint. In Secs. 2.3.2 and 4.1.2, it has been shown how the collapse time of an isolated bubble and of a collective bubble cloud, respectively, converges in the limit of large mass transfer coefficients and sufficiently small time steps. With the same procedure, the convergence of the characteristic shedding frequency and the averaged vapor volume content has been demonstrated for a re-entrant jet dominated flow in Sec. 4.3.2. In order to avoid numerical inaccuracies and instabilities due to source term dominance of the governing equations, the mass transfer coefficients should be chosen as large as necessary to achieve physical convergence, but not excessively large. A practical way to check whether the coefficients are large enough, without the need to perform exhaustive sensitivity studies, is to sample a density-pressure trajectory at a location of high evaporation rate and possibly at another location at which rapid condensation processes are expected. If the observed trajectories remain close to vapor pressure during evaporation and if their evolution is steep relative to the range between vapor and ambient pressure during condensation, the coefficients can be considered as large enough. The error that is introduced by the infinite propagation speed of a pressure pulse in an incompressible liquid can typically be considered as negligible, because the time that it would take for a sound wave to propagate through the flow region of interest at liquid sound speed is typically much smaller than the advective time scale of the flow. However, one cannot expect reliable results for the implosion peak pressures if the liquid is treated as incompressible.

5.1.2. MODELING CAVITATION IMPLOSION LOADS

The findings about the flow solver capabilities have led to the conclusion that a cavitation implosion load model is needed and that it should be based on kinematic features of the cavitating flow. Furthermore, the computation of implosion loads should not exclusively be based on instantaneous local flow quantities, as they are inaccurately predicted at the final cavity collapse stage. With this in mind, the potential energy concept has been considered as a suitable starting point for the design of the cavitation implosion load model, because it provides "a priori" information about the energy content of a cavity which can eventually feed into the radiated shock wave. The task is then to track the collapse energy throughout the cavity collapse, the radiation of the collapse shock wave, its spherical propagation and eventually the impact on the solid surface. The main difficulty in deriving a model transport equation describing this process is that a conversion

of different energy forms takes place. This energy conversion is also referred to as the energy cascade of the cavity collapse [19, 21, 24].

Prior to the final collapse stage, the energy cascade involves the conversion of potential cavity energy into kinetic energy of the surrounding liquid [13, 32]. In complex flow situations, the spatial distribution of kinetic energy induced by a cavity collapse is unknown. The total amount of kinetic energy induced by the collapse, however, can be derived from its change of potential energy [13, 32]. For the simplifying situation of an isolated bubble collapse, it has further been shown in Sec. 3.1.1 that the collapse induced kinetic energy distribution focuses towards the cavity interface and thereby into the collapse center as the final collapse stage is approached. Together with the knowledge of the instantaneous rate of kinetic energy generation induced by the cavity, this focusing effect is utilized in the novel transport equation by artificially absorbing the collapse induced kinetic energy into the cavity interface. Thereby, the absorbed energy is focused towards the collapse center and converted into radiated energy when a final collapse stage is identified. The conservative transport along the collapsing interface is achieved by destroying kinetic energy right upstream from the interface and by absorbing the same amount into the interface and at a rate that is proportional to the local rate of potential energy reduction. Together with the criterion to identify the final collapse stage, this integral balance allows for a redistribution of absorbed kinetic energy between interacting cavities in a collective collapse situation as described by Wang and Brennen [16] . Compared to related approaches by Arabnejad and Bensow [25] and Leclercq *et al.* [27], the capability to capture the collective collapse of interacting cavities can be seen as the most distinct physical feature of the present modeling approach. The surface impact power is calculated from the spherical wave propagation law. Similar to the approach by Leclercq *et al.* [27] and different from almost any other related technique, the local surface orientation relative to the radiation source is taken into account to fully comply with the energy conservation requirement.

The computational efficiency of the approach can be problematic because each radiation source must be propagated onto the entire target surface. In other words, each local surface impact is the result of a volume integral over all radiation sources. This efficiency problem has been solved by integrating the energy radiation field over time and by propagating the accumulated radiation energy at the end of specified time intervals only. This can be done because the energy propagation from the radiation source to the impacted surface only involves geometrical information. If the temporal evolution of an impact signal is needed, it is recommended to restrict the analysis to a few probe locations of interest. Furthermore, a statistical analysis method has been developed to identify extreme impact events by attenuating low amplitude events in the surface energy distribution. By this means, one can distinguish between locations that are impacted frequently but at rather low amplitudes and locations that are subject to few isolated extreme events.

5.1.3. APPLICATION OF THE IMPLOSION LOAD MODEL

The cavitation implosion load model has been applied to three test cases, each focusing on different aspects of the model. The first test case in Sec. 4.1 involved the close wall collapse of a vapor bubble cloud. It has been demonstrated with this test case, that the

model is able to automatically distinguish between isolated and collective collapse situations. In Sec. 4.1.3, the model has been shown to capture the collective energy transport along the low pressure side of an inward directed condensation shock as described by Wang and Brennen [16]. To further demonstrate the effect of energy focusing, the results obtained from the transport equation of collapse induced kinetic energy (energy focusing approach) have been compared to an alternative approach similar to Leclercq *et al.* [27] in which the change of potential energy is assumed to directly feed into radiated power (non-focusing approach) instead of being converted into kinetic energy prior to the final collapse stage. In fact, the majority of cavitation erosion models based on the potential energy concept follows the latter assumption. The impact signals have been shown to be fundamentally different for the two approaches. Only with the kinetic energy focusing approach, the reconstructed acoustic wall impact pressure could mimic the impact pressure signal obtained by Schmidt *et al.* [17] from a fully compressible density-based simulation. In the second test case in Sec. 4.2, the cavitating flow around a NACA0015 hydrofoil has been investigated, mainly to test the statistical analysis method to identify extreme impact events. Best practice guidelines for the use of the developed methodology to assess the aggressiveness of periodic cavitating flows have been derived and summarized in Sec. 4.2.7. With the third test case, involving the cavitating flow in an axisymmetric nozzle, it has been demonstrated that the surface impact energy distribution accumulated per sample time converges if the averaged vapor volume content in the computational domain and the characteristic cavity shedding frequency converges. This can be seen as a step towards quantitative predictions of cavitation erosion damage.

5.2. OUTLOOK

Some aspects of the presented modeling approach need further improvement, so that the computed cavitation implosion impact loads can reliably be coupled to material models. This will allow to make quantitative predictions of cavitation erosion damage in future work.

The collapse driving pressure has turned out to be the most difficult quantity to model in the present modeling framework. The reason is that the collapsing driving pressure is a non-uniform and unsteady ambient condition rather than a material quantity. For periodic cavitating flows as typically encountered in engineering problems, the moving time averaged pressure is proposed as an approximation of the collapse driving pressure (see Sec. 3.1.3). From a systematic variation of the moving average time window in Sec. 4.2.4, it is concluded that the length of the moving time window should be equal to the characteristic cavity shedding period or larger. Even though this approach allows to capture the effect of pressure recovery gradients on statistical average, an improved model for the driving pressure with stronger physical foundation would be desirable.

The conservation of energy throughout the collapse energy cascade is a key factor when reliable quantitative predictions of the energy distribution on the impacted surface are aimed for. The transport equation to describe the focusing and radiation of collapse energy is given Eqn. (3.28) and by Eqn. (3.40) in its final form, and the spherical wave propagation and surface projection of the radiated energy is given by Eqn. (3.44). The transport term $\phi(\mathscr{E})$ and the radiation source term as well as the spherical wave propagation and surface projection operator are formulated in such a way

that energy conservation is strictly enforced. The term $\left(De_{\text{pot}}/Dt\right)_c$ measuring the local change of potential energy, however, can be subject to inaccuracies due to numerical errors involved in the reconstruction of the velocity divergence field (see Eqns. (3.29) and (3.30)). For this reason, the numerical technique to reconstruct the velocity divergence needs further investigations. In recent research, Melissaris *et al.* [68] have found a way to achieve exact energy conservation under two prerequisites. First, the velocity divergence at the cell center should be reconstructed from the cavitation model source term Γ [68] such that $(\nabla\cdot\mathbf{u})_C = \Gamma_C$ and not from the sum of the face fluxes given by $(\nabla\cdot\mathbf{u})_C = 1/V_C\sum_f \mathbf{u}_f\cdot\mathbf{S}_f$ as it has been done in the present work. Even though both formulations should be equal because of the definition $\nabla\cdot\mathbf{u}=\Gamma$, they do not necessarily give the same result in practice due to interpolation and iterative errors in the numerical scheme [106]. Second, higher order time discretization schemes help to further minimize the numerical errors involved in the reconstruction of $\nabla\cdot\mathbf{u}$ [68].

In the present form, the impact signals computed from the cavitation implosion model are not time accurate because the radiation source and the spherical wave propagation and surface projection operator can only control the energy content in the spherical wave front, but not the exact energy density distribution across the wave front. Also, the wave propagation speed is assumed to be infinite. An additional modeling assumption is needed to make the computed impact signal time accurate. The additional model term could comprise an assumption about the wave passage time and an energy density distribution function across the wave front. With the knowledge of both, the energy radiation could be modeled in a time accurate fashion rather than as a discrete event as it happens in the present form. Patella *et al.* [34] have found a linear relation between the wave passage time and the initial radius of a collapsing vapor/gas bubble. Knowing the amount of energy that is focused into the collapse collapse, an equivalent initial radius could be computed in the present modeling approach to finally obtain the wave passage time. Analogous to the propagation of acoustic sources in the acoustic analogy by Lighthill and Newman [107] and by Williams *et al.* [108], a time retardation could be introduced to account for the wave travel time from the source to the impact location. Furthermore, Tinguely *et al.* [14] formulated the collapse energy partition of an isolated vapor/gas bubble as a function of a single parameter that involves the driving pressure difference and also the pressure of non-condensable gas. When either the amount of non-condensable gas is high or the driving pressure is low so that the amount of energy feeding into a rebound bubble is not negligible, the energy partition by Tinguely *et al.* [14] could be employed in the present modeling approach.

Finally, the transport terms $\{\phi\}^+$ and $\{\phi\}^-$ in the transport equation of collapse induced kinetic energy are subject to modeling assumptions discussed in Sec. 3.2.1 in order to achieve the transport of absorbed kinetic energy along the collapsing cavity interfaces as well as the non-trivial energy redistribution between interacting cavities. Even though the validity of these modeling assumptions is supported by the numerical test cases in the present work, more testing is recommended to further validate them against results from literature.

REFERENCES

[1] S. Schenke, T. Melissaris, and T. J. C. van Terwisga, *On the relevance of kinematics for cavitation implosion loads,* Physics of Fluids **31**, 052102 (2019).

[2] S. Schenke and T. J. C. van Terwisga, *An energy conservative method to predict the erosive aggressiveness of collapsing cavitating structures and cavitating flows from numerical simulations,* International Journal of Multiphase Flow **111**, 200 (2019).

[3] K. Johansen, J. H. Song, K. Johnston, and P. Prentice, *Deconvolution of acoustically detected bubble-collapse shock waves,* Ultrasonics **73**, 144 (2017), received funding from the European Research Council under the European Union's Seventh Framework Programme (FP/2007 – 2013)/ERC Grant Agreement no. 336189 (TheraCav).

[4] A. Vogel, W. Lauterborn, and R. Timm, *Optical and acoustic investigations of the dynamics of laser-produced cavitation bubbles near a solid boundary,* Journal of Fluid Mechanics **206**, 299 (1989).

[5] M. S. Plesset and R. B. Chapman, *Collapse of an initially spherical vapour cavity in the neighbourhood of a solid boundary,* Journal of Fluid Mechanics **47**, 283 (1971).

[6] M. Dular, B. Stoffel, and B. Širok, *Development of a cavitation erosion model,* Wear **261**, 642 (2006).

[7] P. A. Lush, *Impact of a liquid mass on a perfectly plastic solid,* Journal of Fluid Mechanics **135**, 373 (1983).

[8] J. R. Blake and D. C. Gibson, *Cavitation bubbles near boundaries,* Annual Review of Fluid Mechanics **19**, 99 (1987).

[9] G. L. Chahine, *Advanced Experimental and Numerical Techniques for Cavitation Erosion Prediction*, edited by G. Chahine, K.-H. Kim, J.-P. Franc, and A. Karimi, Vol. 106 (2014) Chap. 6, pp. 123–161.

[10] M. Dular and O. Coutier-Delgosha, *Numerical modelling of cavitation erosion,* International Journal for Numerical Methods in Fluids **61**, 1388 (2009).

[11] F. G. Hammitt, *Observations on cavitation damage in a flowing system,* Journal of Basic Engineering **85**, 347 (1963).

[12] A. Vogel and W. Lauterborn, *Acoustic transient generation by laser-produced cavitation bubbles near solid boundaries,* Journal of The Acoustical Society of America **84**, 719 (1988).

[13] D. Obreschkow, P. Kobel, N. Dorsaz, A. de Bosset, C. Nicollier, and M. Farhat, *Cavitation bubble dynamics inside liquid drops in microgravity,* Phys. Rev. Lett. **97**, 094502 (2006).

[14] M. Tinguely, D. Obreschkow, P. Kobel, N. Dorsaz, A. de Bosset, and M. Farhat, *Energy partition at the collapse of spherical cavitation bubbles,* Phys. Rev. E **86**, 046315 (2012).

[15] R. H. Cole, *Underwater explosions* (Princeton, Princeton Univ. Press, 1948).

[16] Y.-C. Wang and C. Brennen, *Numerical computation of shock waves in a spherical cloud of cavitation bubbles,* Journal of Fluids Engineering **121** (1999), 10.1115/1.2823549.

[17] S. J. Schmidt, M. Mihatsch, M. Thalhamer, and N. A. Adams, *Advanced Experimental and Numerical Techniques for Cavitation Erosion Prediction*, edited by G. Chahine, K.-H. Kim, J.-P. Franc, and A. Karimi, Vol. 106 (2014) Chap. 14, pp. 329–344.

[18] D. Ogloblina, S. J. Schmidt, and N. A. Adams, *Numerical Simulation of Collapsing Vapor Bubble Clusters Close to a Rigid Wall,* in *Proceedings of the 10th International Symposium on Cavitation (CAV2018)* (ASME Press, 2018) https://asmedigitalcollection.asme.org//chapter-pdf/3823165/861851_ch149.pdf .

[19] F. Pereira, F. Avellan, and P. Dupont, *Prediction of cavitation erosion: An energy approach,* Journal of Fluids Engineering **120**, 719 (1998).

[20] R. F. Patella and J.-L. Reboud, *A new approach to evaluate the cavitation erosion power,* Journal of Fluids Engineering **120**, 335 (1998).

[21] R. F. Patella, J.-L. Reboud, and L. Briançon-Marjollet, *A phenomenological and numerical model for scaling the flow agressiveness in cavitation erosion,* in *Cavitation Erosion EROCAV Workshop. Val de Reuil, France* (2004).

[22] H. Kato, A. Konno, M. Maeda, and H. Yamaguchi, *Possibility of quantitative prediction of cavitation erosion without model test,* Journal of Fluids Engineering **118** (1996).

[23] M. S. Mihatsch, S. J. Schmidt, and N. A. Adams, *Cavitation erosion prediction based on analysis of flow dynamics and impact load spectra,* Physics of Fluids **27**, 103302 (2015).

[24] G. Bark, N. Berchiche, and M. Grekula, *Application of principles for observation and analysis of eroding cavitation, EROCAV observation handbook*, 3rd ed. (Department of Shipping and Marine Technology, Chalmers University of Technology, Sweden, 2004).

[25] M. H. Arabnejad and R. Bensow, *A methodology to identify erosive collapse events in the incompressible simulation of cavitating flows,* in *Proceedings of the 20th Numerical Towing Tank Symposium* (Wageningen, the Netherlands, 2017).

[26] R. F. Patella, A. Archer, and C. Flageul, *Numerical and experimental investigations on cavitation erosion,* IOP Conference Series: Earth and Environmental Science **15**, 022013 (2012).

[27] C. Leclercq, A. Archer, R. F. Patella, and F. Cerru, *Numerical cavitation intensity on a hydrofoil for 3d homogeneous unsteady viscous flows,* International Journal of Fluid Machinery and Systems **10**, 254 (2017).

[28] M. Nohmi, T. Ikohagi, and Y. Iga, *Numerical prediction method of cavitation erosion,* in *2008 Proceedings of the ASME Fluids Engineering Division Summer Conference, FEDSM 2008*, Vol. 1 (2008).

[29] Z. Li, M. Pourquie, and T. J. C. van Terwisga, *Assessment of cavitation erosion with a urans method,* Journal of Fluids Engineering **136**, 041101 (2014).

[30] S. Joshi, J. P. Franc, G. Ghigliotti, and M. Fivel, *Sph modelling of a cavitation bubble collapse near an elasto-visco-plastic material,* Journal of the Mechanics and Physics of Solids **125**, 420 (2019).

[31] U. Rasthofer, F. Wermelinger, P. Karnakov, J. Šukys, and P. Koumoutsakos, *Computational study of the collapse of a cloud with 12 500 gas bubbles in a liquid,* Physical Review Fluids **4** (2019), 10.1103/PhysRevFluids.4.063602.

[32] B. B. Mikic, W. M. Rohsenow, and P. Griffith, *On bubble growth rates,* International Journal of Heat and Mass Transfer **13**, 657 (1970).

[33] L. Rayleigh, *Viii. on the pressure developed in a liquid during the collapse of a spherical cavity,* The London, Edinburgh, and Dublin Philosophical Magazine and Journal of Science **34**, 94 (1917).

[34] R. F. Patella, G. Challier, J.-L. Reboud, and A. Archer, *Energy balance in cavitation erosion: From bubble collapse to indentation of material surface,* Journal of Fluids Engineering **135**, 011303 (2013).

[35] W. G. Vincenti and J. C. H. Kruger, *Introduction to Physical Gas Dynamics* (John Wiley & Sons, 1965).

[36] R. Saurel, P. Cocchi, and P. B. Butler, *Numerical study of cavitation in the wake of a hypervelocity underwater projectile,* J. Propul. Power **15**, 513–522 (1999).

[37] P. G. Tait, *Report on some of the physical properties of fresh water and sea water,* Phys. Chem. **2**, 1 (1888).

[38] S. J. Schmidt, *A low Mach number consistent compressible approach for simulation of cavitating flows*, Ph.D. thesis, Technische Universiät München (2015).

[39] N. Kyriazis, P. Koukouvinis, M. Gavaises, R. J. Pearson, and M. R. Gold, *Heating effects during bubble collapse using tabulated data,* in *Proceedings of the 10th International Symposium on Cavitation* (Baltimore, Maryland, USA, 2018).

[40] I. H. Sezal, *Compressible dynamics of cavitating 3-D multi-phase flows,* Ph.D. thesis, Technische Universiät München (2009).

[41] C. E. S., Hickel, S. Schmidt, and N. Adams, *Large-eddy simulation of turbulent cavitating flow in a micro channel,* Physics of Fluids **26** (2014), 10.1063/1.4891325.

[42] B. Budich, S. J. Schmidt, and N. A. Adams, *Numerical simulation and analysis of condensation shocks in cavitating flow,* Journal of Fluid Mechanics **838**, 759–813 (2018).

[43] Y. Delannoy and I. E. Kueny, *Two phase flow approach in unsteady cavitation 'modelling,* Cavitation and Multiphase Flow Forum, ASMEFED **98**, 153 (1990).

[44] D. van der Heul, C. Vuik, , and P. Wesseling, *Efficient computation of flow with cavitation by compressible pressure correction,* in *ECCOMAS* (Barcelona, Spain, 2000).

[45] A. H. Koop, H. W. M. Hoeijkmakers, G. H. Schnerr, and E. J. Foeth, *Design of twisted cavitating hydrofoil using a barotropic flow method,* Proceedings of the 6th International Symposium on Cavitation (2006).

[46] E.-J. Foeth, *The structure of three-dimensional sheet cavitation,* Ph.D. thesis, Delft University of Technology (2008).

[47] R. F. Kunz, D. A. Boger, D. R. Stinebring, T. S. Chyczewski, J. W. Lindau, H. J. Gibeling, S. Venkateswaran, and T. R. Govindan, *A preconditioned navier-stokes method for two-phase flows with application to cavitation prediction,* Computers and Fluids **29**, 849 (2000).

[48] S. J. Schmidt, I. H. S. nad G. H. Schnerr, and M. Thalhamer, *Riemann techniques for the simulation of compressible liquid flows with phase-transition at all mach numbers - shock and wave dynamics in cavitating 3-d micro and macro systems,* in *46th AIAA Aerospace Sciences Meeting and Exhibit* (Reno, Nevada, 2008).

[49] E. Goncalves, M. Champagnac, and R. Fortes Patella, *Comparison of numerical solvers for cavitating flows,* International Journal of Computational Fluid Dynamics **24**, 201 (2010).

[50] J.-L. Reboud, O. Coutier-Delgosha, B. Pouffary, and R. F. Patella, *Numerical simulation of unsteady cavitating flows: Some applications and open problems,* in *Proceedings of the European Congress on Computational Methods in Applied Sciences and Engineering* (2004).

[51] S. Frikha, O. Coutier-Delgosha, and J. A. Astolfi, *Influence of the cavitation model on the simulation of cloud cavitation on 2d foil section,* International Journal of Rotating Machinery **2008** (2009).

[52] R. E. Bensow and G. Bark, *Simulating cavitating flows with les in openfoam,* in *Proceedings of the 5th European Conference on Computational Fluid Dynamics* (Lisbon, Portugal, 2010).

[53] J. Sauer and G. H. Schnerr, *Unsteady cavitating flow - a new cavitation model based on a modified front capturing method and bubble dynamics,* in *Proceedings of 2000 ASME Fluid Engineering Summer Conference*, Vol. 251 (2000) pp. 1073–1079.

[54] C. L. Merkle, J. Z. Feng, and P. E. O. Buelow, *Computational modeling of the dynamics of sheet cavitation,* in *Proceedings of the 3rd International Symposium on Cavitation* (Grenoble, France, 1998).

[55] S. Hickel, *Dns and les of two-phase flows with cavitation,* in *Direct and Large-Eddy Simulation IX* (Springer International Publishing, Cham, 2015) pp. 595–604.

[56] E. Lauer, X. Y. Hu, S. Hickel, and N. A. Adams, *Numerical investigation of collapsing cavity arrays,* Phys. Fluids **24**, 052104 (2012).

[57] U. Rasthofer, F. Wermelinger, P. Hadijdoukas, and P. Koumoutsakos, *Large scale simulation of cloud cavitation collapse,* Procedia Computer Science **108**, 1763 (2017), international Conference on Computational Science, ICCS 2017, 12-14 June 2017, Zurich, Switzerland.

[58] E. G. D. Silva and R. F. Patella, *Numerical study of cavitating flows with thermodynamic effect,* Computers and Fluids **39**, 99 (2010).

[59] P. Downar-Zapolski, Z. Bilicki, L. Bolle, and J. Franco, *The non-equilibrium relaxation model for one-dimensional flashing liquid flow,* International Journal of Multiphase Flow **22**, 473 (1996).

[60] M. Cristofaro, W. Edelbauer, P. Koukouvinis, and M. Gavaises, *A numerical study on the effect of cavitation erosion in a diesel injector,* Applied Mathematical Modelling **78**, 200 (2020).

[61] J. Sauer, *Instationär kavitierende Strömungen - Ein neues Modell, basierend auf Front Capturing (VoF) und Blasendynamik*, Ph.D. thesis, Universität Karlsruhe (2000).

[62] M. Pelanti and K.-M. Shyue, *A numerical model for multiphase liquid-vapor-gas flows with interfaces and cavitation,* International Journal of Multiphase Flow **113** (2019), 10.1016/j.ijmultiphaseflow.2019.01.010.

[63] H. B. Stewart and B. Wendroff, *Two-phase flow: Models and methods,* Journal of Computational Physics **56**, 363 (1984).

[64] OpenFOAM, *Openfoam website,* (2020).

[65] S. Schenke and T. J. C. van Terwisga, *Simulating compressibility in cavitating flows with an incompressible mass transfer flow solver,* in *Proceedings of the 5th International Symposium on Marine Propulsors* (Espoo, Finland, 2017).

[66] P. Koukouvinis and M. Gavaises, *Simulation of throttle flow with two phase and single phase homogenous equilibrium model,* Journal of Physics: Conference Series **656**, 012086 (2015).

[67] E. Ghahramani, M. H. Arabnejad, and R. E. Bensow, *A comparative study between numerical methods in simulation of cavitating bubbles,* International Journal of Multiphase Flow **111**, 339 (2019).

[68] T. Melissaris, S. Schenke, N. Bulten, and T. J. C. van Terwisga, *On the accuracy of predicting cavitation impact loads on marine propellers,* Wear **456-457**, 203393 (2020).

[69] M. Bhatt, A. Gnanaskandan, and K. Mahesh, *Evaluation of finite rate homogenous mixture model in cavitation bubble collapse,* Journal of Physics: Conference Series **656**, 012136 (2015).

[70] C. Eskilsson and R. Bensow, *Estimation of cavitation erosion intensity using cfd: Numerical comparison of three different methods,* in *Proceedings of the 4th International Symposium on Marine Propulsors* (Austin, Texas, USA, 2015).

[71] J. P. Franc and J. M. Michel, *Fundamentals of Cavitation*, Fluid Mechanics and Its Applications (Springer Netherlands, 2006).

[72] I. Akhatov, O. Lindau, A. Topolnikov, R. Mettin, N. Vakhitova, and W. Lauterborn, *Collapse and rebound of a laser-induced cavitation bubble,* Physics of Fluids **13**, 2805 (2001).

[73] C. Flageul, R. F. Patella, and A. Archer, *Cavitation erosion prediction by numerical cavitation,* in *Proceedings of the 14th International Symposium on Transport Phenomena and Dynamics of Rotating Machinery* (Honolulu, HI,USA, 2012).

[74] D. Obreschkow, M. Tinguely, N. Dorsaz, P. Kobel, A. de Bosset, and M. Farhat, *Universal scaling law for jets of collapsing bubbles,* Phys. Rev. Lett. **107**, 204501 (2011).

[75] M. S. Plesset, *The dynamics of cavitation bubbles,* Journal of Applied Mechanics **16**, 277 (1949).

[76] M. A. Maiga, O. Coutier-Delgosha, and D. Buisine, *A new cavitation model based on bubble-bubble interactions,* Physics of Fluids **30**, 123301 (2018).

[77] S. Schenke and T. J. C. van Terwisga, *Erosive aggressiveness of collapsing cavitating structures,* in *Proceedings of the 10th International Symposium on Cavitation* (Baltimore, Maryland, USA, 2018).

[78] H. Soyama, H. Kumano, and M. Saka, *A new parameter tp predict cavitation erosion,* Proceedings of the 4th International Symposium on Cavitation (2001).

[79] N. Ochiai, Y. Iga, M. Nohmi, and T. Ikohagi, *Numerical prediction of cavitation erosion in cavitating flow,* in *Proceedings of the 7th International Symposium on Cavitation* (Ann Arbor, Michigan, USA, 2009).

[80] B. P. Welford, *Note on a method for calculating corrected sums of squares and products,* Technometrics **4**, 419 (1962).

[81] G. Hardy, J. E. Littlewood, and G. Polya, *Inequalities,* (1934).

[82] M. van Rijsbergen, E.-J. Foeth, P. Fitzsimmons, and A. Boorsma, *High-speed video observations and acoustic-impact measurements on a naca 0015 foil,* in *Proceedings of the 8th International Symposium on Cavitation* (Singapore, 2012) pp. 958–964.

[83] J.-P. Franc, M. Riondet, A. Karimi, and G. L. Chahine, *Impact Load Measurements in an Erosive Cavitating Flow,* Journal of Fluids Engineering **133** (2011), 10.1115/1.4005342, 121301.

[84] R. I. Issa, *Solution of the implicitly discretised fluid flow equations by operator-splitting,* Journal of Computational Physics **62**, 40 (1986).

[85] H. Jasak, *Error analysis and estimation for the finite volume method with applications to fluid flows*, Ph.D. thesis, Imperial College (1996).

[86] H. Ganesh, S. A. Mäkiharju, and S. L. Ceccio, *Bubbly shock propagation as a mechanism for sheet-to-cloud transition of partial cavities,* Journal of Fluid Mechanics **802**, 37–78 (2016).

[87] C. Brennen, *The dynamic balances of dissolved air and heat in natural cavity flows,* Journal of Fluid Mechanics **37**, 115–127 (1969).

[88] S. Schenke and T. J. C. van Terwigsa, *Numerical prediction of vortex dynamics in inviscid sheet cavitation,* in *Proceedings of the 20th Numerical Towing Tank Symposium* (Wageningen, the Netherlands, 2017).

[89] M. Dular and M. Petkovšek, *On the mechanisms of cavitation erosion - coupling high speed videos to damage patterns,* Experimental Thermal and Fluid Science **68** (2015).

[90] S. J. Schmidt, M. Thalhamer, and G. H. Schnerr, *Inertia controlled instability and small scale structures of sheet and cloud cavitation,* in *Proceedings of the 7th International Symposium on Cavitation* (Ann Arbor, Michigan, USA, 2009).

[91] T. Xing, Z. Li, and S. Frankel, *Numerical simulation of vortex cavitation in a three-dimensional submerged transitional jet,* Journal of Fluids Engineering **127**, 714 (2005).

[92] M. Hoekstra and G. Vaz, *The partial cavity on a 2d foil revisited,* in *Proceedings of the 7th International Symposium on Cavitation* (Ann Arbor, Michigan, USA, 2009).

[93] Y. Kawanami, H. Kato, H. Yamaguchi, M. Maeda, and S. Nakasumi, *Inner structure of cloud cavity on a foil section,* JSME International Journal Series B Fluids and Thermal Engineering **45**, 655 (2002).

[94] T. J. C. van Terwisga, P. A. Fitzsimmons, Z. Li, and E. J. Foeth, *Cavitation erosion – a review of physical mechanisms and erosion risk models,* in *Proceedings of the 7th International Symposium on Cavitation* (Ann Arbor, Michigan, USA, 2009).

[95] A. Mantzaris, B. Aktas, P. Fitzsommons, and M. Atlar, *Establishment and verification of reproducible method for coating propeller blades for erosive cavitation detection,* in *Proceedings of the 4th International Conference on Advanced Model Measurement Technologies for the Maritime Industry* (2015).

[96] Z. Li, *Assessment of cavitation erosion with a multiphase Reynolds-averaged Navier-Stokes method*, Ph.D. thesis, Technische Universiteit Delft (2012).

[97] M. S. Mihatsch, S. J. Schmidt, and N. A. Adams, *Cavitation erosion prediction based on analysis of flow dynamics and impact load spectra,* Physics of Fluids **27**, 103302 (2015).

[98] A. Peters, H. Sagar, U. Lantermann, and O. Moctar, *Numerical modelling and prediction of cavitation erosion,* Wear **338-339** (2015), 10.1016/j.wear.2015.06.009.

[99] F. Schreiner, S. Mottyll, and R. Skoda, *A method for the coupling of compressible 3d flow simulations with a cavitation erosion model for ductile materials and assessment of the incubation time,* in *Proceedings of the 8th International Conference on Computational Methods in Marine Engineering* (Göteborg, Sweden, 2019).

[100] M. S. Mihatsch, *Numerical Prediction of Erosion and Degassing Effects in Cavitating Flows*, Ph.D. thesis, Technische Universiät München (2017).

[101] M. Gavaises, F. Villa, P. Koukouvinis, M. Marengo, and J.-P. Franc, *Visualisation and les simulation of cavitation cloud formation and collapse in an axisymmetric geometry,* International Journal of Multiphase Flow **68**, 14 (2015).

[102] L. Eça and M. Hoekstra, *A procedure for the estimation of the numerical uncertainty of cfd calculations based on grid refinement studies,* Journal of Computational Physics **262**, 104 (2014).

[103] L. F. Richardson and R. T. Glazebrook, *Ix. the approximate arithmetical solution by finite differences of physical problems involving differential equations, with an application to the stresses in a masonry dam,* Philosophical Transactions of the Royal Society of London. Series A, Containing Papers of a Mathematical or Physical Character **210** (1911).

[104] P. J. Roache, *Verification and Validation in Computational Science and Engineering* (Hermosa Publishers, 1998).

[105] P. J. Roache, *Fundamentals of Verification and Validation* (Hermosa Publishers, 2009).

[106] E. Ghahramani and R. E. Bensow, *Analysis of the finite mass transfer models in the numerical simulation of bubbly flows,* in *Proceedings of the 10th International Symposium on Cavitation* (Baltimore, Maryland, USA, 2018).

[107] M. J. Lighthill and M. H. A. Newman, *On sound generated aerodynamically i. general theory,* Proc. R. Soc. Lond. A **211** (1952).

[108] J. E. F. Williams, D. L. Hawkings, and M. J. Lighthill, *Sound generation by turbulence and surfaces in arbitrary motion,* Philosophical Transactions of the Royal Society of London. Series A, Mathematical and Physical Sciences **264** (1969).

[109] M. Benzi, G. H. G. J., and Liesen, *Numerical solution of saddle point problems,* Acta Numerica **14**, 1 (2005).

[110] F. Moukalled, L. Mangani, and M. Darwish, *The Finite Volume Method in Computational Fluid Dynamics: An Advanced Introduction with OpenFOAM and Matlab*, 1st ed. (Springer Publishing Company, Incorporated, 2015).

[111] F. P. Kärrholm, *Numerical Modelling of Diesel Spray Injection, Turbulence Interaction and Combustion*, Ph.D. thesis, Chalmers Tekniska Högskola (2008).

[112] C. M. RHIE and W. L. CHOW, *Numerical study of the turbulent flow past an airfoil with trailing edge separation,* AIAA Journal **21**, 1525 (1983).

[113] R. F. Warming and R. M. Beam, *Upwind second-order difference schemes and applications in unsteady aerodynamic flows,* in *Proceedings of the 2nd Computational Fluid Dynamics Conference* (Hartford, Connecticut, USA, 1975).

[114] B. van Leer, *Towards the ultimate conservative difference scheme. ii. monotonicity and conservation combined in a second-order scheme,* Journal of Computational Physics **14**, 361 (1974)

ACKNOWLEDGEMENTS

I would like to thank my promotor and daily supervisor Tom van Terwisga. I highly appreciate your excellent guidance and how you always give highest priority to the personal well-being of those around you. I also appreciate the freedom you gave me in shaping my research trajectory. Nevertheless, you continuously challenged me to critically reevaluate my work and its relevance in order to identify the essence of our research problem. Your deep knowledge of cavitating flow dynamics and your remarkable intuition on the importance of the involved physical parameters were crucial to my work. Thank you, Jerry Westerweel, for being my second promotor. Even though our discussions were rather concerned with general topics and aspects of fluid mechanics, I could learn a lot from you. I will never forget the absolutely unique and inspiring work environment that you provide in the lab of Fluid Mechanics.

I would also like to express my great gratitude to Manolis Gavaises, Amalia Petrova, and all the supervisors of the ITN program CaFE, who made this project possible and such a valuable experience, including the opportunity to learn from leading experts in the field of cavitation. Of course, the experience was enriched a lot by ESR 1, ESR 2, ESR 3, ESR 4, ESR 5, ESR 6, ESR 7, ESR 8, ESR 9, ESR 10, ESR 12, ESR 13, ESR 14, ESR 15, and ESR 16, hereafter referred to as my PhD-coworkers. Thank you for all the great times at our meetings and for all the scientific inspiration. On a somewhat more abstract level, my gratitude is extended to the European Union. The opportunity to collaborate with enthusiastic researchers from all over the world cannot be appreciated enough.

As part of the CaFE project, I was hosted by Steffen Schmidt at the Chair of Aerodynamics and Fluid Mechanics at the Technical University of Munich. I would like to thank you for sharing your knowledge, data and expertise, and for the important impulses that you gave at the early stage of the project. It was also of great help to share this time with Daria Ogloblina from TU Munich and Ebrahim Ghahramani from Chalmers. When setting up test cases, I could benefit from your knowledge of bubble cloud dynamics and OpenFOAM, respectively, and I enjoyed your company very much. Also the data and the knowledge shared by Mohammad Hossein Arabnejad Khanouki from Chalmers were very beneficial. In the second half of the project, Norbert Bulten and Petra Stoltenkamp hosted me for a secondment at Wärtsilä in Drunen. Getting introduced to the workflow of the department turned out to be very helpful and even necessary in order to assess the development done so far against the suitability in industrial practice and to get further impulses for improvement.

A very special thank you goes to my PhD-coworker Themis Melissaris, for all his support at Wärtsilä and for all the crucial contributions that he has made to our work. I am most happy that we decided to join our research trajectories together, because I am convinced that this has improved the quality of our research significantly, but also because of all the good times we had.

Next to the funding by the EU, this research was financially supported by the MARIN

Academy, where I was also hosted for more than a year. I would like to thank Artur Lidtke for his excellent guidance and for helping me to find my way through the user coding environment of ReFRESCO. I further want to thank Martijn van Rijsbergen, Guilherme Vaz, Serge Toxopeus, Evert-Jan Foeth, Bart Schuiling, Bram Starke, Thomas Lloyd, Erik van Wijngaarden, Johan Bosschers, and Auke van der Ploeg for their valuable feedback at several conferences and PhD meetings. And of course, I would like to thank my MARIN Academy colleagues Maarten, Gem, Sébastien, Chiara, Rui, and Benoît Leblanc for all the discussions about CFD and things I had no idea they existed, and also for introducing me to Poutine.

I would like to thank my daily colleagues from the Fluid Mechanics lab and those associated with it: Gijs, Gerben, Juanid, Dries, Caroline, Rob, Teng Dong, Udhav, Willian, Daniele, Rob, Sasha, Mike, Wout, Henk, Wouter, Tariq, Sudarshan, Yavuz, Lina, Andries, Jerke, Greta, Ankur, Pepijn, Melika, Arati, Maurice, Arnoud, Pedro, Ernst Jan, Jan, Amitosh, Edwin, Mark, Swaraj, Gerrit, Gem, Gosse, René, Marieke, Manu, Saad, Mathieu, Florian, Jasper Ruijgrok, Jasper Tomas, Sita, Sohrab, Özge, Christian Potma, Christian Poelma, Ellert, Koen, Guillermo, John, Parviz, Daniel, Wim-Paul, Ruud, Gema, Göktürk, Jana, Ankur, Haoyu Li, Bob, Willem, Bidhan, Angeliki. Your assist and company, including all the social events and little celebrations, were the reason why I was happy to go to work every morning, which I see as a privilege that by far not everyone enjoys.

I would further like to express my gratitude to Mathieu Pourquie. You were able to fix any technical issue I had with running my simulations on the cluster and to shed more light into the sometimes mysterious world of CFD. Very special thanks also to Duncan van der Heul. You did not only give me valuable advise on my work when I needed it the most, but you also challenged me to become more precise in my scientific approach. Thank you for taking all the time.

I also highly appreciated that I had Saad Jahangir sharing my office and Christian Poelma sitting next door. Saad, your thoughts, findings, and experimental observations on cavitation dynamics as well as your company were of great value, and I enjoyed all our common activities. Christian, you could often help me to find my way through the peculiarities of publishing processes or of conducting research in a rather big project. I would further like to thank Dineke Heersma and Caroline Legierse for their great administrative support throughout the entire time.

Furthermore, I would like to thank Benoît Cointe for his insightful and high quality work on the numerical simulation of condensation shocks in cavitating flows, which he did as part of his Master thesis project. I also highly appreciate the carefully and independently conducted work of all Bachelor students that I helped to supervise with their thesis projects.

Even though most of my daily work routine at TU Delft took place at the Fluid Mechanics lab, I would also like to thank my colleagues from the Ship Hydromechanics section of the MTT department. I enjoyed conducting and further developing the Advanced Course in Resistance and Propulsion together with Erik, Gem, Maarten, Swaraj, Pranav, Themis, Lina, and Tom, as well as assisting Tom and Cornel with supervision tasks. I also highly appreciate the valuable feedback on my work by Marco.

Practically from the first day on, I had the great pleasure to share my office with Gem. I enjoyed your company, support, dinners, and your valuable advise on scientific issues

or any other subject. I am also grateful to have met Juanita, Helene, and Cor from the Schilder- en Tekenclub Rotterdam, who share the passion about painting and who introduced me to the beauty of philosophy. Likewise, it was a great pleasure to discuss science and life with Carsten, preferably accompanied by a Nachoplank and/or cheescake. Also, I will always keep the numerous visits of nice coffee bars and the market of Delft together with Amitosh in good memory, just as well as the extended walks, runs and chats together with my language course mate Alberto. You guys truly made me feel home in Delft. Also big thanks to my former study mates, and especially to Jan and Leon, for establishing SaL and for being the all time record holders in visiting me in Delft. And also big thanks to Andi and Anastasia, for always being there, the excellent food, and for providing me with socks when I am short of them. With the years of my PhD research at TU Delft coming to an end, it seemed like a rather remarkable and fortunate circumstance that my old study mate Hendrik sent me the posting for the CaFE research position, which I would most likely not have found myself at that time. So thank you a lot for your awareness.

I cannot express how grateful I am to have met you, Heike, how grateful I am for your love, for all the practical and emotional support, the inspiration that you give, and for your undivided attention upon all the PhD-related relevancies and irrelevancies that tended to occupy my mind every now and then. Last but certainly not least, I want to thank my parents, my brother and his wife, my grandparents, and my not yet in-laws, for being the best family I can possibly imagine. You give me unconditional love and support, and you are always there whenever I need help, rest, or a place to stay.

A

Appendix A

A

A.1. SEGREGATED EQUATIONS

A segregated pressure-based approach is employed to solve the equations on a collocated grid. Pressure-velocity coupling is achieved by solving a pressure equation, involving a Laplacian term of the pressure field, followed by a correction of the velocity field which is directly obtained by forward substitution of the previously computed pressure field [85]. The pressure equation and the velocity correction step provide a solution of the Euler equations given by Eqn. (2.16) and Eqn. (2.17). Phase transition is achieved by solving the transport equation of liquid volume fraction given by Eqn. (2.21). In the following, the procedure to obtain the set of discretized equations to be solved is described in more detail.

The momentum equation is written in the linearized semi-discrete form (discrete in the momentum field $\mathbf{U}$) [85]

$$A_{\mathbf{u}C}\mathbf{U}_C + BP_C = H_{\mathbf{u}}(\mathbf{U}), \tag{A.1}$$

where $\mathbf{U}_C$ and P_C are the velocity and the pressure field assembled at the cell centers and the matrix $A_{\mathbf{u}C}$ contains the diagonal discretization coefficients only, such that it is cheaply inverted. The vector $H_{\mathbf{u}}(\mathbf{U})$ contains the neighbor coefficients multiplied by the corresponding velocities known from the previous iteration step as well as the explicit part of the discretized time derivative term. Furthermore, the operator B represents the gradient operator ∇ applied to the entire field, such that

$$BP_C = \left[\; (\nabla p_{C,1})^T, \quad \ldots \quad (\nabla p_{C,i})^T, \quad \ldots \quad (\nabla p_{C,n_{\text{cells}}})^T \; \right]^T, \quad \text{where } i \in [1, n_{\text{cells}}] \tag{A.2}$$

and where n_{cells} is the number of grid cells in the computational domain. Analogous, the mass continuity equation is written in the semi-discrete form

$$A_{pC}P_C + B^T\mathbf{U}_C = H_p(P), \tag{A.3}$$

as well (discrete in the pressure field P), where B^T represents the divergence operator $\nabla\cdot$ applied to the entire field such that

$$B^T\mathbf{U}_C = \left[\; \nabla\cdot\mathbf{u}_{C,1}, \quad \ldots, \quad \nabla\cdot\mathbf{u}_{C,i}, \quad \ldots, \quad \nabla\cdot\mathbf{u}_{C,n_{\text{cells}}} \; \right]^T, \quad \text{where } i \in [1, n_{\text{cells}}]. \tag{A.4}$$

The matrix A_{pC} denotes the coefficient matrix, being implicit with respect to P_C, and the vector $H_p(P)$ represents the corresponding explicit term. Both A_{pC} and $H_p(P)$ stem from the discretization of the cavitation model source term, which is explained in more detail in Appx. A.2. Assembling Eqn. (A.1) and Eqn. (A.3), the following coupled linear system is obtained:

$$\underbrace{\begin{bmatrix} A_{\mathbf{u}C} & B \\ B^T & A_{pC} \end{bmatrix}}_{M} \underbrace{\begin{bmatrix} \mathbf{U}_C \\ P_C \end{bmatrix}}_{X} = \underbrace{\begin{bmatrix} H_{\mathbf{u}}(\mathbf{U}) \\ H_p(P) \end{bmatrix}}_{\text{RHS}} \tag{A.5}$$

Boundary operators have already been applied to $\mathbf{U}_C$ and P_C in Eqns. (A.1) and (A.3) so that the system matrix M in Eqn. (A.5) has full rank. The solution technique described in the following has originally been developed for entirely incompressible flows, where $B^T\mathbf{U}_C = 0$. Eigenvalue analysis of M then shows that the linear system given by Eqn. (A.5)

evolves into a saddle-node problem [109]. In order to adapt iterative solution techniques designed for large and sparse problems [109] of this kind, it is convenient to decompose Eqn. (A.5) into sub-systems of more favorable eigenvalues [110]. Essentially, two possible sets of segregated equations equivalent to Eqn. (A.5) can be obtained from Schur complement reduction of M [109]. This reduction is obtained from the block triangular factorization of M, given by [109]

$$M = \begin{bmatrix} I & O \\ B^T A_{\mathbf{u}C}^{-1} & I \end{bmatrix} \begin{bmatrix} A_{\mathbf{u}C} & O \\ O & \mathfrak{S} \end{bmatrix} \begin{bmatrix} I & A_{\mathbf{u}C}^{-1} B \\ O & I \end{bmatrix}, \tag{A.6}$$

The matrix $\mathfrak{S} = A_{pC} - B^T A_{\mathbf{u}C}^{-1} B$ is the Schur complement [109] and I is the identity matrix. By either multiplying the first and the second matrix on the right-hand side of Eqn. (A.6) or the second and the third matrix, two different left-right ($\mathfrak{L} - \mathfrak{U}$) factorizations of M can be obtained, eventually leading to different sets of segregated equations. In this work, the first option is followed, where the left-right decomposed system becomes

$$M = \underbrace{\begin{bmatrix} A_{\mathbf{u}C} & 0 \\ B^T & \mathfrak{S} \end{bmatrix}}_{\mathfrak{L}} \underbrace{\begin{bmatrix} I & A_{\mathbf{u}C}^{-1} B \\ 0 & I \end{bmatrix}}_{\mathfrak{U}}. \tag{A.7}$$

A solution of Eqn. (A.5) is then obtained step wise by first computing an interim solution X^* from $\mathfrak{L}X^* = \text{RHS}$ and then the final solution from $\mathfrak{U}X = X^*$. The term $\mathfrak{L}X^* = \text{RHS}$ gives

$$A_{\mathbf{u}C} \mathbf{U}_C^* = H_{\mathbf{u}}(\mathbf{U}), \tag{A.8}$$

$$B^T \mathbf{U}_C^* + \left[A_{pC} - B^T A_{\mathbf{u}C}^{-1} B \right] P_C^* = H_p(P). \tag{A.9}$$

The term $\mathfrak{U}X = X^*$ gives

$$\mathbf{U}_C + A_{\mathbf{u}C}^{-1} B P_C = \mathbf{U}_C^* \tag{A.10}$$

and the trivial solution $P_C = P_C^*$. Solving Eqn. (A.8) for $\mathbf{U}_C^*$, substituting into Eqn. (A.9) and further substituting $\mathbf{U}_C^*$ into Eqn. (A.10) and solving for $\mathbf{U}_C$ yields the pressure equation given by Eqn. (A.11), which needs to be solved for the collocated pressure field P_C, and the momentum correction equation given by Eqn. (A.12), from which the updated collocated momentum field $\mathbf{U}_C$ is obtained by forward substitution of P_C:

$$\left[A_{pC} - B^T A_{\mathbf{u}C}^{-1} B \right] P_C = H_p(P) - B^T \left[A_{\mathbf{u}C}^{-1} H_{\mathbf{u}}(\mathbf{U}) \right] \tag{A.11}$$

$$\mathbf{U}_C = A_{\mathbf{u}C}^{-1} \left[H_{\mathbf{u}}(\mathbf{U}) - B P_C \right] \tag{A.12}$$

The transport equation of the liquid fraction γ (see Eqn. (2.21)) is solved in a separate step. The solver is run in a PISO (Pressure-Implicit with Splitting of Operators [84]) mode as implemented in OpenFOAM (see [85], [64]), which means that the γ equation, placed in the outer iteration loop, is solved once per time step only. Three inner iteration loops over pressure equation and velocity correction are performed. No relaxation is applied.

An important detail that cannot be seen from the above equations is how the implicit Laplacian term of Eqn. (A.11) and the explicit gradient term of Eqn. (A.12) are discretized. By employing the face interpolated form of $A_{\mathbf{u}C}^{-1}$ and by utilizing the Gauss

theorem to discretize both terms, an oscillation free solution is obtained for the collocated grid arrangement [85, 111], which would otherwise require the Rie-Chow correction [112] of the velocity field. The procedure to discretize the momentum equation resulting in the semi-implicit form as given by Eqn. (A.1) and hence the coefficient matrix $A_{\mathbf{u}C}$ is described in the work by Jasak [85]. The discretized terms of the γ equation (Eqn. (2.21)) as well as the terms A_{pC} and $H_p(P)$ of the pressure equation (Eqn. (A.11)) are presented in more detail in Appx. A.2 as they require some modification compared to the original solver due to the modified cavitation model.

A.2. DISCRETIZATION PROCEDURE

The modified form [65] of the Merkle model [54] source term given by Eqn. (2.19) is rewritten in two different forms to derive a semi-implicit form of the pressure equation and the liquid fraction transport equation, respectively. In order to be treated (partially) implicitly in the pressure equation, the mass transfer source term must be expressed as a function of pressure, such that

$$\nabla \cdot \mathbf{u} = \left[\dot{m}_{pv} + \dot{m}_{pc}\right](p - p_v), \tag{A.13}$$

where

$$\dot{m}_{pv} = \begin{cases} \gamma \frac{C_v}{\rho}\left(\frac{1}{\rho_l} - \frac{1}{\rho_v}\right) & \text{if} \quad p \le p_v \\ 0 & \text{if} \quad p > p_v \end{cases}$$

and

$$\dot{m}_{pc} = \begin{cases} 0 & \text{if} \quad p \le p_v \\ (1-\gamma)\frac{C_c}{\rho}\left(\frac{1}{\rho_l} - \frac{1}{\rho_v}\right) & \text{if} \quad p > p_v \end{cases}$$

Evaluating the source term of A.13 at the cell center location, referred to by the subscript C, gives the semi-discrete equation

$$\nabla \cdot \mathbf{u}_C + \underbrace{\left(\dot{m}^0_{pc,C} - \dot{m}^0_{pv,C}\right)}_{a_{pC}} p_C = \underbrace{\left(\dot{m}^0_{pc,C} - \dot{m}^0_{pv,C}\right) p_v}_{h_p(p)}, \tag{A.14}$$

where the superscript 0 indicates that the corresponding terms are assumed to be known from the previous iteration step. Assembling the underbraced terms a_{pC} and $h_p(p)$ in Eqn. (A.14) for the entire computational domain gives the matrices A_{pC} and $H_p(P)$ in the pressure equation as given by Eqn. (A.11). To be treated (partially) implicitly in the liquid fraction transport equation, the mass transfer source term must be expressed as a function of the liquid fraction γ, which gives

$$\nabla \cdot \mathbf{u} = \underbrace{-\left[\gamma \dot{m}_{\gamma v} + (1-\gamma)\dot{m}_{\gamma c}\right]}_{\dot{m}_\gamma}\left(\frac{1}{\rho_v} - \frac{1}{\rho_l}\right), \tag{A.15}$$

where

$$\dot{m}_{\gamma v} = \begin{cases} \frac{C_v}{\rho}(p - p_v) & \text{if} \quad p \le p_v \\ 0 & \text{if} \quad p > p_v \end{cases}$$

and

$$\dot{m}_{\gamma c} = \begin{cases} 0 & \text{if} \quad p \le p_v \\ \frac{C_c}{\rho}(p - p_v) & \text{if} \quad p > p_v \end{cases}.$$

To obtain an implicit form of the liquid fraction transport equation, Eqn. (2.21) is rewritten as follows:

$$\frac{\partial \gamma}{\partial t} + \nabla \cdot (\gamma \mathbf{u}) = \frac{\dot{m}_\gamma}{\rho_l} + \gamma \left(\frac{1}{\rho_v} - \frac{1}{\rho_l} \right) \dot{m}_\gamma - \gamma \left(\frac{1}{\rho_v} - \frac{1}{\rho_l} \right) \dot{m}_\gamma \tag{A.16}$$

Substituting Eqn. (2.19) for only the second term on the right-hand side of Eqn. (A.16) gives

$$\frac{\partial \gamma}{\partial t} + \nabla \cdot (\gamma \mathbf{u}) = \underbrace{\left[\frac{1}{\rho_l} - \gamma \left(\frac{1}{\rho_v} - \frac{1}{\rho_l} \right) \right] \dot{m}_\gamma}_{\dot{\mathfrak{V}}} + \gamma \nabla \cdot \mathbf{u}. \tag{A.17}$$

With the definition of $\dot{m}_\gamma$ in Eqn. (A.15), we get

$$\dot{\mathfrak{V}} = -\underbrace{\gamma \left[\frac{1}{\rho_l} - \gamma \left(\frac{1}{\rho_v} - \frac{1}{\rho_l} \right) \right] \dot{m}_{\gamma v}}_{\dot{\mathfrak{V}}_v} + \underbrace{\gamma \left[\frac{1}{\rho_l} - \gamma \left(\frac{1}{\rho_v} - \frac{1}{\rho_l} \right) \right] \dot{m}_{\gamma c}}_{\dot{\mathfrak{V}}_c} - \underbrace{\left[\frac{1}{\rho_l} - \gamma \left(\frac{1}{\rho_v} - \frac{1}{\rho_l} \right) \right] \dot{m}_{\gamma c}}_{\dot{\mathfrak{V}}_c}, \tag{A.18}$$

and the integral form of Eqn. (A.16) becomes

$$\int_{\mathrm{CV}} \frac{\partial \gamma}{\partial t} \mathrm{d}V + \int_{\mathrm{CV}} \nabla \cdot (\gamma \mathbf{u}) \, \mathrm{d}V - \int_{\mathrm{CV}} \gamma \nabla \cdot \mathbf{u} \mathrm{d}V + \int_{\mathrm{CV}} \gamma (\dot{\mathfrak{V}}_v - \dot{\mathfrak{V}}_c) \, \mathrm{d}V = -\int_{\mathrm{CV}} \dot{\mathfrak{V}}_c \mathrm{d}V. \tag{A.19}$$

Employing the Gauss theorem, the discrete convection term of Eqn. (A.19) is constructed from the face fluxes, which are obtained from interpolation between the cell center associated with index C and the neighboring cell centers associated with index N:

$$\int_{\mathrm{CV}} \nabla \cdot (\gamma \mathbf{u}) \, \mathrm{d}V \approx \sum_f (\gamma \mathbf{u}^0)_f \cdot S_f \approx \widetilde{a}_{\gamma C} \gamma_C + \sum_N \widetilde{a}_{\gamma N} \gamma_N \tag{A.20}$$

A linear scheme is employed for the time derivative term in Eqn. (A.19), such that

$$\int_{\mathrm{CV}} \frac{\partial \gamma}{\partial t} \mathrm{d}V \approx \frac{\gamma_C - \gamma_C^0}{\Delta t} V_C, \tag{A.21}$$

where again the superscript 0 refers to the previous time step, for which the value of γ_C is already known. Further normalizing by the cell volume V_C, the discrete liquid fraction transport equation becomes

$$a_{\gamma C} \gamma_C + \sum_N a_{\gamma N} \gamma_N - \frac{1}{V_C} \left(\sum_f \mathbf{u}_f^0 \cdot S_f \right) \gamma_C + \dot{\mathfrak{V}}_v^0 \gamma_C - \dot{\mathfrak{V}}_c^0 \gamma_C = \frac{\gamma_C^0}{\Delta t} - \dot{\mathfrak{V}}_c^0, \tag{A.22}$$

where

$$a_{\gamma C} = \frac{1}{\Delta t} + \frac{\widetilde{a}_{\gamma C}}{V_C} \quad \text{and} \quad a_{\gamma N} = \frac{\widetilde{a}_{\gamma N}}{V_N}.$$

For discretization of the convective terms in the momentum equation and the liquid fraction transport equation, the upwind-biased linear scheme [113] and the Van Leer [114], respectively, is employed. The Laplacian term of pressure in the pressure equation is discretized by using a linear scheme as described by Jasak [85].

A.3. RESIDUAL CONTROLS

The presence of the mass transfer source term in the governing equations demands special attention to the residual measure of the algebraic equations because they can become strongly source term dominated., which may affect the accuracy of the solution. The discretized equations to be solved can be written in the simplified notation [110]

$$a_C \phi_C + \sum_N a_N \phi_N = b_C. \tag{A.23}$$

In Eqn. (A.23), ϕ is the unknown quantity to be solved for. The index C refers to the local cell center and the index N to the cell centers of the corresponding neighbors. The coefficients a_C and a_N stem from the temporal and spatial discretization and the interpolation step that is needed in the finite volume formulation on a collocated grid to express face quantities in terms of the adjacent cell centered values. In the open source CFD environment OpenFOAM [64], the local residual remaining after solving the equations iteratively, is expressed in the normalized form [110]

$$\mathfrak{r}\left(\phi_C\right) = \frac{1}{\max\left(\| a_C \phi_C \|\right)} \left(a_C \phi_C + \sum_N a_N \phi_N - b_C \right), \tag{A.24}$$

where $\max\left(\| a_C \phi_C \|\right)$ is the maximum value of $a_C \phi_C$ of all cells. The global residual is given by the L_1 norm of Eqn. (A.24), where $L_1(\mathfrak{r}) = 1/n_{\text{cells}} \sum_{i=1}^{n_{\text{cells}}} \| \mathfrak{r}_i \|$. The solution of an equation is considered as converged if $L_1(\mathfrak{r})$ falls below the residual tolerance $\epsilon_{\mathfrak{r}}$. In the present work, the solver iterates over the discretized γ-transport equation until the residual drops below $\epsilon_{\mathfrak{r}} = 10^{-13}$. The final residual tolerance of the pressure equation is chosen to be $\epsilon_{\mathfrak{r}} = 10^{-11}$.

CURRICULUM VITÆ

Sören SCHENKE

30-09-1987	Born in Sömmerda, Germany.

EDUCATION

2020–present	Postdoctoral research Otto von Guericke University Magdeburg Magdeburg, Germany
2015–2020	PhD research Department of Maritime and Transport Technology Department of Process & Energy Delft University of Technology Delft, the Netherlands MARIN Academy Maritime Research Institute Netherlands (MARIN) Wageningen, the Netherlands
2012–2015	M.Sc. study in Naval Architecture and Ocean Engineering Hamburg University of Technology Hamburg, Germany
2014	Erasmus exchange in 2014 Delft University of Technology Delft, the Netherlands
2008–2012	B.Sc. study in Naval Architecture Hamburg University of Technology Hamburg, Germany

AWARDS

2019	Best Poster Award 2019 at the Cavitation and Multi-Phase Flows Workshop in Chania (Greece)
2016	Hanns Voith Foundation Prize for the Master thesis

LIST OF PUBLICATIONS

5. **S. Schenke, T. Melissaris, and T. J. C. van Terwisga**, *A Numerical Study on the Energy Focusing Mechanism in Periodic Cavitating Flows and its Effect on Impact Load Distributions Caused by Repetitive Cavity Implosions*, in preparation (2020).

4. **S. Schenke, and D. R. van der Heul, and T. J. C. van Terwisga**, *On the Validity of the Mass Transfer Modeling Approach in a Macroscopic Model for Cavitating Flows*, in preparation (2020).

3. **T. Melissaris, and S. Schenke, and N. Bulten, and T. J. C. van Terwisga**, *On the accuracy of predicting cavitation impact loads on marine propellers*, Wear **456-457**(2020), 203393.

2. **S. Schenke, T. Melissaris, and T. J. C. van Terwisga**, *On the Relevance of Kinematics for Cavitation Implosion Loads*, Physics of Fluids **31**(5), 052102 (2019).

1. **S. Schenke, and T. J. C. van Terwisga**, *An Energy Conservative Method to Predict the Erosive Aggressiveness of Collapsing Cavitating Structures and Cavitating Flows from Numerical Simulations*, International Journal of Multiphase Flow **111**, 200 (2019).